# On the Power Performance and Integration of Carbon-dioxide Plume Geothermal (CPG) Electrical Energy Production

A DISSERTATION SUBMITTED TO THE FACULTY
OF THE UNIVERSITY OF MINNESOTA
BY

**Benjamin M. Adams**

IN PARTIAL FULFILLMENT OF THE
REQUIREMENTS FOR THE DEGREE OF DOCTOR OF PHILOSOPHY

Thomas H. Kuehn, Advisor
Martin O. Saar, co-Advisor

May 2015

# Acknowledgements

Never in my wildest dreams did I expect to get a PhD. I always thought I'd end up a well-educated contractor: building homes, putting on roofs, or making toilets flush, like my dad taught me. I spent the first several years after undergrad half-heartedly chasing that end. But life, doing what it does best, overlapped a period of personal intellectual boredom with a graduate school application deadline. Fortunately, young-undergraduate-senior Ben had the foresight to take the GRE while he was still capable, so to that younger version of myself goes my first *thanks*.

The **Department of Mechanical Engineering** accepted me into the masters program in the spring of 2007, and I'll forever indebted to them for that act of kindness. I still think there must have been a mistake—perhaps a clerical error in the admissions office. I had spent the prior three years alternating between summers as a DUKW driver tour guide in Wisconsin Dells and winters remodeling houses. At the time of my admission, I was a ski-bum in Steamboat Springs, Colorado. My undergraduate GPA was nothing to speak of and I had never formally worked as an engineer. But there I was, Fall 2007, somehow qualified to instruct undergraduates and taking graduate classes of my own. I was never so excited.

The first years in the masters program I spent learning to teach. **Professor Will Durfee** was an incredible mentor, helping me shake loose the undergraduate urge to police student work, and instead focusing on the only important outcome: learning. He taught me: to write succinctly, to change the system instead of tirelessly enforcing rules, and to give people a break. With Durfee's encouragement, I started my work with **Pamela Flash** at the Writing Center, crafting undergraduate writing instruction materials. Pamela was a great mentor, who taught me about making waves for the better, and that compromise, necessary to move anything forward, involves self sacrifice—she'd ask, "What did *you* give up?"

I split my Teaching Assistant positions between ME 2011, an introductory engineering class taught by Durfee, and ME 4031, Basic Measurements Laboratory. Measurements lab was that one class that every engineer hated taking: you go to lecture, use an incomprehensible apparatus in lab, and then spend hours trying to write something

intelligible about the experience. When **Professor McMurry** assumed the instructor role in 2008, he let me get involved in the process of devising curriculum for students. He gave me a great opportunity to try out new teaching methods—ways to help students learn in complex, fast-paced, regimented labs. McMurry taught me: how to let students learn more with less work, how to run meetings, and that scheduling an unfinished experiment on the syllabus was sometimes the best way to get it done.

In 2010, I switched to the PhD program and became a research assistant, thanks to my advisor, **Professor Thomas Kuehn**. He assigned me to work on $CO_2$ Plume Geothermal (CPG) energy, a completely new concept (to both the world and me) that involved the confluence of Carbon Capture and Sequestration (CCS) and geothermal power production. My research was supported by the forward-looking folks at the **University of Minnesota's Institute of Renewable Energy on the Environment** (IREE) who provided us with initial seed funding. **Professor Martin Saar**, my co-advisor, was Principal Investigator (PI) on the project, and would lead our group meetings over in the exotic Pillsbury Hall, where the four departments involved would meet: mechanical engineering, earth sciences, applied economics, and public policy.

I had never been in such an intense academic environment before; sometimes it seemed group meetings were in a foreign language. Nonetheless, I learned to pull my weight and produce results of value. I am very grateful that Professors Kuehn and Saar: saw fit to fund me, kept me moving forward, were incredibly patient, and provided ample feedback when needed. Professor Kuehn taught me that hard work, flavored with the occasional hand-drawn T-s diagram or a glance in the "good book," was enough to accomplish anything. With his support and a **National Science Foundation** (NSF) grant, for which I am also very grateful, I was able to "eat the elephant."

Of course, the most valuable resource you have in graduate school is friendship. Friends can talk you through the frustrating days and drink beer with you on the good ones. The "TA Bullpen" in ME 301 was a catalyst for friendships, where I met jokers such as: **Jason Trask**, **Krithiga Ganesan**, **Aaron Boomsma**, and **Amy Stech**. Jason and I shared a similar taste in late-night researching and conversing over Chinese food, and I believe we may have, through the entire course of our degrees, reciprocally extended each other's commitment to graduate school one month at a time.

**Ranga Gopalkrishnan**, **Mark Brandl**, **Tom Shepard**, and **Vivek Rawat** were fellow TAs in ME 4031, who all helped immensely to develop curriculum and provide feedback. Ranga and I stayed sane by biking to Duluth one year; Tom Shepard provided me teaching opportunities when he moved on to St Thomas; and Mark Brandl pulled the

brunt of the weight when we built the compressible flow laboratory together in 2009. Thank you.

**Baris "Barry" Mutlu** was an invaluable fellow TA in Heat Transfer and taught me everything I know about Turkey (the country). **Luke Franklin** was an icon within the department, and the original "tenured PhD student" who took me under his wing. I also had the distinct privilege of meeting, usually over a beer to "discuss" research hiccups, **Lance Wheeler**, **Derek Oberreit**, **Katelyn Schramke**, **Brian Jennissen**, **Jon Meyer**, and **Stephen Sedler**.

**Leanne Matthews** very generously volunteered her time as co-chair to improve the department with me, which seemed like a good idea at the time, through the ME Graduate Student Committee. **Margaret Peterson** would later pick up that torch, while graciously still allowing me to contribute, and made sure I never went uncaffeinated. I'd also like to thank Margaret and my mother, **Polly Adams-Olsen**, for taking the time to proof this document, removing the non-sequitirs and superfluous commas, and helping to shape it into something legible.

I could never have finished this dissertation without my college buddies who, despite the occasional quip relating to being in college for 13 years, have continued to support me all this time: **Dan Smith**, **Nate Raygor**, **Jeremy Iverson**, **Katie Vincent**, **Steve Prusak**, **Leah Christianson**, **Nate Bird**, and **Davy Johnson**. With them, I also count my brothers, **Sam Adams** and **Zachary Olsen**, who are awesome.

Lastly, I'd like to thank all the Department of Mechanical Engineering staff who have made my time here so productive: **John "The Gradfather" Gardner**, **Peter Zimmermann**, **Bob Nelson**, **Mark Erikson**, **Jeanne Sitzmann**, **Bernard Olson**, **Tori Piorek**, **Craig Shankwitz**, and **Alyssa Burger**. Bob was gracious enough to hire me as an undergraduate student worker in 2002; he taught me to balance work and life and that it's OK to screw up every once in a while. Peter taught me how to pour aluminum in the foundry. Mark taught me how to play cribbage. Craig, the only staff member to regularly wear sandals and a Hawaiian shirt, helped me be my own person. The Gradfather provided immeasurable encouragement and conversation over my course here, while reminding me that you catch more flies with honey than vinegar; by the way, if he's still there, remind him it's time to move to Australia.

So moral of the story. Sometimes you'll accomplish things you never even imagined. They'll only seem impossible if you stop to consider them. But any success you'll have will be a direct result the people that support you along the way. *Thanks.*

# Dedication

because Mom's charm
and Dad's goals,
because Dave and his work-a-crowd skills,
because Laurie's hard line and
grandma Bertha's chicken soup time,
because Gloria's passionate Spirit
needed Grandpa's can-tinker-it;
I am. This is for you.

# Abstract

$CO_2$ Plume Geothermal (CPG) energy is a method for producing electricity from heat extracted from hot rock layers or reservoirs deep within the earth's crust. CPG is differentiated from other geothermal technologies by several factors: 1) CPG uses $CO_2$ as the primary geologic working fluid instead of brine, 2) CPG utilizes naturally permeable porous reservoirs to extract heat, such as saline aquifers or depleted hydrocarbon reservoirs, 3) CPG is deep—a CPG reservoir must have a depth of 1 km to maintain $CO_2$ in its supercritical state; though depths of 2 to 5 km are more common, and 4) CPG utilizes reservoirs at common geologic temperature gradients, unlike traditional hydrothermal which utilizes shallow reservoirs of unusually high temperature. Thus, CPG is intended to be integrated into an existing $CO_2$ sequestration site affording an economic return on $CO_2$ capture expenses by providing carbon-neutral, dispatchable electricity. Even when CPG is used as a base-load power source, it correlates well with electrical demand, unlike wind and solar (Chapter 5).

Typically, CPG configurations consist of one or more injection and production wells. These wells link the surface plant with the porous reservoir to create a fluid circuit. Cooled fluid is injected at the surface, heated within the reservoir, and then returned to the surface at higher temperature and pressure which can then be used to create electricity. The variation in $CO_2$ density between injection and production wells creates a thermosiphon which can drive circulation of $CO_2$ without the use of pumps (Chapter 2). The geologic $CO_2$ can be passed directly through a turbine, called a direct system, or heat can be extracted and used to power an Organic Rankine Cycle, called an indirect system. Either system may be used to generate electricity, although a direct system will nearly always produce more electricity than the indirect system. With reservoirs at moderate depth and temperature, these direct systems will also produce more electricity than comparable brine hydrothermal systems (Chapter 3).

The reservoir well spacing and diameter affect the average power and longevity of a CPG system. For every combination of well diameter and reservoir depth, temperature, permeability, and thickness, an optimum spacing between the central injection well and a circumferential collection well will provide the greatest power output over time; placing the collection well too close to the injection well depletes the reservoir too quickly while spacing it too far away increases pressure losses, decreasing the overall power (Chapter 4). Likewise, the selection of too small a well diameter will limit mass flowrate, and thus power, while an oversized well diameter may quickly deplete the reservoir and provide no additional benefit (Chapters 3 & 4).

This research has provided a significantly deeper understanding of CPG power systems and their operation. The impact of this work is to establish a basis of CPG research to be used in several ways. It can directly inform industrial developments, such as a green-field implementation of CPG or the long-term planning of a CPG-ready Carbon Capture and Storage site. This work may also be the basis for future economic or policy analyses that can further argue for the development of CPG. Thus, this work will help enable CPG as part of the 21$^{st}$ century energy portfolio.

# Table of Contents

# List of Tables

## Chapter 1



## Chapter 2



## Chapter 3



## Chapter 4



## Chapter 5

# List of Figures

## Chapter 1



## Chapter 2

## Chapter 3



## Chapter 4

## Chapter 5

# Chapter 1

# Foreword

Geothermal energy is the utilization of the high rock temperature found within the earth to make power. Generally, one or more injection and production wells are drilled to develop a fluid circuit—cool fluid is injected from the surface to the reservoir situated several kilometers below, it is heated by the hot rock, and then the warmed fluid is returned to the surface (Figure 1.1). Then it can be used either to heat buildings or to generate electricity; however, only electricity production is considered here.

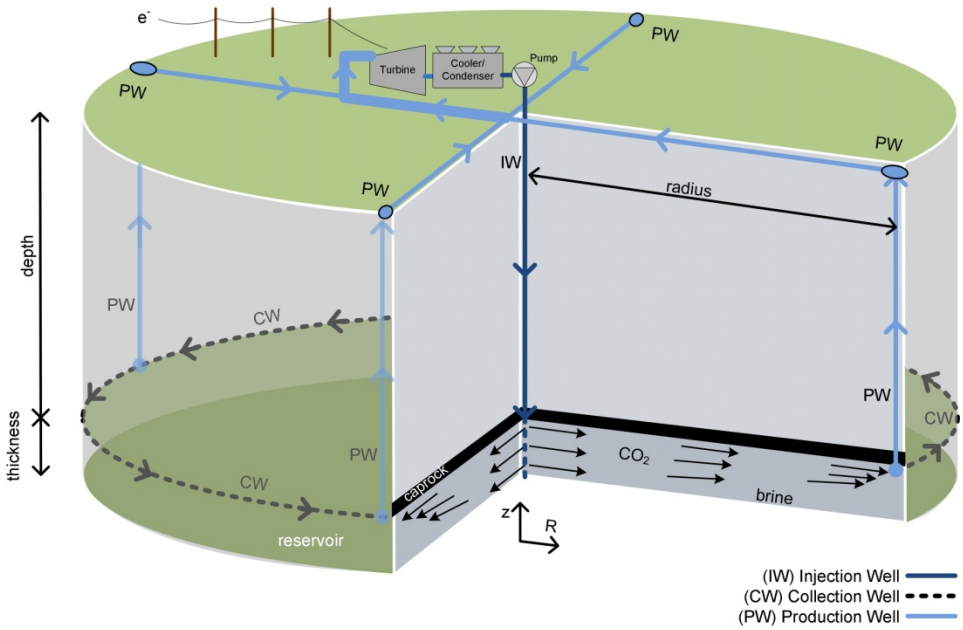


**Figure 1.1: Schematic of a $CO_2$ Plume Geothermal System** (Adams et al., In Preparation)

In this dissertation, research into a geothermal power concept called $CO_2$ Plume Geothermal (CPG) is described. It is different from existing geothermal, defined by several key characteristics:

- CPG uses **$CO_2$** as the primary geologic working fluid instead of water (brine),
- CPG utilizes **sedimentary basins** instead of fracture networks typical of existing geothermal and Enhanced Geothermal Systems,
- CPG is **deep**, used at depths between 1.5 and 5 km, and
- CPG is appropriate for **average temperatures**, instead of only geologic "hot-spots" typical of traditional geothermal locations.

CPG is considered deep compared to traditional brine-based geothermal systems, called hydro-geothermal, which tend to have wells shallower than 1 km. Also, as CPG may utilize resources below 150 °C, it is often referred to as "low-temperature" or "low-enthalpy" geothermal (DOE, 2015). Despite the low temperature label, CPG should not be confused with geothermal heat pumps which are common in residential applications; geothermal heat pumps use a refrigeration cycle to exchange heat with the cool groundwater near the surface, while CPG is a power cycle driven by the hot (>100 °C) earth.

Geothermal power is a renewable energy, and unlike wind and solar, is both dispatchable and can be a carbon sink when combined with Carbon Capture Utilization and Storage (CCUS). In the 2006 *Future of Geothermal Energy*, they found there to be approximately 200,000 EJ (1EJ = $10^{18}$ Joules) of accessible geothermal energy available within the United States, or more than 2,000 times the U.S.'s 2006 primary energy consumption (MIT, 2006). Additionally, they found that at least 100 GWe of geothermal energy could be brought online during the next 50 years, which would be a stark increase to the 3.4 GWe currently installed (NREL, 2014). Thus, geothermal power has great development potential to meet this century's energy demands, both in the United States and worldwide.

## 1.1 Dissertation Organization

This dissertation is comprised of this forward and four published (or soon-to-be published) papers on the subject of CPG electricity production. Each addresses a fundamental research question of CPG, which are as follows:

*Why use CPG?*

**Chapter 1**

Forward – The Big Picture, Motivation, and Background

*How large is the buoyancy-driven thermosiphon created by both $CO_2$ and water?*

**Chapter 2: The Thermosiphon**

"On the Importance of the Thermosiphon Effect in CPG ($CO_2$ Plume Geothermal) Power Systems" (Adams et al., 2014)

*How much electricity can a CPG system create compared to brine hydrogeothermal?*

**Chapter 3: Making Electricity**

"A Comparison of Electric Power Output of $CO_2$ Plume Geothermal (CPG) and Brine Geothermal Systems for Varying Reservoir Conditions" (Adams et al., 2015)

*How big of a reservoir is needed to generate electricity over a plant's lifetime?*

**Chapter 4: Electricity with Time**

"A Characterization of Temperature Depletion in a Sedimentary Basin and its Effect on the Electric Power Output of $CO_2$ Plume Geothermal (CPG) Power Systems" (Adams et al., In Preparation)

*How can a CPG plant meet a community's electricity demand?*

**Chapter 5: CPG vs. Wind and Solar: A Dispatchable Renewable**

"The Complementary Nature of $CO_2$ Plume Geothermal (CPG) Energy Production and Electrical Power Demand" (Adams and Kuehn, 2012)

The remainder of this forward provides context which is not provided in the academic papers that will enhance the reader's understanding of geothermal electricity production. First, the physical basis for geothermal electricity production is considered. Second, the unique value added by CPG will be presented from the perspective of future United States' energy policy. Third, the development of CPG from the research in traditional geothermal and Enhanced Geothermal Systems is shown. And lastly, the impact of the research presented here is explained.

## 1.2 Introduction to Geothermal Energy

The Earth is inevitably cooling—like a hot cup of coffee in a cold room. Physics dictates that its solid inner core, with temperatures greater than 4500°C, will transfer heat to the cooler surroundings: first through the outer liquid core, mantle, and crust to the surface, and then eventually to outer space. The two Earth rock layers of geothermal interest are the outermost two: the lithosphere and asthenosphere. The lithosphere is the portion of the Earth near the surface that behaves rigidly, containing the crust and the portion of the upper mantle cooler than 1300°C. The tectonic plates comprise the lithosphere. The 1300°C isotherm is typically used to define the lower boundary of the lithosphere as it is the temperature at which mantle rocks begin to behave fluidly (Self and Rampino, 2015). The lithosphere rests on the asthenosphere, or the ductile portion of the upper mantle which behaves plastically due to the high rock temperatures.

Heat is transferred from the inner Earth to the surface in different ways. Below the lithosphere, heat is transferred primarily through convection—convective rock cells are formed where hot rock physically flows to and from the surface, exchanging heat between the outer core and lithosphere. Conversely, heat is only conducted through the lithosphere. The radioactive decay of minerals found in the lithosphere provide the surface with about 50% more heat than would reach it through conduction alone (Armstead and Tester, 1987). If an approximate continental Lithospheric thickness of 100 km (Pasyanos, 2008) is combined with a mean average annual surface temperature of 15°C, accounting for both conduction and radioactive decay, an approximate continental

geothermal gradient of approximately 25 °C $km^{-1}$ is established near the surface (Armstead and Tester, 1987; DiPippo, 2012). Many factors, such as: thermal conductivity, thickness, and composition can affect the geothermal gradient (Saar, 2011).

Geothermal power production utilizes this natural geothermal temperature gradient to extract heat naturally stored within the Earth. Thus, this stored heat does not occur merely in the Western United States, where occasionally geothermal gradients in excess of 70 °C $km^{-1}$ occur, but even in places uncharacteristically associated with geothermal electricity production, such as Minnesota. In Minneapolis, if a well were drilled to 12 km—the current limit of well drilling technology—temperatures in excess of 180°C would be attained (Blackwell et al., 2011). Electricity could be generated with that resource, although not necessarily economically.

Any heat source can generate electricity, an engineering concept called a *heat engine*. Most electricity plants utilize a heat engine: fossil fuel plants use the heat derived from combusting fuel, concentrating solar plants (CSP) concentrate the sun's incoming radiation on a high-temperature focal point, and nuclear plants capture the heat emitted from nuclear fission. In the same way, geothermal power plants generate electricity from hot rock stored within the earth. The efficiency of this conversion—from heat to electricity—depends on the temperature: the hotter the resource, the greater the efficiency. Thus, most electric power plants utilize the fuel source at the hottest temperature tolerable by their equipment.

In the case of geothermal, developers do not have the luxury of controlling the temperature of its resource as most other electricity producers do. For example, that same Minnesota geothermal plant that drilled to 12 km for 180°C could instead be replaced by a natural gas turbine that operates at 550°C, without the expense of wells. For this reason, geothermal plants, while utilizing free energy from within the Earth, tend to have relatively low production temperature and thus low efficiency. Herein lays the long-established economic battle of geothermal electricity: though the fuel is free, geothermal

electricity production is capital-intense, and it must be produced in a manner such that its finances can compete with high-efficiency, low-capital fuel sources like natural gas. Fortunately for geothermal energy, these economics will shift with the likely mandate of $CO_2$ Capture and Sequestration (CCS).

## 1.3 The Big Picture

Before the technical merit of the work presented here can be examined, it is necessary to frame the knowledge in a context so that its value might be realized. Thus, we must venture outside the thermodynamics of power generation for a moment to consider *why $CO_2$ Plume Geothermal (CPG) research is essential*.

At the 2014 supercritical $CO_2$ ($sCO_2$) power cycles symposium, Frank Princiotta, the Director of the Air Pollution Prevention and Control Division of the Environmental Protection Agency (EPA) presented the long-term EPA plan to mitigate climate change (Princiotta, 2014). In order to limit global temperatures to 2 °C above pre-industrial values and avoid catastrophe, the atmospheric $CO_2$ concentration must be limited to 450 ppm (IPCC, 2014). To achieve this result, the United States $CO_2$ emissions must be reduced 80% by 2100 (Princiotta and Loughlin, 2014).

Using current energy consumption and improvements to technology, Princiotta was unable to simulate an 80% reduction in $CO_2$ emissions without significant lifestyle, social, and structural changes. Thus, an intermediate goal of 50% reduction in $CO_2$ emissions by 2050 was chosen. To achieve a 50% reduction, Figure 1.2 shows the $CO_2$ emissions in the electricity production sector will be essentially reduced to zero (Princiotta and Loughlin, 2014). This reduction will be through the increased use and development of renewable and nuclear energies, as well as $CO_2$ capture and sequestration (CCS). CCS is not specified in either the EPA's or the President's Climate Action Plan for 2030 (EPA, 2014; U.S. President, 2013); however, it is very likely that CCS will be mandated shortly thereafter. In the interim, the Department of Energy (DOE) research priorities are aimed at lessening the impact of CCS's 15-20% energy penalty (NETL,

2010) through the development and proving of transformational power plant technology, such as the $sCO_2$ Rankine cycle.

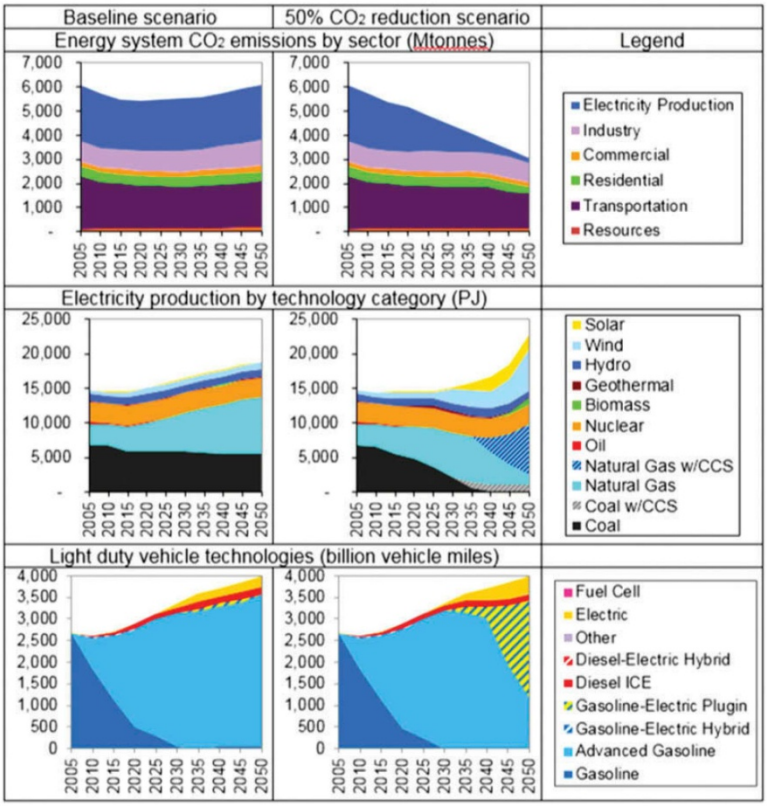


**Figure 1.2: $CO_2$ Emissions for Baseline and 50% Reduction Scenarios** (Princiotta and Loughlin, 2014)

*The Implementation of CCS Enables CPG*

Geothermal power utilizes a free fuel source, but the substantial capital costs, namely to explore, drill, and complete the wells, limit its economic competitiveness. Additionally, it has been found in yet-unpublished CPG research and by Atrens (2011) for $CO_2$-EGS, that a major factor in the economic viability of $CO_2$-based geothermal power production is the availability of low-cost or free $CO_2$.

Therefore, the implementation of CCS will enable CPG in two ways: first, by establishing $CO_2$ plumes in sedimentary reservoirs (Global CCS Institute, 2014) in volumes sufficient for CPG energy production; and second, by increasing the cost of $CO_2$-emitting electricity production. In addition to $CO_2$, CCS will provide, at least in part, the necessary well exploration and infrastructure for CPG. CCS will prove a reservoir's suitability for $CO_2$ storage, and in the process determine reservoir characteristics, such as permeability and geometry, all of which are essential and costly values to attain for geothermal alone. Additionally, the injection of $CO_2$ at a sequestration site may increase the reservoir pressure substantially, thus necessitating production wells to alleviate the over-pressurization and to contain the $CO_2$ plume (Buscheck et al., 2012). Therefore, CPG production at a CCS site will have greatly reduced capital costs than an undeveloped site, making the implementation of CPG more likely.

Therefore, it becomes necessary to research CPG, not just out of scientific curiosity, but rather to develop it as a likely electricity producer in this century's energy portfolio.

## 1.4 The Evolution of the CPG Concept

Geothermal electricity production is more than a hundred years old; the first geothermal electric plant was built in Larderello, Italy in 1904 (DiPippo, 2012). The first geothermal electric plant was built in the United States in 1921 at the Geysers in California. Since then, geothermal power development in the United States has expanded to 3.4 GWe (NREL, 2014), mostly in California and Nevada, making the United States the world's largest producer of geothermal electricity (GEA, 2013). California and Nevada have seen the majority of geothermal development as they are positioned over geologically active regions—locations where fractures and abnormalities in the crust have allowed unusually hot fluid to rise to near, and sometimes on, the surface. This ease of capture made the development of early geothermal electric plants straightforward and affordable—a free fuel source was available essentially at the surface, without the need for costly resource exploration. When the energy crisis of the 1970s at least tripled the price of oil, development of these resources became both economical and a national priority.

Many of these early geothermal plants, like some of those at the Geysers in California, were simple; they captured the hot fluid as it was emitted from the ground, processed it, and then released the cooled effluent to the surface. As the prevalence of geothermal plants expanded, the shallow and hot energy resources were quickly exploited and the industry began drilling increasingly deeper and more complex wells. Eventually the number of known sites with sufficiently shallow and hot resources got developed, and when combined with the cessation of public subsidies, geothermal development receded (Lund and Bloomquist, 2012). Thus was established the relatively flat line of geothermal development that extends from the late-1980s to today in Figure 1.3.

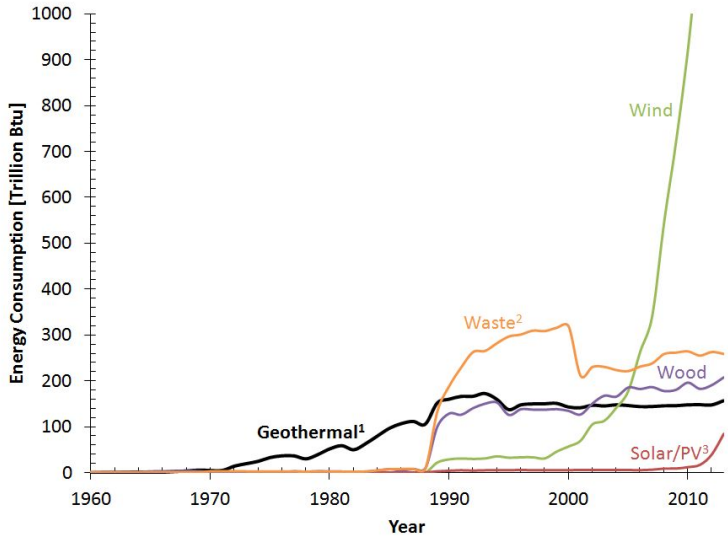


**Figure 1.3: U.S. Energy Consumption by Non-Hydroelectric Renewable for 1960-2013, given in terms of Fossil-based Generation Displaced by Renewable (EIA, 2015a).** All values, except for wood, are converted from electricity to thermal energy using a fossil-based conversion factor (See EIA (2015a) Table A6). [1]Does not include geothermal heat pumps. [2]Electricity produced from landfill gas, sludge waste, agricultural byproducts, and other biomass. Also considers non-renewable waste though 2000 (e.g. municipal trash). [3]Includes both solar thermal and photovoltaic (PV).

In the 1990s, it would have been difficult to imagine that the use of $CO_2$ as a geologic working fluid could be economically viable—the benefit of using $CO_2$ is lost when applied to the open-loop fracture networks utilized in traditional geothermal electric

production. It would take the confluence of two at-the-time unrelated fields to establish CPG: the Hot Dry Rock (HDR) deep geothermal EGS project and the Carbon Capture Utilization and Storage (CCUS) research into deep saline aquifers. First, the concept of using $CO_2$ as a geothermal working fluid will be discussed as it spun-off from the Fenton Hill HDR project.

*Fenton Hill: Making a Case for $CO_2$ Geothermal*

The Fenton Hill Hot Dry Rock (HDR) geothermal research center was a Department of Energy project, located 40 miles west of Los Alamos National Laboratory, born of the 1970s energy crisis (Brown, 2009). The HDR concept was newly developed by Los Alamos researchers; in HDR, deep wells (2.5 to 5 km) are drilled into low-permeability bedrock where the majority of the world's high-grade geothermal energy is located (Duchane and Brown, 2002). The wells were hydraulically over-pressurized up to 48 MPa at the surface, reopening existing fault lines and shearing their rough surfaces to permanently increase permeability (Duchane and Brown, 2002; MIT, 2006). Water was then circulated between the injection and production well, through the permeability-enhanced rock, to the surface (Tester et al., 1989; DiPippo, 2012). The use of deep wells to extract otherwise trapped energy in low-permeability rock was unprecedented at the time; most geothermal reservoirs only utilized shallow resources with existing fractures. Despite being a pilot-scale project, it demonstrated many important concepts of deep geothermal implementation in low-permeability rock. For instance, it showed: that wells could be directionally drilled to 5 km depths and accurately positioned using acoustic equipment; that the permeability of crystalline basement rock could be artificially enhanced, but only along existing fractures; and that water could be circulated through an EGS reservoir for extended periods of time to produce useful heat (MIT, 2006). The plant was dismantled in 1996 as energy priorities shifted from HDR (GTO, 2015; Ziagos et al., 2013).

In 2000, Donald Brown, a Los Alamos veteran of the Fenton Hill project, saw an opportunity emerge to further develop HDR. As atmospheric $CO_2$ concentrations were becoming an increasingly common topic of scientific discourse, he suggested the use of $CO_2$ in lieu of water in HDR (Brown, 2000). He argued that the HDR concept, while financially risky on its own, could become competitive when funded jointly with $CO_2$ sequestration efforts—HDR could be used both to store $CO_2$ and produce electricity. Additionally, $CO_2$ has many benefits when used as a geothermal working fluid, including: decreased mineral solubility, and an ability to circulate itself, called a thermosiphon, therefore reducing the need for pumps (Brown, 2000).

The use of $CO_2$ within a reservoir was a promising concept and tools were developed to validate it. Pruess (2004; 2005) developed an ECO2N module for TOUGH2 to simulate the injection of $CO_2$ into fractured or porous media. This was necessary for the simulation of $CO_2$ for both Carbon Capture and Storage (CCS) and HDR (Doughty, 2004). At about this same time, the term Enhanced or Engineered Geothermal Systems (EGS) superseded the term HDR as it more broadly included the artificial fracturing of any low-permeability system, not just the "dry" HDR systems. When EGS systems utilize $CO_2$ as the primary geologic working fluid, they are sometimes called $CO_2$-EGS.

$CO_2$-EGS research was initially only conducted from a reservoir dynamics perspective. $CO_2$ was shown to have comparable heat mining capabilities to that of brine, but without the complexities of pumping or mineral precipitation (Pruess, 2006; Pruess and Azaroual, 2006). Pruess (2008) first modeled a $CO_2$ reservoir three dimensionally and anticipated that the strong $CO_2$ sensitivity to temperature might increase reservoir productivity with time; similarly, the pressure profile of a static $CO_2$ well was simulated to show the high likelihood that a thermosiphon would develop. Pritchett (2009) critiqued the use of $CO_2$ as a geothermal fluid, arguing that within a fracture network the low viscosity would cause a short-circuit, decreasing the amount of rock directly in contact with the $CO_2$, and potentially halve the reservoir's lifetime. This is not an uncharacteristic finding for $CO_2$-EGS; however, Randolph and Saar (2011a) later would show that the reservoir lifetime

increased when fracture spacing decreased, and that a $CO_2$-EGS reservoir lifetime approaches that of CPG as fracture spacing goes to zero, which is essentially the definition of a sedimentary porous medium.

Agarwal and Anderson (2010) combined the EGS reservoir with a surface plant to simulate electricity production, finding water produced 80% more electricity than $CO_2$. However, their singular choice of a 3 km reservoir with an 80 °C $km^{-1}$ thermal gradient (the worldwide continental-crust average is 34 °C $km^{-1}$ (Pollack et al., 1993)) would later be found to be outside the ideal operating range of $CO_2$-based geothermal, which is moderate depths and temperature gradients (Adams et al., 2015). Similarly, Atrens (2010) estimated electricity production from an EGS reservoir and found that $CO_2$ was less efficient at energy extraction than water due to its smaller heat capacity and substantial wellbore pressure losses. They did note that if well diameter was increased (they used a 9" diameter well, typical of the oil & gas industry), $CO_2$ could be better suited for low-permeability reservoirs than brine – a finding confirmed in Adams et al. (2015).

$CO_2$-EGS still needs substantial research and development (Carroll and Stillman, 2014). Additionally, it has not proved financially viable with large estimated Levelized Cost of Electricity (LCOE) (>>\$100 $MWhr^{-1}$), generally due to the large cost of well construction (Atrens et al., 2011; Beckers et al., 2014). Nonetheless, $CO_2$-EGS research is ongoing (Borgia et al., 2012; Pan et al., 2013; Lou et al., 2014). EGS does have the potential to access the vast supplies of geothermal energy (13,300,000 EJ) contained within low-permeability basement rock; however, MIT (2006) points out that a substantial portion (100,000 EJ) of geothermal heat is still available in sedimentary formations, as discussed next.

*Sedimentary Basins are a Naturally-permeable Substitute for EGS*

The research climate in the mid-2000s was increasingly favorable for $CO_2$-based geothermal developments. $CO_2$ reservoir simulation tools had been developed and $CO_2$

was being shown to be a geologically favorable working fluid; however, these tools were only being used to simulate $CO_2$-EGS or $CO_2$ sequestration (CCS) into sedimentary basins. Thus far, no one had considered utilizing sedimentary basins for geothermal power.

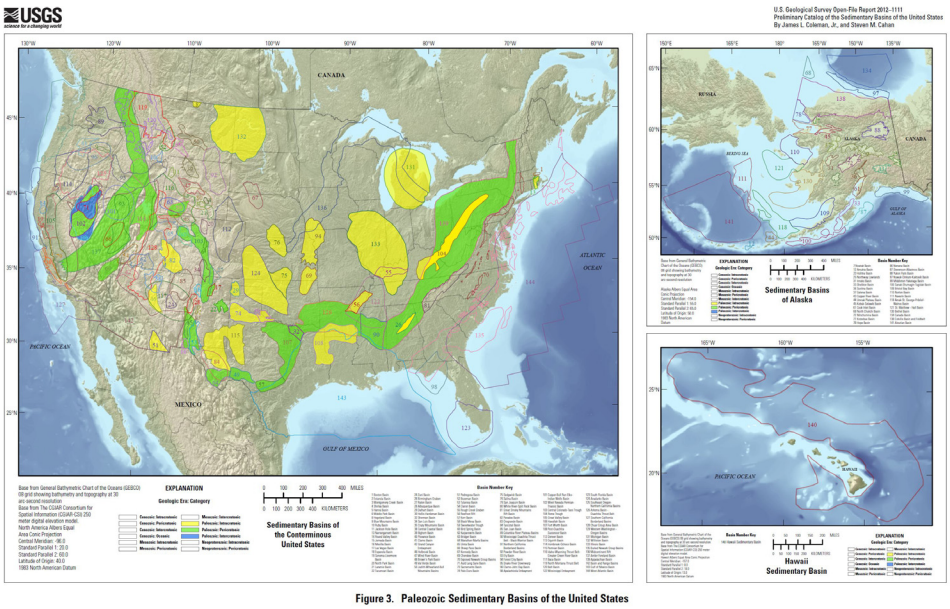


**Figure 1.4: Map of Paleozoic Sedimentary Basins in the United States.** Paleozoic basins are shaded while basins in other geologic layers are outlined. (Coleman and Cahan, 2012)

Sedimentary basins, which often contain saline aquifers or hydrocarbon reservoirs, are expansive, permeable formations that extend across much of the United States and the world (Runkel et al., 2007; Coleman & Cahan, 2012). Figure 1.4 shows the ubiquity of Paleozoic sedimentary basins in the United States, which are at depths likely to be suitable for CPG. When capped with an impermeable caprock, they form a layer within the earth which can hold massive volumes of $CO_2$, unlike man-made HDR and EGS reservoirs which are comparatively smaller-scale. Azar et al. (2006) estimates between 30 and 650 Gt-C (110 and 2400 Gt-$CO_2$) can be stored in sedimentary basins globally. Sedimentary basins also offer a significant benefit over the fractured basement rock of EGS—they are a current target for $CO_2$ sequestration (Global CCS Institute, 2014).

Thus, it was not unusual when, in 2008, Jimmy Randolph and Professor Martin Saar extended $CO_2$ geothermal research from EGS into another field with which they were both familiar: sedimentary basins (Randolph, 2011). They termed the combination of $CO_2$ and porous media $CO_2$ Plume Geothermal (CPG), based on early analytical models of geologic $CO_2$ storage during CCS, where the $CO_2$ and brine did not mix (much) but the $CO_2$ displaced the brine, forming a distinct funnel-shaped "plume" (Nordbotten, 2005). Another reason for the term CPG was to distinguish it from $CO_2$-EGS as CPG allows storage of large quantities of $CO_2$. $CO_2$-EGS reservoirs are created artificially, and due to the limited extent and nature of the fracturing, often have widely spaced fractures which only store minimal amounts of $CO_2$ underground.

In 2009, Saar and Randolph, with Professor Thomas Kuehn, patented CPG (Saar et al., 2012-2015), and received seed funding from Minnesota's Institute for Renewable Energy & the Environment (IREE), now a signature program of the Institute on the Environment (IonE). With Professor Saar as Principle Investigator (PI), the CPG research group at the University of Minnesota was formed with co-PIs from complementary fields of expertise: Professor Thomas Kuehn from Mechanical Engineering, Professor Steven Taff from Applied Economics, and Professor Elizabeth Wilson from Public Policy, succeeded by Professor Jeff Bielicki. The group received a three-year Department of Energy (DOE) Grant (DE-EE0002764) to research $CO_2$ fluid-mineral interactions in 2010.

*CPG Research at the University of Minnesota (and beyond)*

Initial CPG work compared the heat extraction efficiency of porous and fractured reservoirs, showing that sedimentary reservoirs could produce hotter downhole $CO_2$ for a longer duration than Water-EGS (Randolph and Saar, 2010). Randolph and Saar (2011b) found similar results when CPG was compared against water-sedimentary geothermal systems and water-EGS. Randolph and Saar (2011c) examined a range of reservoir permeabilities and found that at permeabilities higher than 5 $x10^{-14}$ $m^2$ brine produced more power, while at lower permeabilities $CO_2$ produced more power. Additionally,

Randolph and Saar (2011a) performed an economic analysis using estimated power values based on Carnot efficiency, finding that between 7% and 12% of $CO_2$ capture energy cost could be recovered by utilizing CPG.

Working with Randolph and Saar, Janke and Kuehn (2011) simulated power production of both direct and indirect surface plants using a fixed-pressure-drop reservoir model. A direct surface plant extracts pressure energy using a turbine directly in the geologic $CO_2$ stream, while an indirect surface plant extracts only heat energy from the geologic $CO_2$ using a heat exchanger and an off-the-shelf Organic Rankine Cycle (ORC). They found a direct-type CPG system to produce the most power.

Thus far, models for both $CO_2$-EGS and CPG had assumed the wells were adiabatic (i.e., did not lose heat to the surrounding rock); although there was some concern that the higher wellbore Reynolds number of $CO_2$ would lead to substantially greater heat loss. To test this concern, Randolph et al. (2012) calculated the effect of $CO_2$ heat loss to the surrounding rock on production pressure and temperature in a 0.25 m diameter well with a mass flowrate of 80 kg $s^{-1}$. They found that several days after the onset of production, the $CO_2$ production temperature was within 2°C of the adiabatic limiting case, due to the low thermal conductivity of the surrounding rock. More recently this concern has re-surfaced, particularly by Pan et al. (2015); however, the large frictional and heat losses reported there are due to the small pipe diameters (0.12 and 0.18 m) combined with the mass flowrates they considered, and even in the adiabatic case, those diameters are poor choices for power production (Adams et al., 2015).

In 2012, the University of Minnesota CPG research group was awarded a $1.9M National Science Foundation (NSF) Sustainable Energy Pathways (SEP) four-year grant #1230691 to sustain research. The NSF proposal laid out a detailed work plan encompassing four areas of research: Multi-phase Multi-fluid Flow (3.1), Reservoir Engineering and Management (3.2), Environmental and Technological Sustainability (3.3), and CPG Spillovers and Externalities (3.4). A breakdown of the proposed research is given in

Table 1.1. The NSF goals achieved through the papers of this dissertation, located in Sections 2 through 5, are highlighted in green in the table.

**Table 1.1: Originally Proposed Research Areas in NSF-SEP Project Proposal.** "Dept" indicates responsible department: (G)eology, (M)echanical Engineering, (E)conomics, and (P)ublic policy. If covered in this dissertation, the row is highlighted in green and "Diss. Section" indicates the corresponding section.

| NSF Section | Focus Area | Dept | Diss. Section |
|---|---|---|---|
| ***3.1*** | ***Multi-phase Multi-fluid Flow*** | | |
| 3.1.1 | 3D, Multi-fluid, Time Dependent Reservoir Modeling | G, M | 3, 4 |
| 3.1.2 | Reactive Transport: Rock-Fluid and Material-Fluid Interactions | G, M | |
| 3.1.3 | Fluid Production and Electricity Generation Over Time | G, M, E | |
| 3.1.4 | Multi-fluid Filtering and Separation | M, E | |
| 3.1.5 | Compression and Integration of Incoming $CO_2$ | M, P | |
| ***3.2*** | ***Reservoir Engineering and Management*** | | |
| 3.2.1 | Active/Dynamic $CO_2$ Plume Management | G, M, E | |
| 3.2.2 | Upconing and Well Positioning | G, M, E | 4 |
| 3.2.3 | Multilayered Systems | G, M, E, P | |
| 3.2.4 | Optimal Mass Flowrates, Thermosiphon Effects, and Maximizing Energy and Profit | G, M, E | 2, 3, 4 |
| ***3.3*** | ***Environmental and Technological Sustainability*** | | |
| 3.3.1 | CPG Flexibility and Options for Time Management of the Renewable Energy Resource | M, E | |
| 3.3.2 | $CO_2$ Reservoir Energy Storage | G, M, E, P | |
| 3.3.3 | Decision-Analytic Support for CPG Siting | G, P | |
| 3.3.4 | Contributions to the Hubert Project | P | |
| ***3.4*** | ***CPG Spillovers and Externalities*** | | |
| 3.4.1 | Enabling other Technologies and Transitions | P | 5 |
| 3.4.2 | Co-products and Complementary Benefits | P | |
| 3.4.3 | Environmental Externalities and Risk | G, E | 4 |
| 3.4.4 | Risk Management and Investment Decisions | E, P | |

In parallel with CPG research at the University of Minnesota, members of Lawrence Berkeley National Laboratory (LBNL) have also been simulating well, reservoir, and power production dynamics of CPG systems. Initially, a multi-fluid multi-phase wellbore

simulation module was developed for TOUGH2 called T2Well (Pan et al., 2010; Pan and Oldenburg, 2014). This simulator was extended first to $CO_2$-EGS reservoirs (Pan et al., 2013) and later to porous sedimentary reservoirs (CPG) (Pan et al., 2015). Pan et al. (2015) only simulated a small subset of CPG cases, particularly those with small well diameters in a single reservoir with fixed temperature and depth. It appears that their immediate efforts are focused on field testing a direct $CO_2$ turbine at a sedimentary CCUS site in Cranfield, Mississippi (Freifeld et al., 2013) and not demonstrating the large-scale applicability of CPG.

Beyond traditional CPG, advances are being made in the design and operation, or Active Reservoir Management (ARM), of sedimentary basins. Buscheck et al. (2012) found that a ring of brine production wells around a circular $CO_2$ injection well will eliminate the over-pressurization which would otherwise occur. Additionally, the produced brine could be conditioned for process use. Elliott et al. (2013) and Buscheck (2013) further found that reinjection of the produced brine in a different ring resulted in a hydraulic divide providing lateral containment of the $CO_2$ while producing significant geothermal power. Buscheck (2014) modified this design to use $CO_2$ or $N_2$ as a "gas cap" to both: pressurize the brine for artesian well production and to store energy through the compression of $N_2$ for monthly-scale energy storage.

Saar et al. (2015) expanded upon the simulations by Buscheck et al. (2012) to utilize multiple stacked reservoirs at depths of 3 and 5 km to generate power. In the best performing instance, the shallow reservoir contained both $CO_2$ and brine, while the deep reservoir contained only brine. The shallow, lower temperature brine was used to preheat the secondary fluid in the indirect Rankine cycle at the surface, augmenting system thermal efficiency while laterally containing the shallow $CO_2$.

Garapati et al. (2015) simulated the initial time-dependent injection of $CO_2$ into a brine reservoir to simulate the initial filling, heat extraction rates, and production temperatures over the reservoir lifetime. They found that an initial fixed volume of $CO_2$ is sufficient to

maintain the $CO_2$ mass fraction at the production well above 94% for the reservoir lifetime. Furthermore, they found that the volume of $CO_2$ necessary increases with $CO_2$ density and permeability. Additionally, Garapati et al. (2015) found that reservoir dip does not substantially impact heat extraction rate and that the reinjection of produced brine with the $CO_2$ substantially increases the reservoir effective permeability.

## 1.5 Impact

The research contained in this dissertation has lead to a significantly deeper understanding of $CO_2$ Plume Geothermal electricity production and its governing mechanisms. Moving forward, this work will serve as an important foundation and enable future studies. This is likely to happen in several ways.

First, comprehensive surface plant and system models have been built, tested, and compared to case studies in the literature; thus, future work may focus on the utilization of these models rather than development. Second, the results of this work may be built upon; several of the papers were published with raw supplemental data which may be used in larger-scale economic or policy analyses. Third, this work reduces the unknowns of the CPG concept by establishing electricity generation potential under a variety of conditions and therefore decreases some risk for potential developers. Finally, the work, by simply being published, increases the visibility of CPG research and increases the likelihood of its use. Ultimately, this work adds value by enabling the development of CPG as an important part of the 21$^{st}$ century's energy portfolio.

Chapter 2

# The Thermosiphon

## Preface

Since the inception of $CO_2$-based geothermal energy utilization by Brown (2000), $CO_2$ has been characterized as a beneficial geologic working fluid, in part, due to its ability to establish a buoyancy-driven flowrate, called a thermosiphon. Moreover, the thermosiphon has been hypothesized to be strong enough to power a direct turbine at the surface while eliminating pumping requirements (Atrens et al., 2009; 2010). However, the strength, variability, and dynamics of this effect were unknown.

In this paper, the thermosiphon generated by both brine and $CO_2$ is quantified, explained, and compared. The analysis uses a single value of permeability and well diameter, varying only depth and geothermal temperature gradient. The mass flowrate generated and heat extraction rate are found as a function of depth and geothermal temperature gradient, and an alternative method for characterizing the thermosiphon in terms of power (MWe) is developed, called "effective pumping power."

## Citation

Adams, B.M., Kuehn, T.H., Bielicki, J.M., Randolph, J.B., & Saar, M.O. (2014). On the importance of the thermosiphon effect in CPG ($CO_2$ plume geothermal) power systems. *Energy*, 69, 409-418. http://dx.doi.org/10.1016/j.energy.2014.03.032

# On the Importance of the Thermosiphon Effect in $CO_2$ Plume Geothermal (CPG) Power Systems

**Benjamin M. Adams[a], Thomas H. Kuehn[a]*, Jeffrey M. Bielicki[b,c], Jimmy B. Randolph[d], Martin O. Saar[d]**

kuehn001@umn.edu

[a]Department of Mechanical Engineering, University of Minnesota, 111 Church St SE, Minneapolis, MN 55455, U.S.A.

[b]Department of Civil, Environmental, and Geodetic Engineering, The Ohio State University, 2070 Neil Avenue, Columbus, OH 43210, U.S.A.

[c]John Glenn School of Public Affairs, The Ohio State University, 1810 College Road, Columbus, OH 43210, U.S.A.

[d]Department of Earth Sciences, University of Minnesota, 310 Pillsbury Drive SE, Minneapolis, MN 55455, U.S.A.

**Keywords**

Carbon Dioxide; Geothermal Energy; Carbon Dioxide Utilization; Thermosiphon; Renewable Energy; Carbon Dioxide Plume

**Highlights**

- $CO_2$ density changes create a buoyancy-driven current, or thermosiphon.
- We estimate the strength of the thermosiphon for $CO_2$ and for 20 wt% NaCl brine.
- $CO_2$ has a reservoir pressure drop approximately 3 to 12 times less than brine.
- A thermosiphon can utilize 10% of the reservoir energy for fluid circulation.
- $CO_2$ is a particularly advantageous working fluid at depths between 0.5 km and 3 km.

## Paper Summary

$CO_2$ Plume Geothermal (CPG) energy systems use $CO_2$ to extract thermal energy from naturally permeable geologic formations at depth. $CO_2$ has advantages over brine: high mobility, low solubility of amorphous silica, and higher density sensitivity to temperature. The density of $CO_2$ changes substantially between geothermal reservoir and

surface plant, resulting in a buoyancy-driven convective current – a thermosiphon — that reduces or eliminates pumping requirements. We estimated and compared the strength of this thermosiphon for $CO_2$ and for 20 weight percent NaCl brine for reservoir depths up to 5 km and geothermal gradients of 20, 35, and 50 ºC/km. We found that through the reservoir, $CO_2$ has a pressure drop approximately 3 to 12 times less than brine at the same mass flowrate, making the $CO_2$ thermosiphon sufficient to produce power using reservoirs as shallow as 0.5 km. At 2.5 km depth with a 35 ºC/km gradient – the approximate western U.S. continental mean – the $CO_2$ thermosiphon converted approximately 10% of the energy extracted from the reservoir to fluid circulation, compared to less than 1% with brine, where additional mechanical pumping is necessary. We found $CO_2$ is a particularly advantageous working fluid at depths between 0.5 km and 3 km.

## 2.1 Introduction

Geothermal power plants use the temperature difference between the Earth's hot subsurface rock and the cooler surface to generate electricity. Such systems transport thermal energy from underground to the surface using a working fluid, and in a power plant at the surface, a portion of the fluid's thermal energy is converted into electricity. The cooled working fluid is then typically reinjected into a subsurface reservoir. Conventional geothermal (hydrothermal) energy technology uses hot brine as the working fluid that is circulated through geologic formations. Moreover, these power plants are often situated in tectonically and/or volcanologically active regions where reservoir temperatures are unusually high near the Earth's surface (Blackwell and Richards, 2004). However, these unique thermal resources are limited in size and location. New technology must be developed in order to harness the estimated 200,000 exajoules (EJ) of thermal energy that may be extractable from the Earth's crust in the United States alone (MIT, 2006). This resource is much greater than the 540 EJ of primary energy that was consumed worldwide in 2011 (EIA, 2007) and is renewable on human, rather than geologic, time scales. Furthermore, compared to most other renewable

energy resources, geothermal energy is continuously available and, thus, can serve as a baseload or dispatchable power resource without requiring energy storage.

To access the high geothermal energy potential for human use, approaches have been suggested to initiate and/or widen fractures within hot, dry, low-permeability, crystalline basement rocks, thereby creating relatively small, artificial geothermal reservoirs that can support fluid flow and heat extraction (Majer et al., 2007; Smith et al., 1975). These Enhanced or Engineered Geothermal Systems (EGS) typically use water for both fracturing and advective heat energy extraction, but carbon dioxide ($CO_2$) has also been proposed as the working fluid (Brown, 2000; Pruess, 2006). While EGS has the potential to increase access to the geothermal resource base, significant technological gains are needed before EGS will be capable of extracting more than small amounts of energy (MIT, 2006).

Recently, $CO_2$ has been proposed as the subsurface working fluid for geothermal energy extraction in sedimentary basins that host natural, large-scale, high-permeability reservoirs that are overlain by, and often inter-layered with, low-permeability cap rocks (Randolph and Saar, 2011; Saar, Randolph, and Kuehn, 2012). To distinguish it from EGS using $CO_2$, this approach has been termed a $CO_2$ Plume Geothermal (CPG) energy system. As shown in Table 2.1, CPG differs from conventional hydrothermal and EGS approaches in two important ways: (1) $CO_2$ is used as the primary working fluid instead of water or brine, and (2) the $CO_2$ is circulated through naturally-permeable formations, resulting in a large-scale $CO_2$ plume. Compared to the deep formations targeted for EGS, CPG reservoirs are typically shallower (1-4 km instead of 4-7 km deep) and, hence, cooler. However, the large size and high permeability of sedimentary basins allows for much higher fluid flow and advective heat transfer rates. Importantly, the CPG approach avoids reservoir-scale hydraulic fracturing and fault shearing/dilation, which may induce seismicity (Hitzman, 2012). In addition, CPG reduces or eliminates the need for the expensive deep drilling that is typically required in EGS, and instead employs well-

established drilling techniques developed by the oil and gas industry for sedimentary basins.

| | **Energy Extraction Working Fluid** | |
|---|---|---|
| **Type of Reservoir** | Water | $CO_2$ |
| **Sedimentary Basin** (large-scale, naturally permeable, typically lower temperature) | Conventional Hydrothermal System | $CO_2$-Plume Geothermal (CPG) System |
| **Enhanced Geothermal System (EGS)** (small-scale, relatively impermeable prior to stimulation, typically higher temperature) | Conventional EGS | $CO_2$-based EGS |

**Table 2.1: The Four Types of Geothermal Systems Considered**

The sedimentary basins in which these saline aquifers reside are ubiquitous throughout the world (Metz et al., 2007) and underlie more than half of North America (Runkel et al., 2007). The salinity of such formations is high (total dissolved solids (TDS) > 10,000 PPM, i.e., far saltier than seawater), so they are unlikely to be considered a potable, or even industrial, water resource. Because $CO_2$ is less dense than the surrounding pore fluids (e.g., brine), CPG sites must be located where vertical migration of the buoyant $CO_2$ is impeded by low-permeability or impervious caprock layers overlying the permeable reservoir.

CPG can be combined with a $CO_2$ Capture and Storage (CCS) site to produce electricity and/or heat from places where $CO_2$ is injected into sedimentary basins as an approach to climate change mitigation (Global CCS Institute, 2013). This technology is an example of Carbon Capture *Utilization* and Storage (CCUS), because the coupled operation can leverage the injected $CO_2$ to produce electricity that can be used onsite and/or sold to offset the costs associated with CCS. In addition, extraction of heat from the reservoir during CPG operations reduces reservoir over-pressurization caused by $CO_2$ injection during CCS (Randolph et al., 2013), helping to ensure reservoir integrity and decreasing monitoring requirements. In addition, strategically producing brine and/or $CO_2$ from a

geologic $CO_2$ storage (GCS) site and its associated reduction in over-pressurization reduces the likelihood of inducing seismicity and can provide brine at the surface for potential use as potable or process resources (Buscheck et al., 2013). CPG may also be implemented in (partially) depleted hydrocarbon fields alongside enhanced oil recovery (EOR) operations (Saar et al., pending; Freifeld et al., 2013) and offset the hydrocarbon fuels used to power such sites.

The surface plant that produces electricity from geothermal energy can have two basic configurations: direct and indirect (binary). In an indirect system, heat is extracted from the primary subsurface working fluid to drive a secondary Rankine cycle. An indirect system is desirable when the pressure difference between primary fluid production and injection wellheads is small and the temperature difference between the fluid leaving the production well and the ambient at the surface is high. In contrast, a direct system typically expands the primary working fluid through a piece of turbomachinery in order to generate electricity, and is therefore desirable when the pressure difference between the production and injection wellheads is large. This latter condition — high pressure difference — occurs when $CO_2$ is used as the primary working fluid (even at low reservoir temperatures of $<100^oC$) and at relatively rare, high temperature ($>200^oC$) hydrothermal sites. In this paper, we exclusively model indirect geothermal systems.

Systems using $CO_2$ as the subsurface working fluid develop a buoyancy-driven thermosiphon, which occurs because of the differences in $CO_2$ density between the injection and production wells upon even a small amount of heating in the reservoir (Atrens et al., 2009; 2010) and because the high mobility (inverse kinematic viscosity) of $CO_2$ in the reservoir facilitates fluid flow. The thermosiphon can eliminate parasitic, and thus costly, pumping requirements necessary in conventional hydrothermal installations.

In this paper, we estimate the strength of this thermosiphon effect using idealized reservoir and surface plant parameters to compare the strengths of thermosiphons generated by indirect $CO_2$ and existing "state-of-the-art" 20 wt% NaCl brine indirect

geothermal power systems for depths up to 5 km and geothermal gradients of 20, 35, and 50 ºC $km^{-1}$. From these idealized cases, we draw a number of conclusions about the relative strengths of thermosiphons for subsurface systems (reservoirs) composed purely of $CO_2$ and purely of brine.

### 2.1.1 The Thermosiphon Effect in Geothermal Power Systems

The driving force of the thermosiphon is generated by the density difference of the $CO_2$ between injection and production wells. The phase of the fluid is relevant to the extent to which it affects its compressibility—supercritical $CO_2$, which typically exists throughout the subsurface portion of a CPG system, has a large variability in density, despite having liquid-like density and gas-like dynamic viscosity. When fluid flows upward in a production well, the pressure decreases because the increase in elevation reduces the hydrostatic pressure of the fluid and pressure losses accumulate due to friction with the pipe wall. For a static fluid, the pressure losses are zero and the change in pressure can be calculated from the Bernoulli equation:

$$\int_1^2 \frac{dP}{\rho} = g(z_2 - z_1) \qquad (2.1)$$

When the density of the fluid is nearly constant with changes in temperature and pressure (e.g., with liquid brine), the integral in Equation (2.1) can be eliminated and the pressure change, $\Delta P$, becomes the product of fluid density, $\rho$, the Earth's gravitational acceleration constant, $g$, and the change in elevation, $z_2$-$z_1$, between the surface, $z_2$, and the reservoir, $z_1$. Thus, for conventional hydrothermal systems, the pressure changes in the production and injection wells roughly offset each other. Consequently, the pressure difference between the injection and production wellheads is close to zero, and the fluid will be stagnant if not actively pumped. In contrast, when the fluid density changes substantially with pressure (e.g., with supercritical $CO_2$ as the working fluid), the pressure difference between the wellheads can be quite large. This pressure difference drives the $CO_2$ thermosiphon.

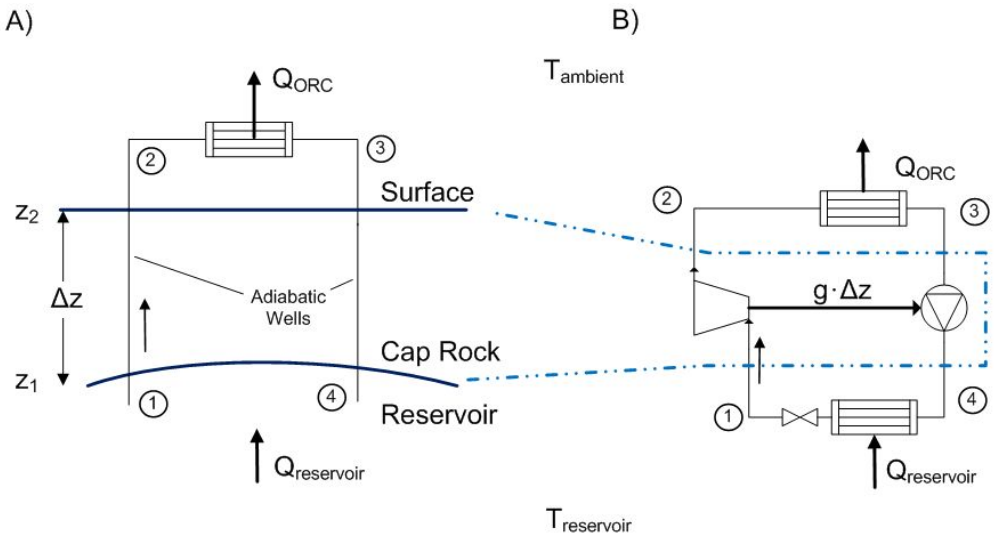


**Figure 2.1: A) A simple binary geothermal cycle that supplies heat to an Organic Rankine Cycle ($Q_{ORC}$).** Heat enters the cycle in the reservoir ($Q_{reservoir}$), located a depth, $\Delta z=z_2-z_1$, below the surface. The overall efficiency of the system is governed by the difference in temperature of the resource ($T_{reservoir}$) and the sink ($T_{ambient}$). **B) An equivalent power cycle at a constant elevation with the same states as Panel A.** The change in energy of the fluid as it expands in the production well ($g \cdot \Delta z$) is equal, but opposite in sign, to the energy which compresses the fluid in the injection well.

A simplified binary geothermal system is shown in Figure 2.1A. The hot geothermal fluid is produced from the reservoir at State 1 then rises through the production well to the surface (State 2). The working fluid next passes through a heat exchanger where thermal energy is transferred to an Organic Rankine Cycle (ORC) and leaves the heat exchanger at ambient temperature at State 3, where the cool fluid is injected back into the subsurface. The pressure of the fluid increases as it approaches State 4 in the subsurface reservoir. The wells are assumed to be adiabatic because the low thermal conductivity of the surrounding rock minimizes thermal losses (Randolph et al., 2012). An energy balance between States 1 and 2, neglecting small changes in kinetic energy, shows that the fluid's specific enthalpy, *h*, changes by

$$h_2 - h_1 = g(z_1 - z_2) \quad . \qquad (2.2)$$

Equations (2.1) and (2.2) show that the fluid in the production well undergoes an expansion with a change in enthalpy equal to the change in potential energy. The relation for a non-isentropic expansion process is shown in Equation (2.3), where an efficiency parameter, $\eta$, has been added to account for frictional wellbore pressure losses.

$$\eta \int_1^2 \frac{dP}{\rho} = h_2 - h_1 \qquad (2.3)$$

This part of the system can be represented by a turbine at a constant elevation, as shown in Figure 2.1B. Similarly, the process of increasing the fluid pressure and enthalpy in the injection well is a compression process, which is represented by a shaft-driven pump shown in Figure 2.1B. The isentropic change in enthalpy in both wells is equal in magnitude but opposite in sign, so the energy transfer can be represented by a shaft connecting the turbine (between States 1 and 2) and pump (between States 3 and 4), as shown in Figure 2.1B. Consequently, Figure 2.1B represents an equivalent power system, without any elevation change, that can be used to model a binary geothermal system.

When the fluid densities differ between the injection and production wells, the pressure changes in the wells will also differ. For example, in a 2.5 km deep stagnant $CO_2$ system, with a 35 $^oC\ km^{-1}$ thermal gradient, the average injection well fluid density is 880 kg $m^{-3}$ while the average production well fluid density is only 520 kg $m^{-3}$. In either well, the change in potential energy is approximately 25 kJ $kg^{-1}$, but the change in injection and production well pressures is 21.6 MPa and 12.7 MPa, respectively. The $CO_2$ at States 1 and 4 is at 25 MPa, but the production wellhead pressure is 12.3 MPa, and the injection wellhead pressure is 3.4 MPa. As much as 8.9 MPa of "excess pressure" is, thus, available at the surface, and could be used to move the fluid within the system or, in a direct power plant, to generate electricity. The fluid mass flowrate through the cycle will increase until frictional losses equal the excess pressure. Consequently, the varying density of the $CO_2$ system generates a thermosiphon. In contrast, the density of brine is

much less sensitive to temperature and pressure and, thus, changes little throughout the cycle and provides little thermosiphon effect.

## 2.2 Methods

In the following, we describe our numerical modeling methods applied to the three main components of the geothermal power system: reservoir, wells, and surface plant.

### 2.2.1 Reservoir Modeling

We use TOUGH2 (Pruess, 2004) with the ECO2N equation of state module (Pruess, 2005) to numerically model a single production-injection well pair within the flat homogeneous sedimentary basin geothermal reservoir, employing a standard five-spot well pattern and taking advantage of symmetry to efficiently simulate the geology, as presented in previous publications (e.g. Pruess, 2006; Randolph and Saar, 2011). During simulations, the reservoir pore fluid is either all $CO_2$ or all 20 wt% NaCl Brine. Thus, in $CO_2$ simulations, brine displacement by $CO_2$ is not simulated. Rather, we assume that a sufficiently large $CO_2$ plume has been established in the reservoir before heat extraction commences (Randolph and Saar, 2011), and thus any localized clogging due to salt precipitation (Borgia et al., 2012) has been remedied. To avoid running the TOUGH2 model for every mass flowrate required for wellbore and surface plant simulations, the pressure losses are estimated from the results of six TOUGH2 mass flowrate simulations, using Darcy's Law for laminar flow through porous media,

$$\Delta P = \left[ \frac{\mu L}{\rho \kappa A} \right] \dot{m} \quad . \tag{2.4}$$

Equation (2.4) shows the linear relationship between working fluid mass flowrate, $\dot{m}$, and pressure difference, $\Delta P$, in the reservoir between the injection and production wells, when the term in the brackets, the average specific inverse mobility, $M$, is constant. $M$ =

*(μL)/(ρκa)* is the product of the inverse mobility, or kinematic viscosity, $\mu/\rho$, and reservoir properties, $L/(\kappa A)$, and accounts for how these reservoir and fluid properties resist fluid flow. *M* is constant for a given reservoir permeability, depth, and temperature. To note, the actual specific inverse mobility varies substantially throughout a reservoir and thus the average value of TOUGH2 simulations is used to interpolate other mass flowrates.

| | |
|---|---|
| Working Fluid I | 100% $CO_2$ |
| Working Fluid II | 20 wt% $H_20$-NaCl (brine) |
| $\eta_{orc}$ | 0.33 |
| $D$ | 0.28 m |
| $g$ | 9.81 m $s^{-2}$ |
| $L_{surface}$ | 707 m |
| Reservoir Area | 1 km x 1 km |
| Reservoir Thickness | 300 m |
| $P_{reservoir}$ | Hydrostatic ( $\rho_{water} \cdot g \cdot \Delta z$) |
| $T_{ambient}$ | 15 ºC |
| $T_{gradient}$ | 20, 35, & 50 ºC $km^{-1}$ |
| $z$ | 1 km to 5 km |
| $\varepsilon$ | 0.000055 m |
| $\kappa$ | 5 x $10^{-14}$ $m^2$ |
| $\rho_{water}$ | 1000 kg $m^{-3}$ |
| $\Phi$ | 0.1 |
| | |
| *Reservoir Boundary Conditions* | |
| Lateral | No fluid or heat flow |
| Vertical | No fluid flow, heat conduction using TOUGH2 semi-analytic model |

**Table 2.2: Model Parameter Values used in Simulations**

To find *M*, the pressure loss in the reservoir is determined by running TOUGH2 simulations at six mass flowrates at a given permeability, $\kappa$, depth, and pressure, for $CO_2$ and brine. Reservoir-specific parameters are provided in Table 2.2. For each parameter combination, a linear regression of the form $\Delta P = \alpha + \beta \cdot \dot{m}$ is performed on the generated data with the intercept, $\alpha$, set to zero. The resulting regression slope, $\beta$, is the specific inverse mobility, *M*. The average uncertainty of *M* for fourteen such regressions

is 0.4%, indicating predicted pressure loss values, using *M*, will be very close to results from actual TOUGH2 simulations. The calculated values of *M* are shown in Figure 2.2.

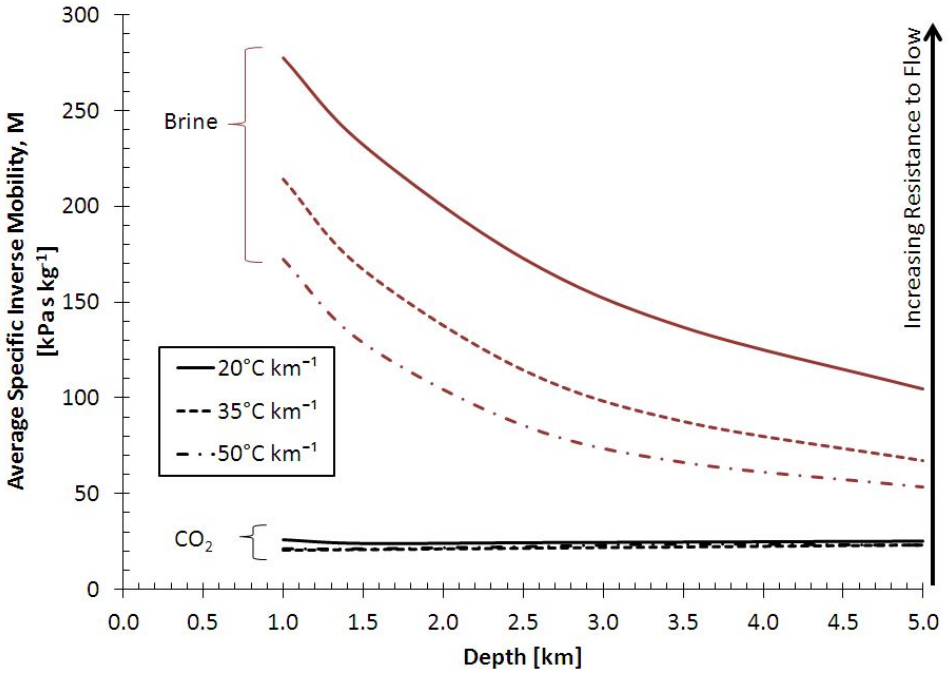


**Figure 2.2: Average specific inverse mobility, *M*, for the reservoir of interest given in Table 2.2.** When multiplied by the mass flowrate, *M* gives the pressure difference across the reservoir

The values of *M* for $CO_2$ are relatively constant near a value of 22 kPa s $kg^{-1}$ throughout the range of depths and geothermal gradients considered here. In contrast, the dynamic viscosity, $\mu$, of brine decreases with increasing temperature. Consequently, resistance to flow, expressed by *M*, decreases with depth for brine but is always higher than that of $CO_2$ over the conditions examined here that are representative of U.S. continental sedimentary basins. For example, at a depth of 1 km, *M* for brine is 7 to 12 times greater than that of $CO_2$, while at 5 km, *M* for brine is still 2.5 to 5 times that of $CO_2$. As a result, the difference between the thermosiphon performance of $CO_2$ and brine is significant at all investigated depths (1-5 km) but more pronounced at shallower depths. To note, pressure losses are estimated to have a *numerical simulator uncertainty* of 6%, based on the benchmarking of eight reservoir simulator performances of $CO_2$-enhanced gas recovery by Class *et al.* (2009).

We use a steady-state energy balance to determine the heat extraction rate from the reservoir, $Q_{reservoir}$. The rate of heat removed is the product of the working fluid mass flowrate, $\dot{m}$, and its enthalpy difference in and out of the reservoir, as shown in Equation (2.5). Enthalpy is fluid property based on its thermal and pressure energy content, found from lookup tables.

$$Q_{reservoir} = \dot{m}\left(h_{out,reservoir} - h_{in,reservoir}\right) \qquad (2.5)$$

The temperature of the working fluid produced from the reservoir (State 1, Figure 2.1A) is fixed at a value found by multiplying the reservoir depth by the geothermal gradient and adding the assumed average ambient air temperature. Consequently, we assume that the temperature of the fluid as it enters the production well is the same as the initial reservoir temperature; the large injection-production well spacing (0.71 km) and low, laminar fluid flowrates are sufficient to increase the temperature of the injected $CO_2$ to the initial reservoir temperature by the time it reaches the production well. The average specific heat, $c_{p,ave}$, of the working fluid as it flows through the reservoir is calculated by Equation (2.6).

$$c_{p,ave} = \frac{\left(h_{out,reservoir} - h_{in,reservoir}\right)}{\left(T_{out,reservoir} - T_{in,reservoir}\right)} \qquad (2.6)$$

### 2.2.2 Well Modeling

To simulate wellbore flow, the injection and production wells are divided into 100 m segments and numerically integrated. The element length is chosen to balance computational time and accuracy, ensuring that the wellbore pressure drop is within 1% of the value found using a very finely discretized test model. Hence, a 1% *well discretization uncertainty* is used. We employ $CO_2$ properties from Span and Wagner (1996) in simulations using Engineering Equation Solver (EES). Brine properties are determined from relations provided by Driesner (2007) and the IAPS-84 Steam Tables

(Haar et al., 1984). Across each element, an energy balance, momentum balance, and continuity equation are used to find the resulting fluid state ($i+1$) from the initial state ($i$), as shown in Equations (2.7-2.9) which are adiabatic and neglect the effect of kinetic energy; in a 2.5 km, 0.27 m production well with a $CO_2$ mass flowrate of 170 kg $s^{-1}$, the velocity varies from 5.2 to 7.3 m $s^{-1}$, which is a kinetic energy change of 0.05% of the total energy change.

$$h_i + gz_i = h_{i+1} + gz_{i+1} \tag{2.7}$$

$$P_i + \rho_i g z_i = P_{i+1} + \rho_i g z_{i+1} - \Delta P_{losses} \tag{2.8}$$

$$\dot{m}_i = \rho_i A_i V_i \tag{2.9}$$

The frictional pressure losses are determined from the Darcy-Weisbach relation,

$$\Delta P_{losses} = f \frac{L_{pipe}}{D} \rho \frac{V^2}{2} \quad , \tag{2.10}$$

where the friction factor, $f$, is taken from the Moody Chart (Moody, 1944). To minimize piping at the surface, wells are assumed to be drilled at an angle from a single, central surface location, emanating out to the corners, which have a lateral distance, $L_{surface}$, and a depth, $z_2$-$z_1$ from the surface. The length of the well, $L_{pipe}$, is thus the hypotenuse of the triangle with sides $L_{surface}$ and z. For instance, $L_{surface}$ is always 0.71 km, while at a depth of 2.5 km, a well length of $L_{pipe} = (2.5^2 + 0.71^2)^{0.5} = 2.6$ km is needed.

To find the friction factor, $f$, a pipe roughness, $\varepsilon$, for Bare Cr13 oil piping is used (Farshad and Rieke, 2006). The roughness is 10 μm larger than the 45 μm value often used for Schedule 40 pipe, as proposed by Moody (1944), and used in the Geothermal Electricity Technology Evaluation Model (GETEM) (DOE, 2012). The use of a larger $\varepsilon$ results in a conservatively high estimate of the pressure drop in the wells. To determine

the sensitivity of the system to frictional pipe losses, we use a *surface roughness uncertainty* of 10 μm when calculating thermosiphon mass flowrates.

Previous analyses have suggested that complications may arise in the production well as a result of cooling of $CO_2$ due to the Joule-Thomson effect (Mathias et al., 2010). This effect, however, relates to a non-isentropic (irreversible) constant-enthalpy process. Even though some irreversibilities will be introduced and result in a frictional pressure drop, very large throttling pressure reductions (~5 MPa) only reduce the fluid temperature modestly and therefore pose little threat to production (Mathias et al., 2012; Oldenburg, 2007; Singh et al., 2011). The majority of the temperature reduction occurs from a change in pressure as the enthalpy decreases and the fluid expands during production in the well. Our analysis accommodates both the irreversibility and the enthalpy change by using thermo-physical property data in conjunction with the Darcy-Weisbach relation for the pressure drop. Further, the CPG loop does not experience substantial throttling of fluid at any one specific location (e.g., production well), and $CO_2$ heat addition and removal only occur within the surface plant and reservoir, respectively.

### 2.2.3 Surface Plant Modeling

At the surface, heat is extracted from the working fluid to generate electricity using an Organic Rankine Cycle (ORC) (DiPippo, 2008). The fluid reinjection temperature at the surface (State 3, Figure 2.1A) is taken to be the average ambient air value. Minimal surface piping exists, thus heat transfer and pressure losses in surface piping are neglected. The pressure loss within the surface heat exchanger is assumed to be small relative to the kilometer-scale length of the wells. For example, in a well extending to 2.5 km depth at a temperature gradient of 35 °C $km^{-1}$, the pressure loss in the production well is 2690 kPa, much larger than in typical heat exchangers

$$\eta_{th} = \frac{P_{net}}{Q_{reservoir}} = \eta_{ORC}\eta_{carnot} \quad , \qquad (2.11)$$

$$\eta_{carnot} = 1 - \frac{T_{ambient}}{T_{surface\,(\text{Fig1,State2a})}} \qquad (2.12)$$

$$P_{net} = \eta_{ORC}\, \eta_{carnot}\, Q_{reservoir} \quad . \qquad (2.13)$$

The power produced by the system is calculated with Equation (2.13), where the thermal efficiency (Equation 2.11) is a product of Carnot efficiency (Equation 2.12) and a constant ORC efficiency, $\eta_{orc}$. The ORC efficiency is taken to be 33% of the Carnot efficiency based on thermal efficiency values reported for similarly-sized binary geothermal power plants, such as the Heber plant in Imperial Valley, California (10.5% net thermal efficiency, 31% of the Carnot efficiency (DiPippo, 2008)) the Megamax plant in East Mesa, California (12.0% net thermal efficiency, 33% of the Carnot efficiency (DiPippo, 2008)), and the Dora II plant in Aydin, Turkey (10.7% net thermal efficiency, 31% of the Carnot efficiency (Ganjehsarabi et al., 2012)).

The Carnot efficiency (Equation 2.12) is determined using the temperature of the produced fluid at the surface (Figure 2.1, State 2a) and the ambient air temperature. The temperature of brine is nearly constant in the production well, and thus, its production temperature is assumed to equal the reservoir temperature. In contrast, the temperature of $CO_2$ decreases as it rises through the production well. Thus to facilitate a proper comparison between these working fluids, the fluid temperature entering the ORC (State 2a) is used to calculate the Carnot efficiency rather than the reservoir temperature.

## 2.3 Results and Discussion

We present our results in four parts. First, we show the mass flow and heat extraction rates for the range of temperatures and depths considered in Section 2.3.1 for both brine and $CO_2$ systems. These values are then used to calculate the power generated (Section 2.3.2). In Section 2.3.3, we introduce a concept called "Effective Pumping Power," which is used to quantify the strength of a thermosiphon in terms of parasitic power

saved. Last, we show the sensitivity of the system to variations in reservoir permeability in Section 2.3.4.

### 2.3.1 Mass Flow and Heat Extraction Rates

The steady-state mass flowrates of the $CO_2$ and brine systems are shown in Figure 2.3. The steady-state mass flowrate is a result of the thermosiphon—the mass flowrate at which the "excess pressure" equals the frictional losses within the piping and reservoir. The lighter bounds around each curve represent the combined uncertainty from three sources, as described previously: a 6% reservoir *simulator uncertainty* found from Class *et al.* (2009), a 1% *well discretization uncertainty* in pressure, and a 10 μm pipe *surface roughness uncertainty*. Uncertainties are numerically estimated values, propagated using the Taylor series method.

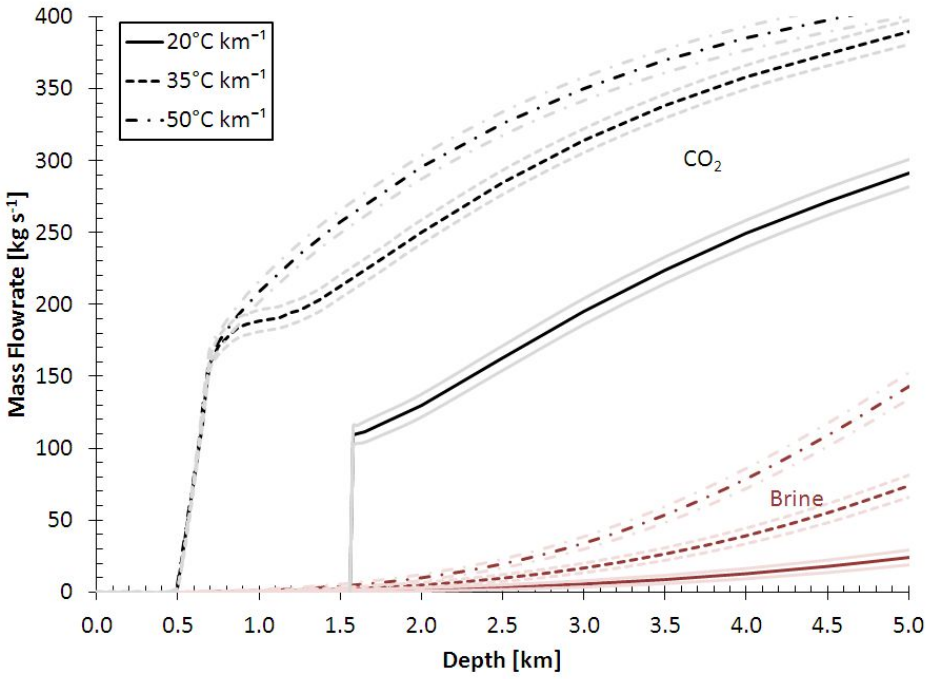


**Figure 2.3: Thermosiphon-generated mass flowrates at varying reservoir depths and geothermal temperature gradients.** Note that the flowrates are considerably higher in all cases for $CO_2$ than for brine, as expected from Figure 2.2. The discontinuities shown in the $CO_2$ curves are caused by conditions near the critical point.

Mass flowrates for both fluids increase monotonically with increasing depth (Figure 2.3). $CO_2$ systems exhibit significant thermosiphon-induced circulation at depths as shallow as 0.5 km. Despite $CO_2$ not being supercritical at such shallow depths, its density variation is sufficient to drive fluid circulation. The sharp increase in $CO_2$ mass flowrates near 0.5 km (for 35 $^oC$ $km^{-1}$ and 50 $^oC$ $km^{-1}$ cases) occurs because the circulating $CO_2$ is near the critical point (7.4 MPa) and, thus, its density is very sensitive to temperature. As an example of the difference between $CO_2$ and brine thermosiphon performances, consider the case of a geothermal gradient of 35 $^oC$ $km^{-1}$ at 1 km depth: the average injection and production well density of $CO_2$ are 860 kg $m^{-3}$ and 335 kg $m^{-3}$, respectively, while for brine, they are 1149 kg $m^{-3}$ and 1133 kg $m^{-3}$, respectively. These density differences produce a mass flowrate of 188 kg $s^{-1}$ for $CO_2$ but only 1.7 kg $s^{-1}$ for brine.

For the 20 $^oC$ $km^{-1}$ $CO_2$ system, a step-function change in mass flowrate occurs near 1.5 km. At shallower depths, the temperature at the production wellhead (State 2) is below the ambient air temperature so that heat extraction to an ORC and the associated density increase is not possible. However if an ambient air temperature below the $T_{ambient}$ = 15 $^oC$ value used in this model is chosen, non-zero flowrates at shallower depths are possible.

The uncertainty of the $CO_2$ mass flowrate in all cases is nearly constant, averaging ±7.2 kg $s^{-1}$, and is dominated by the TOUGH2 6% simulator uncertainty, which averages ±5.2 kg $s^{-1}$ and contributes about 60% to the overall model uncertainty. The pipe roughness and well numerical integration uncertainty contribute about 20% each. Conversely, brine uncertainty scales with mass flowrate and is approximately linear from ±0 kg $s^{-1}$ to ±9 kg $s^{-1}$ at 1 km and 5 km depth, respectively. For brine, the uncertainty from well numerical integration accuracy constitutes approximately 70% of the overall uncertainty, followed by 30% from TOUGH2 simulator uncertainty, and 0% from pipe roughness. These component uncertainties reveal the differing sensitivities of mass flowrate in the $CO_2$ and brine systems. The well numerical integration accuracy affects the accuracy of the thermosiphon pressure potential generated at the surface between the injection and production wells; while the TOUGH2 simulator uncertainty and pipe roughness

uncertainty affect the pressure losses generated by fluid movement throughout the system. As the brine system has difficulty generating a thermosiphon, it follows that the flowrate of the system would be most sensitive to the numerical integration accuracy. Likewise, the $CO_2$ system generates a large thermosiphon whose rate is sensitive to the factors which affect pressure loss (i.e., TOUGH2 uncertainty and pipe roughness values).

The above analysis has used the given parameters for pipe diameter and roughness and reservoir permeability established in this study from Table 2.2. Changing these values may substantially affect system performance. The pipe diameter has a fifth-order relationship with pressure loss in the Darcy-Weisbach equation. For example, increasing the pipe diameter 10% from 0.28 m to 0.31 m in the 35 $^{o}$C km$^{-1}$, 2.5 km $CO_2$ scenario increases the mass flowrate 15%, from 285 kg s$^{-1}$ to 328 kg s$^{-1}$. Similarly, an order of magnitude increase in permeability to 5x10$^{-13}$ m$^2$ increases the mass flowrate 45% to 417 kg s$^{-1}$. The parameters chosen in this paper are typical values for sedimentary basins (Randolph and Saar, 2011) and, thus, permit general conclusions. Additionally, future studies could build upon this work by investigating heterogeneous and sloped reservoirs, which may favorably affect the thermosiphon-induced mass flowrate.

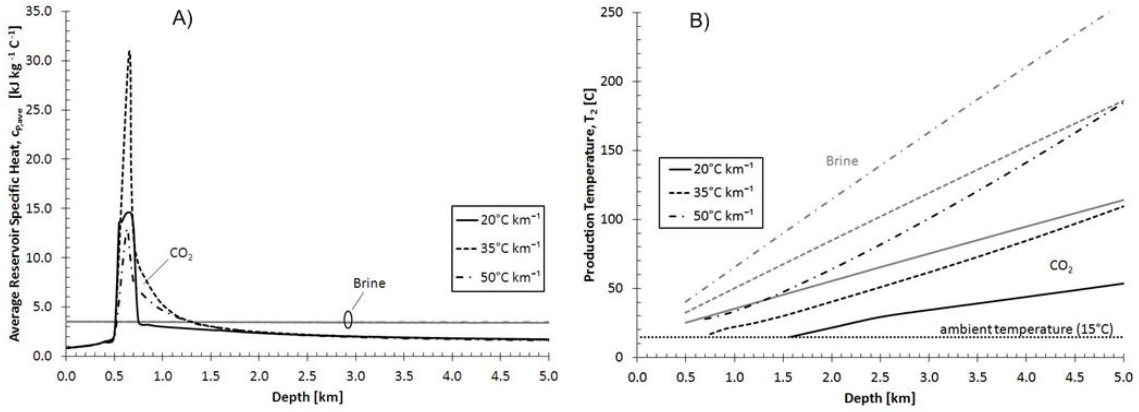


**Figure 2.4: A) Average specific heat in $CO_2$ or brine geothermal reservoirs at varying depths and geothermal gradients.** The spikes in $CO_2$ specific heat values occur around the fluid's critical point. The brine curves for the different geothermal gradients collapse to a single line. **B) Surface production temperature, $T_2$, of $CO_2$ or brine systems at varying depths and geothermal gradients.** Brine temperature is assumed constant in the production well and therefore also indicates reservoir production temperature for both $CO_2$ and brine cases.

The average working fluid specific heats under a given reservoir depth and temperature are evaluated by dividing the fluid enthalpy difference across the reservoir by the associated temperature change, as shown in Equation 2.6. As shown in Figure 2.4A, except for spikes near the critical point, where the average specific heat of $CO_2$ can be almost ten times that of brine, the average specific heat of $CO_2$ is generally below that of brine (3.5 kJ $kg^{-1}$ $C^{-1}$). However, the relatively high mass flowrate induced by the $CO_2$ thermosiphon (Figure 2.3) offsets the fluid's generally lower specific heat (Figure 2.4A) to generate higher heat extraction rates (Figure 2.5).

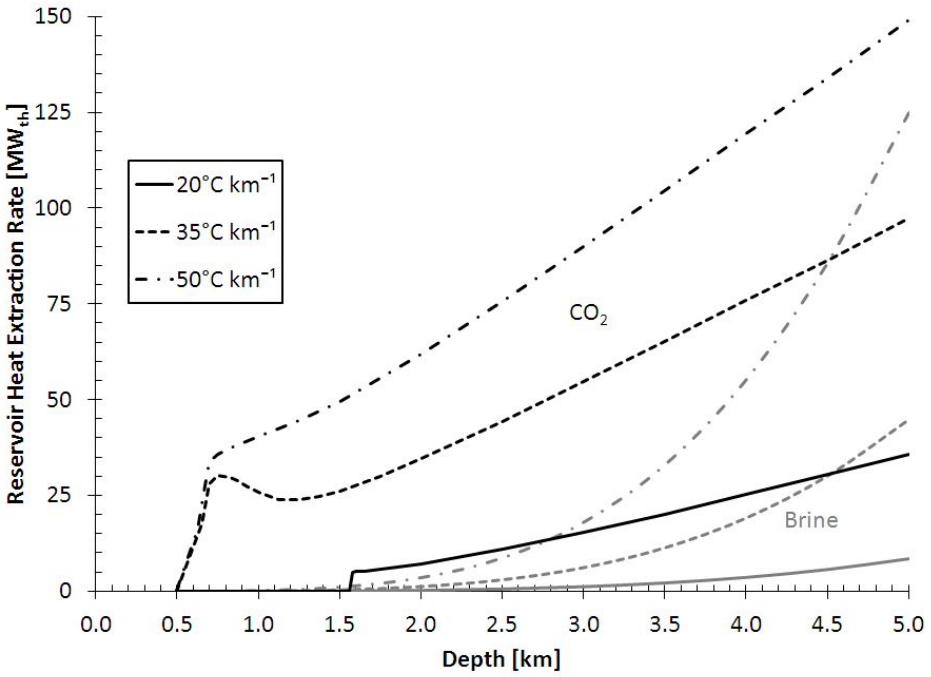


**Figure 2.5: Reservoir heat extraction rates at varying depths and geothermal gradients.** For the sedimentary basin depths (0.5-5.0 km) and geothermal gradients (20-50 $^{o}$C $km^{-1}$) used here, the heat extraction rates achieved by $CO_2$ always exceed those for brine.

At a depth of 1 km with a 35 $^{o}$C $km^{-1}$ geothermal gradient, a $CO_2$ thermosiphon extracts 300 times more thermal energy than a brine system; however, as shown in Figure 2.4B, the $CO_2$ resource temperature is only 50 $^{o}$C, resulting in a $CO_2$ production temperature of 22 $^{o}$C. Consequently, an Organic Rankine Cycle operating under these conditions has a

Carnot efficiency of 2.4% (Equation 2.12) and a resultant thermal efficiency of 0.8% (Equation 2.11), generating little, if any, power. However when indirect system thermal efficiencies are low, a direct $CO_2$ system, which can directly utilize the thermosiphon pressure generated at the surface, could produce more power.

Figure 2.5 also shows that the heat extraction rate using brine increases more rapidly with depth than the rate using $CO_2$. However, even though the difference narrows with depth, $CO_2$ consistently extracts at least several times more heat than does brine (e.g., approximately four times more at a depth of 4 km). Hence, given comparable thermal efficiencies, a $CO_2$ system will generate accordingly more power than a brine system.

A local peak in heat extraction is evident in Figure 2.5 for the $CO_2$ system and a geothermal gradient of 35 ºC $km^{-1}$ between the depths of 700m and 1000m. These local maxima and minima are primarily a consequence of a spike in $CO_2$ specific heat, shown in Figure 2.4 at a depth of ~700 m, despite increases in mass flowrate as depth increases.

### 2.3.2 Power Generation

To demonstrate the strength of the thermosiphon, Figure 2.6 shows the power generated by an indirect geothermal system without pumping for both $CO_2$ and brine. Power is calculated as the product of the heat extraction rate and 33% of the Carnot efficiency (Equation 2.13). For a given depth and geothermal gradient, a $CO_2$ thermosiphon can generate more power than a brine thermosiphon, except for the most extreme conditions. At a depth of 5 km and a 50 ºC $km^{-1}$ thermal gradient, the reservoir temperature has increased enough to provide a substantial thermosiphon, which, when combined with the larger specific heat and thermal efficiency of brine, generates more power than a $CO_2$ system. In most cases, however, the power generation of a $CO_2$ system is several times larger than brine—at a 2.5 km depth and a geothermal gradient of 35 $^oC$ $km^{-1}$, for example, brine produces just ~0.2 MWe while electrical power generated for a $CO_2$ system is ~8 times larger (~1.6 MWe).

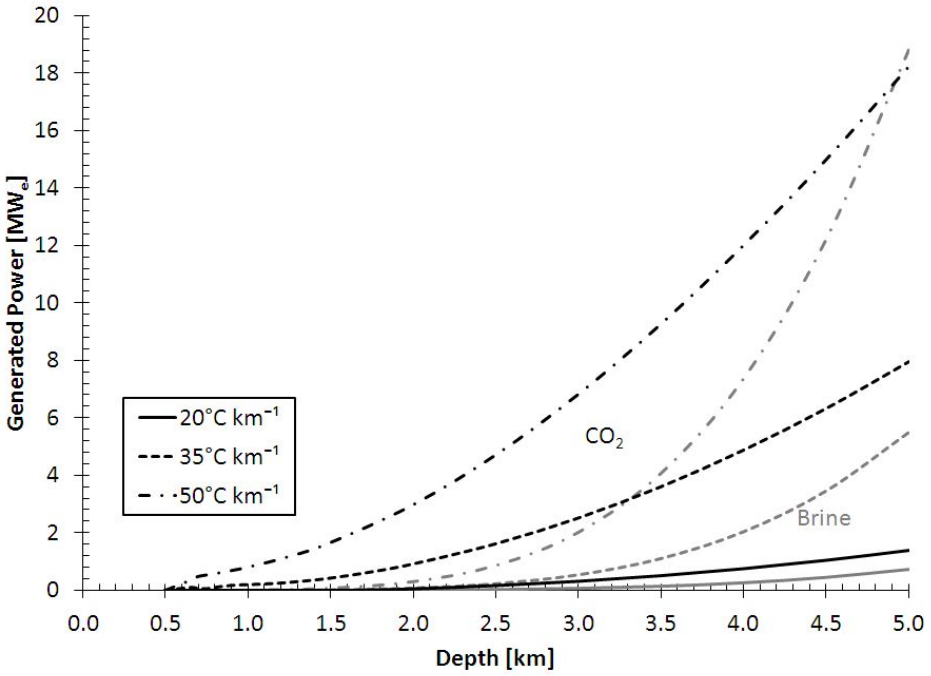


**Figure 2.6: Organic Rankine cycle power generation per injection-production well pair at varying reservoir depths and thermal gradients.** Note that the $CO_2$ system can generate more power than the brine system except for the most extreme case near a 5 km depth and a geothermal gradient of 50 ºC $km^{-1}$.

The results shown in Figure 2.6 compare the power that could be generated relying only on the mass flowrates provided by the thermosiphon; they are not optimized for maximum power production. For example, a $CO_2$ system could have higher efficiency, especially at shallow depths, with a direct cycle turbine, while a brine system could produce more net power by adding pumps to increase the mass flowrate.

This analysis assumes that the power plant cools the fluid to ambient air temperature prior to reinjection in order to maximize the heat extraction for electricity generation and to maximize density of the working fluid. However, conventional brine systems generally reinject the fluid at high temperatures, often above 50 °C, to prevent the precipitation of amorphous silica (DiPippo, 2008). In contrast, $CO_2$ is a poor solvent for minerals, thus a $CO_2$ system can cool the fluid to within a few degrees of the ambient

temperature without concern for mineral precipitation. As a consequence this analysis determines the maximum brine heat extraction, thermosiphon, and power production rates without concern for precipitation constraints.

### 2.3.3 Effective Pumping Power

As shown in Section 2.3.1, both $CO_2$ and brine systems can generate thermosiphons with significant mass flowrates without the use of pumps. Here we develop and apply a method to quantify, in megawatts (MW), the strength of the thermosiphon by estimating the effective pumping power that it provides. This effective pumping power is the amount of electrical energy required by an isentropic pump to drive the same thermosiphon-induced mass flowrate through an equivalent amount of pipe but at constant elevation. Figure 2.7 illustrates the approach used to calculate the effective pumping power.

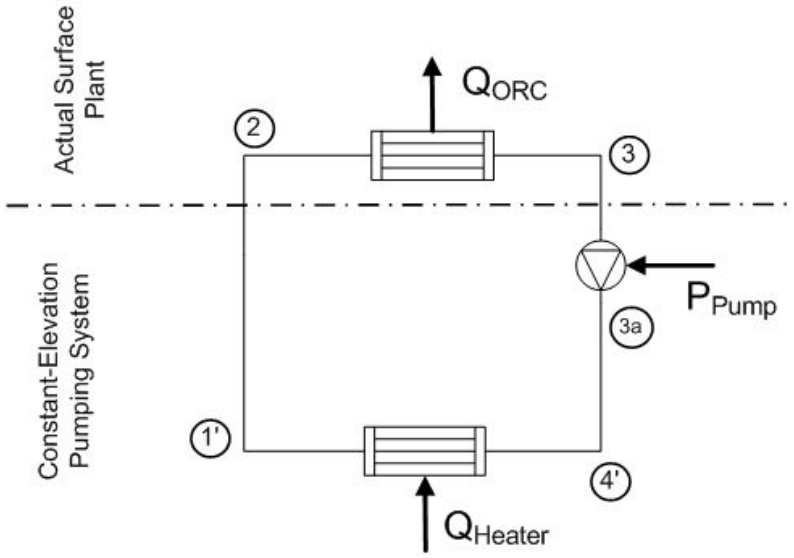


**Figure 2.7: Schematic used to calculate the effective pumping power.** The effective pumping power is the amount of electrical energy that would be needed to pump the system at the thermosiphon-induced mass flowrate through an equivalent amount of pipe if the elevation of the system remained constant, and no thermosiphon was generated.

States 2 and 3 (Figure 2.7) are the same as in the indirect system (Figure 2.1), but States 3a, 4', and 1' are unique to this constant-elevation configuration. The amount of piping from States 3a to 4'and 1' to 2 equals that in the system modeled in Figure 2.1 and all previous calculations. The pressure change from States 4' to 1' is identical to States 4 to 1 in Figure 2.1. An isentropic pump is added at the surface (States 3 to 3a) to provide a pressure differential otherwise created by the thermosiphon, thus the resulting effective pump power equals the energy needed to overcome the friction throughout the system, which approximately equals the energy exerted by the thermosiphon. The effective pump power is the product of thermosiphon mass flowrate and the enthalpy differential across the pump (Equation 2.14), which is roughly the pressure change divided by density (Equation 2.3).

$$P_{\text{effective pump power}} = \dot{m}_{\text{thermosiphon}} \cdot \left(h_{3a} - h_3\right) \qquad (2.14)$$

Using the mass flowrates and state points from the results presented above in Figure 2.3, the effective pumping power is calculated (Figure 2.8).

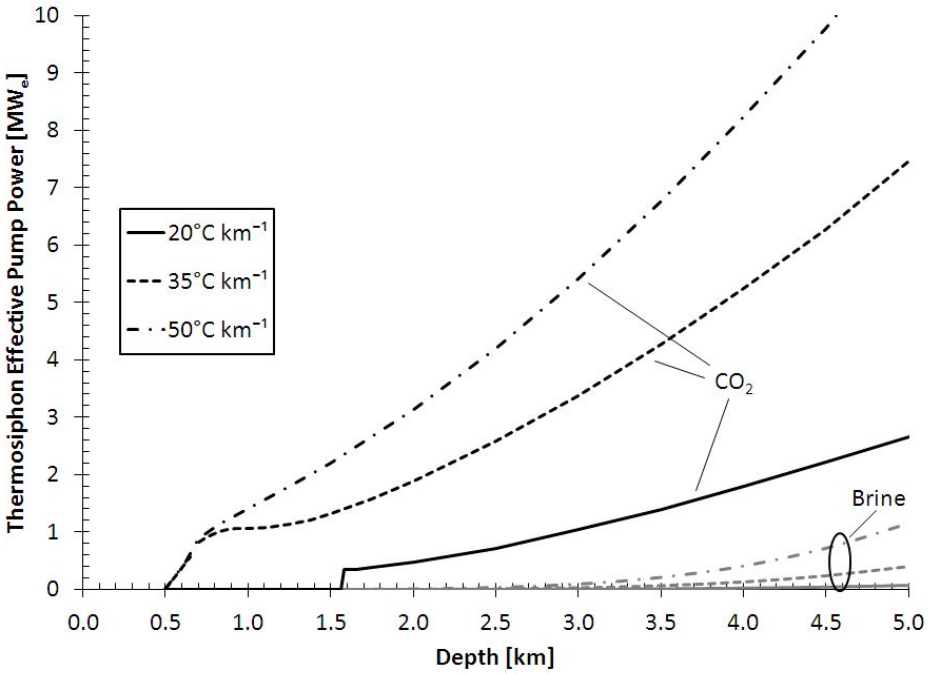


**Figure 2.8: Effective pumping power generated by the thermosiphon at varying depths and geothermal gradients**

The thermosiphon effective pumping power is the power exerted by the fluid on itself, due to the thermosiphon effect, to circulate through the well piping and reservoir. $CO_2$ generates far more effective pumping power, which can be a significant fraction of the total energy extracted from the reservoir, than brine. For example, for a geothermal gradient of 35 ºC $km^{-1}$ and a depth of 5 km, the $CO_2$ effective pumping power is 8% of the heat extracted while for brine, it is < 1%. Thus, the $CO_2$ thermosiphon is able to provide most of the pumping needed to optimize power production for such reservoir conditions, while brine must be supplemented by mechanical pumps, a parasitic power requirement.

### 2.3.4 Thermosiphon Strength and Reservoir Permeability

Of all system parameters, reservoir permeability has the greatest impact on the strength of the thermosiphon. Figure 2.9 presents the results of a sensitivity analysis of the thermosiphon mass flowrate for a half order of magnitude variation in permeability (on a log scale) centered about our selected value of 5 $x10^{-14}$ $m^2$ that was used in previous

figures, i.e., from 2.8 x$10^{-14}$ $m^2$ to 8.9 x$10^{-14}$ $m^2$. Even with this variation, $CO_2$ mass flowrates are always greater than those for brine.

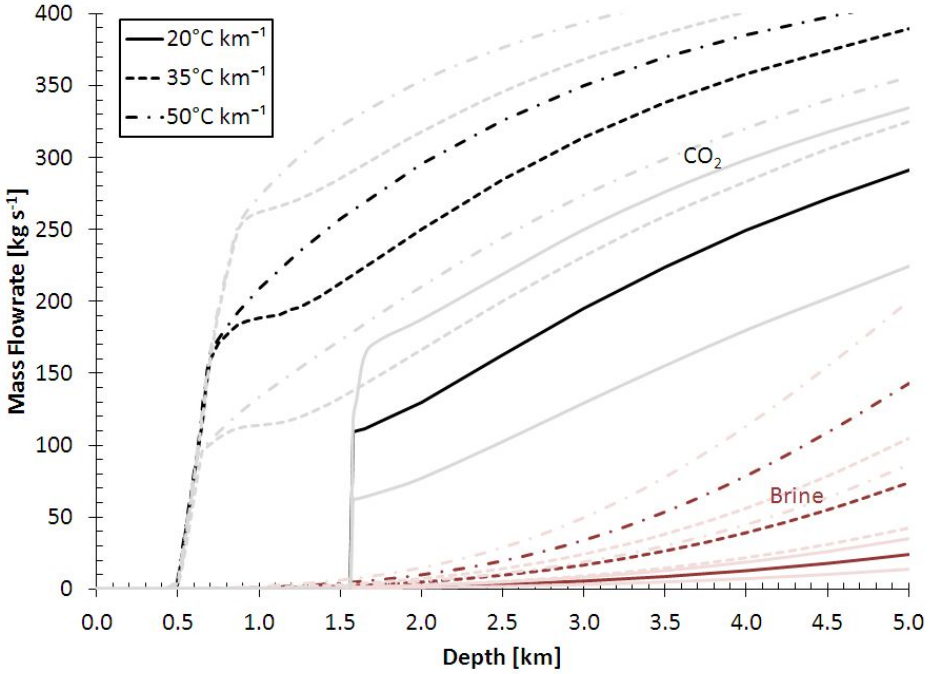


**Figure 2.9: Thermosiphon mass flowrate sensitivity to a half order of magnitude variation in reservoir permeability.** The dark lines are the flowrates at 5x$10^{-14}$$m^2$, while the upper and lower light lines represent the flowrates at 8.9x$10^{-14}$ $m^2$ and 2.8x$10^{-14}$ $m^2$, respectively

## 2.4 Conclusions

We have shown the theoretical basis for, and relative strength of, the thermosiphons established by two different fluids that can be used to harness geothermal energy: $CO_2$ and 20% NaCl brine. $CO_2$ consistently generates larger self-convecting mass flowrates than brine in indirect power cycles with no mechanical pumping. Analysis of our simple surface plant and homogeneous reservoir permits several important conclusions:

*Reservoir pressure losses are significantly greater for brine than $CO_2$.* Darcy flow in the porous and permeable reservoir produces a pressure drop in the circulating fluid, and the degree of this pressure drop depends on the average specific inverse mobility, $M$ =

*(μL)/(ρκa)*, of the fluid in question. *M* is a measure of resistance to flow. For $CO_2$, *M* is nearly constant for all depths and temperatures, whereas brine exhibits 3-12 times higher values of *M* and, thus, 3-12 times greater pressure losses. The dynamic viscosity of brine is more sensitive to temperature than its density, reducing the brine value of *M* as temperature increases; in contrast, $CO_2$ density and viscosity are roughly equally sensitive to temperature, maintaining a constant value of *M*. As a result, $CO_2$ has a relatively lower value of *M* than brine at shallow depths.

*$CO_2$ generates a larger thermosiphon-induced mass flowrate than brine.* The thermosiphon is driven by the difference in density of the working fluid between the injection and production wells. Since the cycle occurs near the critical point of $CO_2$, $CO_2$ density is very sensitive to small changes in temperature and pressure. The result is a strong thermosiphon force at depths as shallow as 0.5 km for $CO_2$. Brine never achieves the same flowrate as $CO_2$, but approaches it as temperature and depth increase to high values.

*$CO_2$ has a higher heat extraction rate, especially at shallow depths, than brine.* At depths between 0.5 km and 1.5 km, the specific heat of $CO_2$ is much greater than that of brine, while at other depths, it is lower. Combining the high specific heat with the large mass flowrates achieved by the $CO_2$ thermosiphon relative to brine, particularly at shallow depths, a $CO_2$ system can extract heat at a faster rate than brine. For example, at a depth of 1 km and a geothermal gradient of 35 ºC $km^{-1}$, a $CO_2$ thermosiphon extracts heat 300 times faster than one with brine.

*The effective pumping power of a $CO_2$ system is an order of magnitude greater than that of a brine system.* $CO_2$ is able to use a greater fraction of the extracted heat to drive the thermosiphon. For example, at a depth of 5 km and a geothermal gradient of 35 ºC $km^{-1}$, $CO_2$ uses 8% of the harnessed heat to pump the fluid compared to < 1% for brine. This can be used to eliminate mechanical pumps and associated pumping parasitic power requirements in a $CO_2$ system.

*$CO_2$ systems are ideally suited for relatively shallow depths.* $CO_2$ has a low critical pressure (7.4 MPa), which results in large density changes with small temperature changes, even at shallow depths. Substantial thermosiphon flowrates can be developed at depths as shallow as 0.5 km for $CO_2$ systems, compared to essentially no flow for brine. In addition, at shallow depths, the $CO_2$ specific heat is large and the reservoir pressure losses are an order of magnitude smaller than those of a brine system. While $CO_2$ outperforms brine in mass flowrate, heat extraction, and generated power to a depth of approximately 5 km, our results suggest that $CO_2$ is a particularly advantageous working fluid at depths between 0.5 km and 3 km.

## 2.5 Acknowledgements

We gratefully acknowledge funding from the National Science Foundation (NSF) under grant number CHE-1230691 and from the George and Orpha Gibson endowment for the Hydrogeology and Geofluids research group in the Department of Earth Sciences at the University of Minnesota (UMN). We would also like to thank the Initiative for Renewable Energy and the Environment (IREE), a signature program of the Institute on the Environment (IonE) at the University of Minnesota for initial seed funding. Any opinions, findings, conclusions, or recommendations in this material are those of the authors and do not necessarily reflect the views of the NSF, UMN, IREE, or IonE. We also gratefully acknowledge helpful comments by three anonymous reviewers and the editor which improved this paper.

Disclaimer: Drs. Saar and Randolph have a significant financial interest, and Dr. Saar has a business interest, in Heat Mining Company LLC, a company that may commercially benefit from the results of this research. The University of Minnesota has the right to receive royalty income under the terms of a license agreement with Heat Mining Company LLC. These relationships have been reviewed and managed by the University of Minnesota in accordance with its conflict of interest policies.

## 2.6 Nomenclature

The nomenclature is shown in Table 2.3.

| | |
|---|---|
| A | Cross-sectional Area [$m^2$] |
| $c_p$ | Specific heat at constant pressure [kJ $kg^{-1}$ $^oC^{-1}$] |
| D | Well pipe inner diameter [m] |
| f | Darcy friction factor [ ] |
| g | Gravitational acceleration constant [9.81 m $s^{-2}$] |
| h | Specific Enthalpy [kJ $kg^{-1}$] |
| L | Length [m] |
| M | Specific Inverse Mobility [Pa s $kg^{-1}$] |
| V | Velocity [m $s^{-1}$] |
| $\dot{m}$ | Mass flowrate [kg $s^{-1}$] |
| P | Pressure [kPa] |
| $P_{net}$ | Electric Power Generated [$kW_e$] |
| Q | Heat Transfer Rate [$kW_{th}$] |
| s | Specific Entropy [kJ $kg^{-1}K^{-1}$] |
| T | Temperature [$^oC$] |
| z | Elevation [m] |
| ε | Pipe surface roughness [m] |
| κ | Reservoir Permeability [$m^2$] |
| μ | Dynamic Viscosity [kg $m^{-1}$ $s^{-1}$] |
| η | Efficiency [ ] |
| ρ | Density [kg $m^{-3}$] |
| φ | Reservoir Porosity [ ] |

**Table 2.3: Nomenclature**

Chapter 3

# Making Electricity

## Preface

While the thermosiphon effect was found to provide substantial mass flowrates compared to water in Chapter 2, potential investors in this technology would be more influenced by the power generation potential of CPG than its mass flowrate. To make an effective comparison, CPG needs to be compared with a traditional hydrothermal facility.

Prior to this work, there were few publications of CPG power potential. Randolph and Saar (2011b; 2011c) calculated power using a simple Carnot-based surface plant model with a fixed mass flowrate. Conversely, Janke and Kuehn (2010) simulated two types of surface plants, both a direct plant and an indirect isobutane-based Organic Rankine Cycle (ORC) plant; however, they approximated the reservoir as a 2 MPa pressure difference for all mass flowrates. Thus, there was a need to couple the TOUGH2 reservoir simulator and EES surface plant simulator to provide a more conclusive set of power production values.

Additionally, electric power had only been estimated for a few sets of parameters. For example, Janke and Kuehn (2010) had only 12 combinations of temperature, depth, turbine efficiency, and system type. Randolph and Saar (2011b) had only three cases.

Similarly, $CO_2$-EGS simulations, which can provide a lower bound for CPG power production, were often only performed at single values of temperature, depth, and permeability (Atrens et al., 2009; Atrens et al., 2010; Agarwal and Anderson, 2010; Pan et al., 2013). At the same time, it was known that the substantial variability in $CO_2$ fluid properties create fluctuations in power production and, thus, no single case of simulations would be sufficient to describe power output. For example, Randolph and Saar (2011c) found that permeability could invert the relative performance of CPG and brine. Similarly, Atrens et al. (2010) found that small well diameters significantly limited $CO_2$-EGS power production; however they hypothesized that the increase of diameter might alleviate this problem. Thus, a comprehensive parameter space assessment of CPG and brine hydrothermal power generation was needed for variations in well diameter and reservoir permeability, temperature, and depth.

In this paper, the net geothermal power production is simulated for both $CO_2$ and brine using a coupled reservoir-surface plant model. Six types of surface plants are modeled: two direct geologic-$CO_2$ plants using either the thermosiphon-established mass flowrate or supplemental surface pumping, two indirect geologic-$CO_2$ plants using either R245fa or $CO_2$ as the indirect fluid, and two indirect geologic-brine plants with either R245fa or $CO_2$ as the indirect fluid. The power production is simulated for the ranges of well diameter, depth, temperature gradient, and permeability that are expected to be encountered in CPG (Table 3.1). Lastly, the detailed modeling of the surface plant is provided in the supplemental material, such as parasitic load calculations for the cooling and condensing towers, and high-side temperature and pressure optimization for the R245fa and $CO_2$ indirect cycles.

## Citation

Adams, B.M., Kuehn, T.H., Bielicki, J.M., Randolph, J.B., & Saar, M.O. (2015). A comparison of electric power output of $CO_2$ Plume Geothermal (CPG) and brine geothermal systems for varying reservoir conditions. *Applied Energy*, 140, 365-377. http://dx.doi.org/10.1016/j.apenergy.2014.11.043

# A Comparison of Electric Power Output of $CO_2$ Plume Geothermal (CPG) and Brine Geothermal Systems for Varying Reservoir Conditions

**Benjamin M. Adams[a], Thomas H. Kuehn[a]*, Jeffrey M. Bielicki[b,c], Jimmy B. Randolph[d], Martin O. Saar[d,e]**

kuehn001@umn.edu

[a]Department of Mechanical Engineering, University of Minnesota, 111 Church St SE, Minneapolis, MN 55455, U.S.A.

[b]Department of Civil, Environmental, and Geodetic Engineering, The Ohio State University, 2070 Neil Avenue, Columbus, OH 43210, U.S.A.

[c]John Glenn School of Public Affairs, The Ohio State University, 1810 College Road, Columbus, OH 43210, U.S.A.

[d]Department of Earth Sciences, University of Minnesota, 310 Pillsbury Drive SE, Minneapolis, MN 55455, U.S.A.

[e]Department of Earth Sciences, ETH-Zürich, Sonneggstrasse 5, 8092 Zürich, Switzerland

**Keywords**

Carbon Dioxide; Geothermal Energy; Carbon Dioxide Utilization; Thermosiphon; Renewable Energy; Carbon Dioxide Plume, Organic Rankine Cycle, Working Fluid

**Highlights**

- $CO_2$ has less pressure losses in a sedimentary geothermal reservoir than brine.
- $CO_2$ produces more power at shallower depths and lower permeabilities than brine.
- $CO_2$ is a better working fluid in secondary Rankine cycles than R245fa.
- Increasing the well diameters dramatically increases geothermal power production.

## Paper Summary

In contrast to conventional hydrothermal systems or enhanced geothermal systems, $CO_2$ Plume Geothermal (CPG) systems generate electricity by using $CO_2$ that has been

geothermally heated due to sequestration in a sedimentary basin. Four CPG and two brine-based geothermal systems are modeled to estimate their power production for sedimentary basin reservoir depths between 1 and 5 km, geothermal temperature gradients from 20 to 50 °C $km^{-1}$, reservoir permeabilities from $1x10^{-15}$ to $1x10^{-12}$ $m^2$ and well casing inner diameters from 0.14 m to 0.41 m. Results show that CPG direct-type systems produce more electricity than brine-based geothermal systems at depths between 2 and 3 km, and at permeabilities between $10^{-14}$ and $10^{-13}$ $m^2$, often by a factor of two. This better performance of CPG is due to the low kinematic viscosity of $CO_2$, relative to brine at those depths, and the strong thermosiphon effect generated by $CO_2$. When $CO_2$ is used instead of R245fa as the secondary working fluid in an organic Rankine cycle (ORC), the power production of both the CPG and the brine-reservoir system increases substantially; for example, by 22% and 20% for subsurface brine and $CO_2$ systems, respectively, with a 35 °C $km^{-1}$ thermal gradient, 0.27 m production and 0.41 m injection well diameters, and 5 $x10^{-14}$ $m^2$ reservoir permeability.

## 3.1 Introduction

In the United States, the Earth's crust contains an estimated 200,000 exajoules of extractable thermal energy—approximately 2000 times the current U.S. annual primary energy consumption—of which an estimated 100 GWe of geothermal energy could be produced within the next 50 years (MIT, 2006). Currently, the United States has an installed geothermal power production capacity of 3.4 GWe, mostly in California and Nevada, which utilize high geothermal temperature gradients and shallow fracture networks within the subsurface (NREL, 2014). As a consequence, technologies must be developed to more efficiently utilize undeveloped geothermal resources, such as high-temperature but lower-permeability reservoirs, or high-permeability but cooler reservoirs. Enhanced Geothermal Systems (EGS) can be deployed in high-temperature/low-permeability resources to increase the power production of a system by fracturing deep (typically about 5 km) crystalline basement rock to increase its permeability (Beckers et al., 2014), but EGS is controversial (e.g., Majer, et al., 2007). This paper describes an approach which does not require fracturing because it utilizes relatively shallow (1 to 5

km), low-temperature, naturally high-permeability sedimentary or stratigraphic reservoirs that are overlain by a low-permeability caprock. We calculate the electric power that could be produced from these geologic layers by using $CO_2$ as the subsurface heat extraction fluid (Figure 3.1) and compare the results with traditional brine-based electric power production from such reservoirs.

$CO_2$ was first proposed as a geothermal working fluid in EGS only (Brown, 2000; Pruess, 2006). $CO_2$ has two primary advantages over brine: 1) it has a low kinematic viscosity, allowing for effective heat advection; and 2) the density of $CO_2$ varies much more with temperature than that of brine which generates a stronger thermosiphon through the injection and production wells, that can thus reduce or eliminate the need for pumps circulating the subsurface fluid through the reservoir (Atrens, et al., 2009, 2010; Adams et al., 2014). Additionally, employing $CO_2$ as the heat extraction fluid can result in diminished fluid-mineral reactions, restricted to a relatively small region that will migrate as the $CO_2$ plume grows (Luhmann et al., 2014; Tutolo et al., in press).

$CO_2$ Plume Geothermal (CPG) differs from using $CO_2$ in EGS (Brown, 2000; Pruess, 2006) because CPG extracts heat from naturally permeable, sedimentary or stratigraphic basins (Randolph and Saar, 2010; 2011a; Saar et al., 2012). These sedimentary basins have larger contacting surfaces which make them favorable for heat exchange using $CO_2$ (Zhang, et al., 2014). These geologic formations are common throughout the United States and the world (IPCC, 2005); for example, they exist below approximately half of North America (Runkel et al., 2007; Coleman and Cahan, 2012) where economically favorable sequestration sites have been identified (Eccles and Pratson, 2014). Such sedimentary basins have been used for $CO_2$ disposal in some parts of the world, including one project that began in the mid-1990s (Procesi et al., 2013) and are the target of current $CO_2$ capture and sequestration (CCS) efforts (Global CCS Institute, 2013) to reduce global climate change (IPCC, 2005). Therefore, coupling CPG with an existing $CO_2$ sequestration project—thus creating a $CO_2$ capture utilization and sequestration (CCUS) process—can reduce the costs of sequestration by using $CO_2$ as a resource to generate

electricity (Randolph and Saar, 2011b; Carroll and Stillman, 2014) and distributes the cost of subsurface exploration over multiple activities (Quattrocchi et al., 2013).

To date, research into electric power production, using $CO_2$ as the subsurface working fluid, has primarily focused on EGS reservoirs at a limited set of conditions (Atrens et al., 2009, 2010, 2011; Beckers et al., 2014). Atrens (2010) calculated exergy production (largest theoretical surface plant electric power production) for both subsurface $CO_2$ and water for a single set of parameters: a 225 °C, 5 km, fixed-permeability reservoir modeled with the Darcy equation, and 0.23 m injection and production well diameters. Beckers et al. (2014) calculated electric power production and Levelized Cost of Electricity (LCOE) for EGS with fixed mass flowrates by varying multiple parameters including depth, geothermal temperature gradient, well diameter, and surface plant design.

To date, CPG research has focused on reservoir and wellbore fluid dynamics. Randolph and Saar (2011a; 2011c) presented initial estimates of electrical power production using a simple Carnot-based power plant and a fixed mass flowrate, depth, and temperature. Buscheck et al. (2012) found that active reservoir management—the manipulation of reservoir characteristics such as plume size or pressure—is necessary to maintain power production after initial CPG deployment. Buscheck et al. (2014) extended the reservoir modeling to use both $CO_2$ and brine as geothermal working fluids, but focused on the engineered pressure gradients between concentric rings of $CO_2$ and brine wells, and used a simple model to predict $CO_2$ power production. Janke and Kuehn (2011) primarily modeled the surface plant and power production of a CPG system, using a fixed pressure drop reservoir. Despite the fixed mass flowrate of 70 kg $s^{-1}$, for a 2.5 km, 100 °C geothermal reservoir, they showed that directly expanding the $CO_2$ through a turbine (direct system) produces 2x - 8x more power than a secondary Rankine cycle (indirect system). Direct $CO_2$-based geothermal power cycles can have higher cycle efficiencies, but they are not yet commercially available. Some effort is being made to adapt existing

waste heat recovery turbomachinery to generate electricity from produced $CO_2$ at a CCUS demonstration site at Cranfield, MS, USA (Freifeld, 2013).

One advantage of using $CO_2$ as a geologic working fluid is the substantial mass flowrates obtained from the density-driven thermosiphon (Adams et al., 2014). These authors combined a reservoir model with wellbore and surface piping models to estimate the strength of this thermosiphon for several depths and temperature gradients and showed substantial mass flowrates at depths as shallow as 1 km. Similarly, Pan et al. (2015) used a multi-phase, multi-fluid wellbore simulator, T2Well, coupled with a reservoir model to show the strength of the thermosiphon for a 3 km, 152 °C pure-$CO_2$ sedimentary reservoir with a $10^{-13}$ $m^2$ permeability, using industry-standard 4 inch (0.1 m) and 7 inch (0.18 m) piping. While Pan et al. (2015) fix mass flowrate, they show, by way of a pressure differential between injection and production wellheads, that a thermosiphon will be established.

In this paper, we expand upon our previous work by coupling combined fluid-dynamic-thermodynamic models of sedimentary basin reservoirs with models of injection/production wells and the surface plant, for varying reservoir conditions, piping, and surface plant configurations, in order to compare the performance of CPG and brine geothermal systems. Compared to previous studies, we investigate a much-expanded range of parameters (e.g. well diameters from 0.14 to 0.41 m) so as not to exclude any potentially profitable, and technologically possible, CPG configurations. For example, considering significantly larger, yet reasonable, well diameters is particularly important, given that pressure losses in the well are inversely proportional to the fifth power of the well diameter, thereby considerably affecting the power production of CPG and other geothermal systems. Additionally, unlike previous work, we do not parameterize mass flowrate, but instead operate at mass flowrates which provide maximum power generation.

In total, we model six sedimentary basin geothermal power plant scenarios (Table 3.1): 1) a direct $CO_2$ plant relying on the thermosiphon effect (Adams et al., 2014) to provide the $CO_2$ circulation through the geothermal reservoir and the surface plant; 2) a direct $CO_2$ plant with supplemental pumping; two indirect $CO_2$ plants using either 3) R245fa (1,1,1,3,3-Pentafluoropropane) or 4) $CO_2$ (R744) as the secondary working fluid; and two indirect brine plants using either 5) R245fa or 6) $CO_2$ as the secondary working fluid. For each scenario, the power production is calculated for reservoir depths of 1 to 5 km, geothermal temperature gradients of 20, 35, and 50 °C $km^{-1}$, reservoir permeabilities from $10^{-15}$ to $10^{-12}$ $m^2$, and well inner diameters from 0.14 to 0.41 m.

**Table 3.1: Model parameters for six combinations of geothermal reservoir and power plant scenarios as described in the main text.**

| | |
|---|---|
| Power System | Direct $CO_2$ – Thermosiphon Only<br>Direct $CO_2$ – Supplemental Pumping<br>Indirect $CO_2$ – R245fa or $CO_2$ Secondary<br>Indirect Brine – R245fa or $CO_2$ Secondary |
| Well Diameter | 0.14 m, 0.27 m, 0.33 m, and/or 0.41 m |
| *Reservoir Conditions* | |
| Depth | 1.0 km, 1.5 km, 2.5 km, 3.5 km, or 5.0 km |
| Thermal Gradient | 20 °C $km^{-1}$, 35 °C $km^{-1}$, or 50 °C $km^{-1}$ |
| Permeability | $1x10^{-12}$ $m^2$ to $1x10^{-15}$ $m^2$ |

## 3.2 Methods

Each inverted 5-spot system configuration involves four major components: a reservoir, an injection well (IW), four production wells (PW), and a surface power plant, as shown in Figure 3.1. The $CO_2$-based systems are initially coupled with a $CO_2$ emitter to inject and fill the reservoir, but no such $CO_2$ sequestration and brine displacement are explicitly simulated. Instead, the pore space of CPG reservoirs is assumed to be completely filled with $CO_2$. Total system performance is modeled by using two software packages: 1) TOUGH2 (Pruess, 2004), with the Equation of State (ECO2N) module (Pruess, 2004, 2005), is used for subsurface fluid- and thermodynamic modeling of geothermal heat and fluid extraction as well as fluid re-injection into the reservoir; and 2) Engineering

Equation Solver (EES) is used to simulate the surface plant power production and wellbore fluid flow. EES is a simultaneous equation solver with built-in thermodynamic property data, including data for $CO_2$ from Span and Wagner (1996). Model parameters are given in Table 3.2.

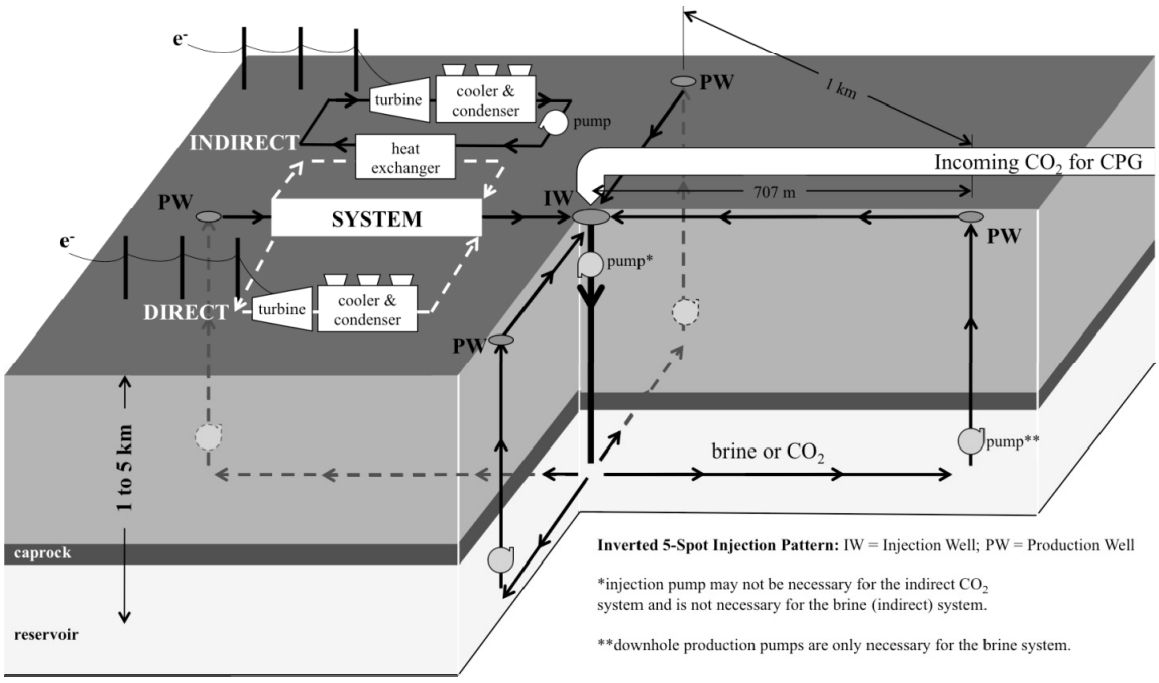


**Figure 3.1: Simplified system schematic showing geothermal reservoir, surface power plant system, and inverted 5-spot well pattern.** Modeling injection-production well pairs implies that a power plant system exists between each production well and injection well. Detailed system configurations are shown in later figures.

### 3.2.1 Base-case Parameters

It is useful to select "base case" conditions to which various alternative options can be compared. Base case parameters include: a horizontal, homogeneous, isotropic reservoir with a thickness of 305 m at an average depth of 2.5 km, a porosity of 10%, and a permeability of $5 \times 10^{-14}$ $m^2$ which is overlain by an impermeable caprock, a geothermal temperature gradient of 35 °C $km^{-1}$ with an ambient air temperature of 15 °C, an injection well inner diameter of 0.41 m, and a production well inner diameter of 0.27 m. The geothermal temperature gradient is approximately the average value for the continental

crust of the western United States of 34 °C $km^{-1}$ (Nathenson and Guffanti, 1988; Pollack et al., 1993). The permeability of 5 $x10^{-14}$ $m^2$ is approximately the average horizontal permeability of sedimentary reservoirs: the Mt. Simon formation, into which 0.3 Mt $CO_2$ $yr^{-1}$ is currently being sequestered near Decatur, Illinois (Global CCS Institute, 2012), has an average horizontal permeability of 2.6 $x10^{-14}$ $m^2$ (Frailey et al., 2011); similarly, a larger study of the Illinois Basin reported typical average horizontal permeabilities between 3 $x10^{-14}$ and 10 $x10^{-14}$ $m^2$ (Finley, 2005; Randolph & Saar, 2010). The ambient air temperature assumed is 15°C and is thus greater than most averages within the United States and represents the approximate average annual air temperature in Dallas, Texas. Because power production increases as ambient air temperature (thermodynamic heat sink) decreases, the power production found, when using a high average annual ambient air temperature of 15°C, is a conservative, i.e., low, estimate of the expected average yearly power production (see Section 3.8.4.3).

### 3.2.2 Conceptual and Numerical Geologic Model

The fluid injection and production pattern used in the present simulations is the standard inverted 5-spot configuration used in previous publications (e.g., Sanyal and Butler, 2005; Pruess, 2006; Randolph and Saar, 2011a) with four symmetrically placed production wells, located at the corners of a 1 km by 1 km square (in map-view), and one injection well in the center (Figure 3.1). This configuration allows direct comparison with previous publications although other well configurations, including horizontal production wells (Garapati et al., 2015) will likely further improve system performance. The symmetrical layout of the inverted 5-spot well configuration and reservoir requires only one-eighth of the reservoir be modeled.

To facilitate direct comparison between brine and $CO_2$ geothermal systems, the pores are assumed to be completely filled with either pure $CO_2$ or 20 wt% NaCl brine. As a consequence, time-dependent behavior such as brine displacement by $CO_2$, heat depletion in the geothermal reservoir, or $CO_2$ dissolution into brine is not considered (Kong and Saar, 2013; Garapati et al., 2015; Meng and Jiang, 2014), and localized clogging due to

salt precipitation has been remedied (Borgia, et al., 2012). Reservoir parameters are described in Table 3.2. Reservoir boundary conditions include no fluid flow through over- and underlying (assumed) zero-permeability cap- and bedrocks and no flow due to lateral symmetry to adjacent inverted 5-spot well patterns as described in Oldenburg et al. (2004), Pruess (2006), and Randolph and Saar (2011a). Heat transfer from over- and underlying formations is simulated with a standard semi-analytic conductive heat exchange boundary condition (Pruess et al., 1999), while no heat transfer occurs at the lateral boundaries due to the aforementioned symmetry. All reservoir rock and fluid temperatures are initially uniform and are determined by the product of depth and geothermal gradient added to the ambient mean annual near-surface air temperature.

The state of the fluid produced from the reservoir depends on several factors, including reservoir depth, temperature, permeability, fluid mass flowrate, injection pressure, and injection temperature. These factors are determined by the system as a whole; therefore, the TOUGH2 reservoir model must be solved simultaneously with the well and surface power plant models. For a given reservoir at a fixed temperature and depth, the pressure change between injection and production wells tends to vary primarily with mass flowrate; we can thus describe the TOUGH2 reservoir model performance in terms of mass flowrate for every reservoir parameter combination, and use this characterization, along with produced fluid temperatures, in the well and surface power plant models.

**Table 3.2: Model parameters (as justified in the main text)**

| | |
|---|---|
| Primary System (Reservoir) Fluids | - 100% $CO_2$<br>- 20 wt% $H_2O$-NaCl (brine) |
| Secondary (ORC) System Fluids (for indirect systems) | - $CO_2$ (R744)<br>- 1,1,1,3,3-Pentafluoropropane (R245fa) |
| Downhole Production Well Pressure | Hydrostatic |
| Direct Turbine Isentropic Efficiency | 78% |
| ORC Turbine Efficiency | 80% |
| Pump Efficiencies | 90% |
| Well Pipe Material | Bare CR13 |
| Well Pipe Roughness | 55 μm (Farshad and Rieke, 2006) |
| Condensing or Cooling Tower Approach Temperature | 7 °C (see Section 3.8.4.2) |

| | |
|---|---|
| Ambient Mean Annual Air Temperature | 15 °C |
| *Reservoir Constants* | |
| Well Configuration | Inverted 5-spot (a 1 $km^2$ footprint, see Figure 3.1) |
| Reservoir Thickness and Depth | 305 m thick, 1-5 km deep (base case: 2.5 km deep) |
| Rock Density | 2300 kg $m^{-3}$ |
| Reservoir Porosity | 0.10 |
| Reservoir Permeability | 5 $x10^{-14}$ $m^2$ (base case only) |
| Reservoir Volume | $2.7x10^8$ $m^3$ |
| Reservoir Fluid Volume | $0.3x10^8$ $m^3$ (8.2 Mt $CO_2$ @ 2.5 km) |
| Initial Reservoir Temperature Profile | Uniform |
| Lateral Reservoir Boundary Condition | No heat or fluid flow |
| Vertical Reservoir Boundary Condition | No fluid flow; heat conduction using TOUGH2 semi-analytic model (Pruess et al., 1999) |

For steady, laminar 1D flow through a porous medium, the pressure drop, $\Delta P$, can be calculated using Darcy's Law (Darcy, 1856), given by Equation 3.1. For a specified reservoir at a given depth and temperature, the average fluid density, $\rho$, and dynamic viscosity, $\mu$, are nearly constant. Likewise, the combination of reservoir properties length, $L$, and area, $A$, is constant. The combination of these four terms, referred to hereafter as the Average Specific Kinematic Viscosity, $S$, is contained in brackets in Equation 3.1. When the value of $S$ is divided by reservoir permeability, κ, it represents a constant of proportionality, $R=S/\kappa$, relating $\Delta P$ to fluid mass flowrate, $\dot{m}$.

$$\Delta P = \left[\frac{\mu L}{\rho A}\right]\frac{\dot{m}}{\kappa} = S\frac{\dot{m}}{\kappa} = R\dot{m} \qquad (3.1)$$

Thus, $R$ may be viewed as a "reservoir parameter" that combines both fluid and porous medium properties, similar to hydraulic conductivity, and describes how effectively the reservoir fluid is being transmitted for a given pressure difference, $\Delta P$. $R$ has been previously described as "average specific inverse mobility" (Adams, et al., 2014). $S$ is

used to calculate the reservoir parameters for the range of reservoir permeabilities considered here.

To calculate a given value of *S*, we determine the difference between injection and production pressure in the reservoir from TOUGH2 simulation results for six mass flowrates and eleven permeabilities, ranging from $1x10^{-15}$ $m^2$ to $1x10^{-11}$ $m^2$, at the specified depth and temperature gradient. The pressure drop, $\Delta P$, for these 66 mass flowrate and permeability combinations is multiplied by the permeability. We then perform a linear regression of the form $\Delta P \cdot \kappa = \alpha + \beta \cdot \dot{m}$, where the intercept, α, is set to zero. The resulting slope, $\beta$, is *S* for that combination of depth and temperature gradient. Calculated values of *S*, each represented by a single data point, are shown in Figure 3.2. The uncertainty in *S* is, on average, less than 1%, indicating the excellent characterization of the TOUGH2 numerical model, given in particular the standard assumed simulator uncertainty of ±6% (see Section 3.8.1).

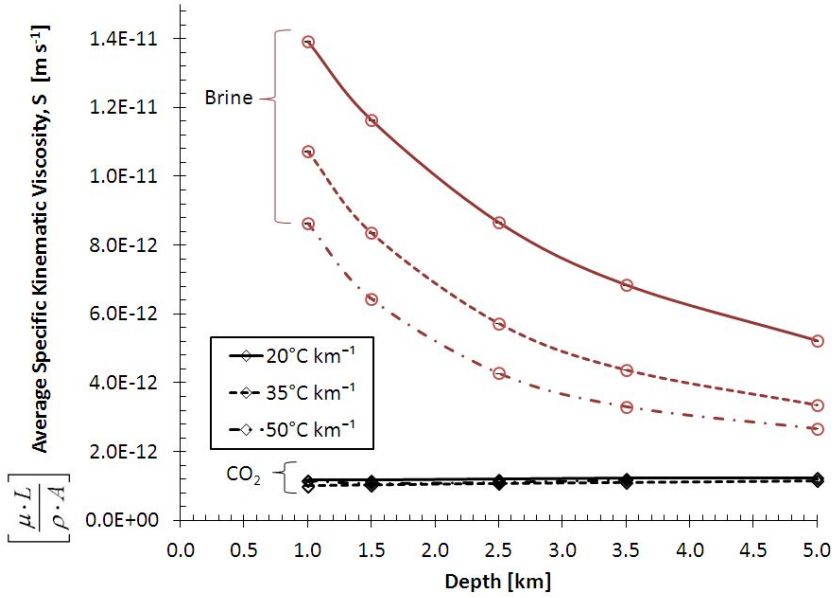


**Figure 3.2: Average Specific Kinematic Viscosity, *S*, of a Reservoir at Temperatures and Depths encountered for brine and $CO_2$ reservoir fluids.** *S* is a characterization of the TOUGH2 model, which in turn is used by the surface plant EES model to determine reservoir pressure drop, $\Delta P$. The benefit of using $CO_2$, instead of brine, is shown by the substantially

smaller value in $S$, i.e., substantially smaller pressure drop, of the $CO_2$ at all depths, but especially at shallow depths.

Figure 3.2 shows that the value of $S \approx 1.14 \times 10^{-12}$ m s$^{-1}$ for $CO_2$ is nearly constant over the investigated depth and geothermal gradient ranges, whereas $S$ for brine, $S_{brine}$, decreases with increasing depth and temperature gradient. These values for $CO_2$ are likely to decrease as heterogeneities are introduced into the reservoir model (Luo et al., 2013), and $S$ may, therefore, overestimate the pressure loss that is likely to occur. At 1 km depth and temperature gradients of 20°C km$^{-1}$ and 50°C km$^{-1}$, $S_{brine}$ is respectively 12 and 8 times greater than that of $CO_2$, which is consistent with Pruess (2006). At 5 km depth, $S_{brine}$ decreases to 5 and 2 times greater than that of $CO_2$ for 20°C km$^{-1}$ and 50°C km$^{-1}$, respectively.

For a given reservoir depth and temperature, differences in average specific kinematic viscosity, $S$, are due only to changes in kinematic viscosity, $\mu/\rho$. Kinematic viscosity describes the tendency of a fluid to resist flow due to diffusion of momentum. Consequently, high kinematic viscosities result in high reservoir pressure losses and ultimately large pumping power requirements or low thermosiphon-generated mass flowrates (Adams et al., 2014). The ratio of the kinematic viscosities of brine and $CO_2$ decreases with increasing depth and temperature gradient, indicating $CO_2$ will have comparatively lower reservoir pressure losses and pumping power requirements in shallow, cooler reservoirs.

### 3.2.3 Well and Surface Power Plant Models

Six surface power plant models and primary working fluid combinations are considered (Table 3.1): two direct $CO_2$ systems, two indirect $CO_2$ systems, and two indirect brine systems. The indirect systems use either R245fa or $CO_2$ as the secondary system working fluid. The direct $CO_2$ system is modeled in two ways. The “thermosiphon” system has no pumps because the flow is generated entirely by the density difference between injection and production wells (Adams et al., 2014). The “pumped” system uses an injection pump at the surface to augment the thermosiphon flow. Surface pumps are easily maintained

and less prone to failure compared to submersible pumps. The indirect brine system, using R245fa, is the standard for current geothermal technology and requires substantial pumping by a pump submersed in the production well.

In all models, the fluid flow in the wells and surface plant are modeled using Engineering Equation Solver (EES). Brine property values are determined from the relationships provided by Driesner (2007) and the IAPS-84 Steam Tables (Haar et al., 1984). The net power, $P_{net}$, is the power supplied by the plant, defined in Equation 3.2 as the gross turbine power plus the (negative) parasitic powers of the pumps and heat rejection equipment.

$$P_{net} = P_{turbine} + P_{pump,primary} + P_{pump,ORC} + P_{fan,cooler} + P_{fan,condenser} \quad (3.2)$$

#### 3.2.3.1 $CO_2$ Direct (Thermosiphon and Pumped)

Fluid flow through the wells and the surface power plant is illustrated in Figure 3.3. Sub-cooled liquid $CO_2$ is injected at the surface at State 1, where it travels adiabatically and nearly isentropically down the injection well to State 2, transitioning to a supercritical fluid as pressures and temperatures increase above the critical point ($T_c$ = 304 K, $P_c$ = 7.4 MPa). The $CO_2$ then flows through the reservoir, heating to the reservoir temperature, reducing in pressure until it reaches the production well at State 3, where it is at the reservoir hydrostatic pressure. The fluid rises adiabatically (Randolph et al., 2012) through the production well to State 4. Once at the surface, it is expanded through a two-phase turbine, with an assumed isentropic efficiency of 78%, based on estimated performance data from a turbine manufacturer. The fluid is then cooled and condensed isobarically through the cooling and condensing towers at the surface to State 6, where its "approach temperature" is 7°C; that is, the fluid is cooled to 7°C above ambient temperature. Section 3.8.4.2 of the Supplemental Information discusses how this approach temperature is chosen. States 7 and 1 are determined differently for $CO_2$ Direct Pumped and $CO_2$ Direct Thermosiphon type systems.

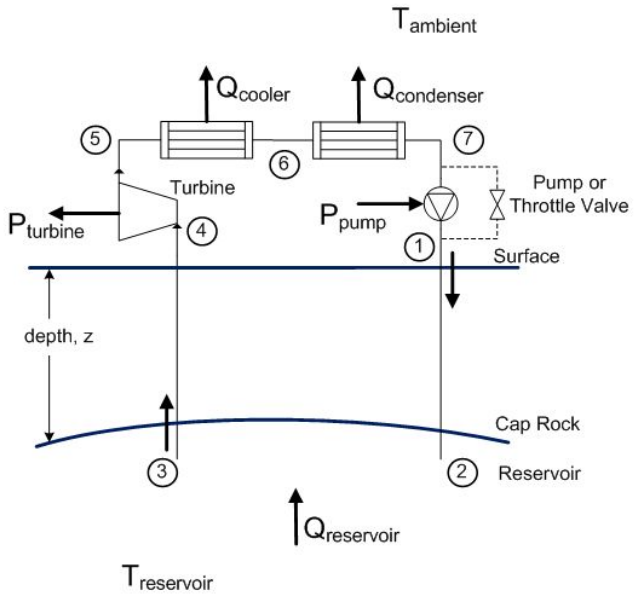


**Figure 3.3: Direct $CO_2$ System.** The direct system using $CO_2$ as the subsurface heat extraction fluid passes the $CO_2$ directly through a turbine (expander) in order to generate electric power.

In a $CO_2$ Direct Pumped system, a pump may be used to supplement the thermosiphon, and the condensation pressure (State 7) is set to 50 kPa above the saturation pressure of $CO_2$ at 22°C. In this direct configuration, either a pump or throttle valve is used between States 7 and 1 (Figure 3.3) to achieve the greatest net power. The net power tends to increase with some pumping, but there are some scenarios in which a decrease in pressure between States 7 and 1 reduces the overall system mass flowrate. This reduction in mass flowrate decreases the condenser parasitic power losses more than the decrease in turbine power and thus increases net power output. As a consequence, throttling by a valve is used in approximately 10% of the Direct $CO_2$ Pumped scenarios, typically where the turbine is operated near the critical point of $CO_2$. In this fraction of scenarios, the power outputs of the Direct $CO_2$ Pumped and Thermosiphon systems are the same.

In a $CO_2$ Direct Thermosiphon system, the condensation pressure (State 7) is set to achieve a pressure at State 2, which is equivalent to the sum of the hydrostatic reservoir pressure and the reservoir pressure change; however, the pressure at State 7 may never be less than 50 kPa above the saturation pressure of $CO_2$ at 22°C. In some $CO_2$ Direct

Thermosiphon systems, a throttle valve is added between State 7 (after the condenser) and State 1 (injection well) to decrease the system mass flowrate. Such throttling decreases the pressure losses in the production well and the reservoir, decreasing the fluid density in the turbine, and thus increasing the power generated by the turbine.

The fluid state in the injection and production wells is calculated numerically with 100 m long axial elements. This element size is chosen to balance computational time with the precision of the results; results for 100 m long elements are within 1% of results for a finely discretized model using 1 m segments. Across each vertical well element, the first law of thermodynamics, patched Bernoulli, and the conservation of mass equations are used to determine the state of each successive starting element, as shown in Equations 3.3-3.6, where subscripts *i* and *i+1* denote the beginning and end of each element, respectively. All nomenclature is described in Table 3.3. The well segments are considered to be adiabatic (Randolph et al., 2012), but not isenthalpic as assumed in earlier studies (Pruess and Azaraoul, 2006; Pruess, 2006).

$$h_i + \frac{V_i^2}{2} + g\,z_i = h_{i+1} + \frac{V_{i+1}^2}{2} + g\,z_{i+1} \tag{3.3}$$

$$P_i + \frac{\rho_i V_i^2}{2} + \rho_i\,g\,z_i = P_{i+1} + \frac{\rho_i\,V_{i+1}^2}{2} + \rho_i\,g\,z_{i+1} - \Delta P_{loss} \tag{3.4}$$

$$\Delta P_{loss} = f\,\frac{L_{pipe}}{D}\,\frac{\rho V^2}{2} = f\,\frac{L_{pipe}}{D^5}\,\frac{8\dot{m}^2}{\rho\pi^2} \tag{3.5}$$

$$\dot{m} = \rho_i A V_i = \rho_{i+1} A V_{i+1} \tag{3.6}$$

The friction factor, *f*, is determined using the Moody Chart, based on the pipe inner diameter, surface roughness, and Reynolds number (Moody, 1944). A pipe surface roughness of 55 μm is used to approximate bare CR13 piping, a standard oil and gas martensitic stainless steel piping used in corrosive environments, as suggested by Farshad and Rieke (2007). This value overestimates pressure losses when compared with the typical 45μm value suggested by Moody (1944) for schedule 40 pipe.

Additionally, pressure losses ($\Delta P_{loss}$ in Equation 3.5) are proportional to the square of the mass flowrate, $\dot{m}$, and inversely proportional to the fifth power of the pipe diameter, $D$. Hence, power production is sensitive to small changes in $D$. Furthermore, for the same mass flowrate, pressure losses decrease as fluid density increases; therefore, pressure losses in the injection well, where fluids are relatively cool and thus dense, are usually a small fraction of those in the production well, where fluids are relatively hot and thus less dense.

$$Q - P = \dot{m}\left(h_{out} - h_{in}\right) \tag{3.7}$$

The power and heat values are found from the enthalpy difference of the fluid, shown in Equation 3.7. Specifically, the power output of the turbine is the product of the difference of inlet and exit enthalpies, found using the isentropic turbine efficiency and the mass flowrate. Similarly, the pump power is found using the isentropic pump efficiency. The heat extraction rates for the reservoir, cooling, and condensing towers are the products of the enthalpy difference, between inlet and outlet, and the mass flowrate (Equation 3.7). The parasitic power requirements of the cooling and condensing towers are the product of the heat extraction rate and the parasitic loss fraction, λ, which is described in Section 3.8.2. The net power varies as a function of mass flowrate, as shown in Figure 3.4, for the base-case Direct $CO_2$ Thermosiphon (un-pumped) system. As mass flowrate increases, the power gains provided by increased turbine throughput are offset by the pressure losses incurred in the piping and reservoir, yielding a point of optimum power. Thus, the mass flowrate through the system is chosen to maximize the net power produced and is further described in Section 3.8.4.1.

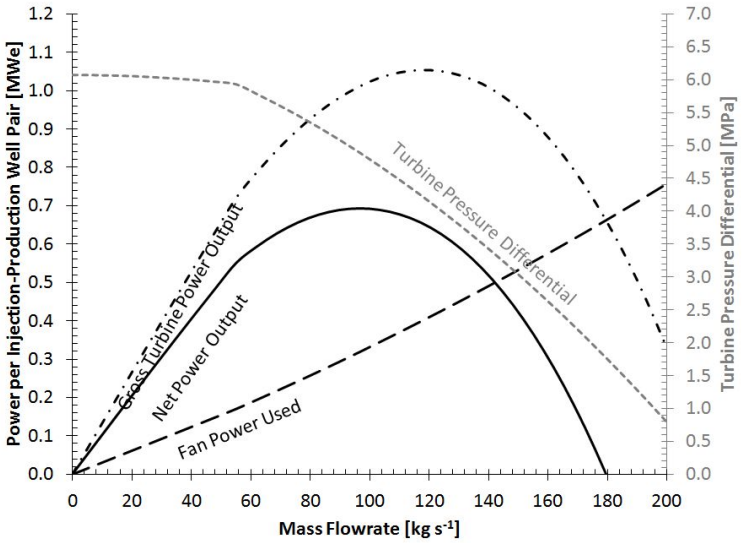


**Figure 3.4: Power Output of a Direct $CO_2$ Thermosiphon (un-pumped) System for One Injection-Production Well Pair [Base-case] of which 4 such pairs constitute one 5-spot system.** Net power output is the gross turbine power output less the parasitic fan power of the cooling tower (Equation 3.2). At low mass flowrates, turbine power output increases with mass flowrate; however, at high mass flowrates, well and reservoir pressure losses decrease the turbine pressure difference, reducing turbine power output, and causing the net power to peak (here ~100 kg $s^{-1}$).

### 3.2.3.2 Indirect $CO_2$ and Brine

In an indirect system, the primary, i.e., subsurface geothermal, working fluid passes through a heat exchanger, driving a secondary Rankine cycle, as shown in Figure 3.5. Indirect systems benefit from using "off-the-shelf" components and have fewer moving parts in contact with the geothermal fluid, but they have smaller overall system thermal efficiency. The Rankine cycle consists of six major components: a preheater (States 13 to 14), a boiler (States 14 to 9), a turbine (States 9 to 10), a de-superheater (States 10 to 11), a condenser (States 11 to 12), and a pump (States 12 to 13). Advanced Rankine technology (e.g., multi-stage turbines and regenerators) are beyond the scope of this paper, but they may increase cycle efficiency with some working fluids (Wang et al., 2012; Yin et al., 2013). Superheating is applied when it is necessary to set the turbine outlet or the pump inlet at a saturated state, depending on the saturation curve characteristics of the secondary working fluid. The $CO_2$ and brine subsurface working fluid systems are modeled almost identically, except the brine system requires a

downhole pump (States 4 to 5). The wells (States 1 to 4 and 5 to 6) are modeled the same way as in the direct $CO_2$ system, using their respective brine or $CO_2$ fluid property values. Turbomachinery efficiencies are listed in Table 3.2 and are typical of ORC simulations (Suaret and Gu, 2014).

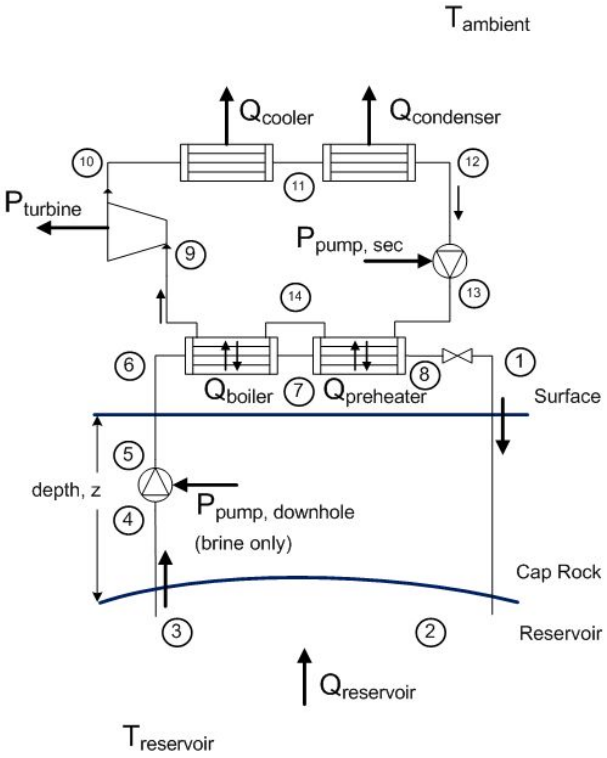


**Figure 3.5: Indirect brine or $CO_2$ Geothermal System.** The indirect system uses a secondary Rankine cycle that extracts energy from the heat extraction fluid using heat exchangers. When brine is the primary, i.e., subsurface geothermal, heat extraction fluid, a downhole pump is necessary to circulate the brine. In contrast, when using $CO_2$ as the geothermal working fluid, no pumping is necessary due to the development of a strong thermosiphon (Adams et al., 2014), and, instead, net power output may even increase in certain cases by throttling the fluid flow (States 8 to 1) as discussed in the main text.

At the surface, in the primary working fluid loop, the fluid passes isobarically through a boiler (R245fa only) and a preheater, arriving at State 8. Then the fluid flows isenthalpically through a throttling valve, used to reduce the pressure and control the mass flowrate ($CO_2$ only), where it arrives at State 1 and is reinjected through a well into the reservoir. No geothermal pumps are used in the indirect geologic-$CO_2$ system because the energy they require is greater than the increase in power they produce. Unlike the direct system, the indirect system does not drive a pressure reduction device (e.g.,

turbine) at the surface; therefore, the indirect geologic-$CO_2$ system operates at higher primary-fluid mass flowrates than its direct counterpart, and is driven by the additional pressure potential otherwise used to operate the turbine.

The secondary cycle is a trans-critical ($CO_2$) or sub-critical (R245fa) Rankine cycle. Low density fluid leaves the boiler at State 9 and is expanded through the turbine to either a superheated vapor (R245fa) or a saturated vapor ($CO_2$) at State 10. The fluid is then cooled isobarically to saturation at State 11 (R245fa only), and then condensed isobarically to State 12 at a saturation pressure that is 7°C above ambient temperature (7°C approach temperature). The high density liquid is then pumped to a high pressure sub-cooled liquid at State 13. When using R245fa, it is heated to boiling at State 14, and then heated to a saturated vapor at State 9. In the case of the trans-critical $CO_2$ Rankine cycle, the supercritical fluid is heated from State 13 to State 9, increasing in temperature throughout with no discernible phase change.

When R245fa is used as the secondary working fluid, the temperature of the primary fluid within the heat exchanger is set to be at least 7°C hotter than the R245fa secondary fluid at any location; this value was obtained as a compromise between cost and performance in unreported optimization simulations. This restriction specifies that the fluid temperature at State 7 must be at least 7°C above the boiling temperature of the R245fa, and the temperature at State 8 must be at least 7°C above the condensing temperature of the R245fa. These 7°C specifications can result in a "pinch point" problem, where the fluid outlet temperature at State 8 is much higher than 7°C above ambient and the injected fluid contains useful thermal energy. Injecting unused energy results in decreased cycle efficiency, decreased density in the injection well, and diminished mass flowrate produced by the thermosiphon effect. Conversely, injecting unused energy into the reservoir does extend the reservoir lifespan. Low-temperature solar energy can be used to assist with boiling the secondary working fluid, to decrease injection temperature and mitigate the pinch-point problem (Ghasemi et al., 2014), but, we did not use this method here.

When $CO_2$ is used as the secondary working fluid, the heat exchanger pinch point problem is alleviated. The $CO_2$ on the high-pressure side of the Rankine Cycle is a supercritical fluid and does not boil; it has a nearly constant temperature gradient, which matches the decreasing temperature profile of the primary working fluid passing through the counter-flow heat exchanger. For these $CO_2$ simulations, the boiler is removed so that all heat transfer occurs within the preheater.

When using R245fa or $CO_2$ as the secondary fluid, the plant operator selects either the secondary boiling temperature (R245fa) or the secondary high-side pressure ($CO_2$), which yields the largest net power. We determine the operating points for these indirect systems (see Section 3.8.3).

In contrast to the indirect $CO_2$-geology-based systems that increase the mass flowrate, and thus power, most effectively by cooling the injected fluid, the indirect brine-geology-based systems produce increased net power when pumped (Adams et al., 2013). Therefore, a downhole lineshaft pump is placed 500 m down the production well (States 4 to 5 in Figure 3.5) in all subsurface brine scenarios. The pumping power is allowed to vary in order to attain the maximum net power output of the system. A maximum pumping pressure difference of 10 MPa is set, based on the limit of currently available geothermal downhole lineshaft Vertical Industrial Turbine pumps available from Goulds (2013), which is approximately 3 times larger than what was allowed by Sanyal and Butler (2005).

When using a brine system, flashing can occur at the surface if piping pressure losses decrease the brine pressure below its saturation pressure; therefore, the minimum pressure in the system is maintained above the condensing pressure for the brine. To allow this flexibility, the downhole well pressure is always above or below the hydrostatic pressure of the reservoir. This over-pressurization is generally small: 1400 kPa on average and a standard deviation of 2020 kPa above hydrostatic pressure for the

parameter space investigated. Minimum and maximum under/over-pressurizations are -2440 kPa and 10,440 kPa, respectively. Therefore, the calculated mass flowrate values for the brine are a high limit and will decrease based on the actual reservoir pressure.

The injection temperature of the brine is limited by the saturation temperature of dissolved amorphous silica. In the reservoir, the brine is saturated with dissolved quartz. When the brine is produced to the surface and cools more than 122°C (89°C) for 0 wt% NaCl brine (20 wt% NaCl brine), the quartz precipitates from the solution as amorphous silica (DiPippo, 1985). This causes scaling within the piping and turbomachinery and is avoided by maintaining the brine above the saturation temperature of amorphous silica.

## 3.3 Parameter Space Results

Six surface plant models, six reservoir permeabilities, five depths, three geothermal temperature gradients, and four well diameters have been investigated (Table 3.1), resulting in 5670 individual electric power production values. For comparison, a subset of these values is shown in Figure 3.6 providing 225 values each for the direct $CO_2$ (with pumping) system and the indirect brine system (which is always pumped) with R245fa as the secondary working fluid. The indirect brine/R245fa case most closely represents the current state of technology for geothermal power production as none of the other systems are commercially available. Tables for all six surface plants can be found in Section 3.8.5. All power production and mass flowrate data are available in Section 3.8.6.

a)

**Direct $CO_2$ - Pumped**

Power Output per Production-Injection Pair [MWe]

| Temp Gradient [°C km$^{-1}$] | Depth [km] | 0.27m Inj & Prod Diameter | | | | | 0.33m Inj & Prod Diameter | | | | | 0.41m Inj & Prod Diameter | | | | |
|---|---|---|---|---|---|---|---|---|---|---|---|---|---|---|---|---|
| | | 1x10$^{-15}$ m$^2$ | 1x10$^{-14}$ m$^2$ | 5x10$^{-14}$ m$^2$ | 1x10$^{-13}$ m$^2$ | 1x10$^{-12}$ m$^2$ | 1x10$^{-15}$ m$^2$ | 1x10$^{-14}$ m$^2$ | 5x10$^{-14}$ m$^2$ | 1x10$^{-13}$ m$^2$ | 1x10$^{-12}$ m$^2$ | 1x10$^{-15}$ m$^2$ | 1x10$^{-14}$ m$^2$ | 5x10$^{-14}$ m$^2$ | 1x10$^{-13}$ m$^2$ | 1x10$^{-12}$ m$^2$ |
| 20 | 1.0 | 0.0 | 0.0 | 0.0 | 0.0 | 0.0 | 0.0 | 0.0 | 0.0 | 0.0 | 0.0 | 0.0 | 0.0 | 0.0 | 0.0 | 0.0 |
| | 1.5 | 0.0 | 0.0 | 0.0 | 0.0 | 0.0 | 0.0 | 0.0 | 0.0 | 0.0 | 0.0 | 0.0 | 0.0 | 0.0 | 0.0 | 0.0 |
| | 2.5 | 0.0 | 0.0 | 0.0 | 0.0 | 0.0 | 0.0 | 0.0 | 0.0 | 0.1 | 0.1 | 0.0 | 0.0 | 0.0 | 0.1 | 0.1 |
| | 3.5 | 0.0 | 0.0 | 0.1 | 0.1 | 0.1 | 0.0 | 0.0 | 0.1 | 0.2 | 0.2 | 0.0 | 0.0 | 0.2 | 0.3 | 0.4 |
| | 5.0 | 0.0 | 0.1 | 0.3 | 0.3 | 0.4 | 0.0 | 0.2 | 0.4 | 0.5 | 0.6 | 0.0 | 0.2 | 0.6 | 0.8 | 1.1 |
| 35 | 1.0 | 0.0 | 0.0 | 0.0 | 0.0 | 0.0 | 0.0 | 0.0 | 0.0 | 0.0 | 0.0 | 0.0 | 0.0 | 0.0 | 0.0 | 0.0 |
| | 1.5 | 0.0 | 0.0 | 0.1 | 0.1 | 0.1 | 0.0 | 0.0 | 0.1 | 0.2 | 0.2 | 0.0 | 0.0 | 0.2 | 0.3 | 0.3 |
| | 2.5 | 0.0 | 0.2 | 0.5 | 0.6 | 0.6 | 0.0 | 0.2 | 0.7 | 0.9 | 1.1 | 0.0 | 0.3 | 0.9 | 1.3 | 1.8 |
| | 3.5 | 0.1 | 0.6 | 1.0 | 1.1 | 1.2 | 0.1 | 0.7 | 1.6 | 1.8 | 2.1 | 0.1 | 0.7 | 2.3 | 2.9 | 3.6 |
| | 5.0 | 0.2 | 1.5 | 2.3 | 2.5 | 2.6 | 0.2 | 1.9 | 3.7 | 4.0 | 4.4 | 0.2 | 2.2 | 5.6 | 6.5 | 7.7 |
| 50 | 1.0 | 0.0 | 0.0 | 0.0 | 0.0 | 0.0 | 0.0 | 0.0 | 0.1 | 0.1 | 0.1 | 0.0 | 0.0 | 0.1 | 0.1 | 0.1 |
| | 1.5 | 0.0 | 0.2 | 0.6 | 0.7 | 0.7 | 0.0 | 0.3 | 0.8 | 1.0 | 1.2 | 0.0 | 0.3 | 1.1 | 1.5 | 2.1 |
| | 2.5 | 0.1 | 0.8 | 1.6 | 1.7 | 1.9 | 0.1 | 1.0 | 2.4 | 2.7 | 3.1 | 0.1 | 1.0 | 3.4 | 4.3 | 5.4 |
| | 3.5 | 0.3 | 1.9 | 3.0 | 3.2 | 3.4 | 0.3 | 2.3 | 4.7 | 5.2 | 5.7 | 0.3 | 2.6 | 7.0 | 8.4 | 10.0 |
| | 5.0 | 0.8 | 4.4 | 6.0 | 6.2 | 6.5 | 0.8 | 5.9 | 9.6 | 10.2 | 10.9 | 0.8 | 7.2 | 15.3 | 17.1 | 19.1 |

b)

**Indirect Brine (R245fa) - Pumped**

Power Output per Production-Injection Pair [MWe]

| Temp Gradient [°C km$^{-1}$] | Depth [km] | 0.27m Inj & Prod Diameter | | | | | 0.33m Inj & Prod Diameter | | | | | 0.41m Inj & Prod Diameter | | | | |
|---|---|---|---|---|---|---|---|---|---|---|---|---|---|---|---|---|
| | | 1x10$^{-15}$ m$^2$ | 1x10$^{-14}$ m$^2$ | 5x10$^{-14}$ m$^2$ | 1x10$^{-13}$ m$^2$ | 1x10$^{-12}$ m$^2$ | 1x10$^{-15}$ m$^2$ | 1x10$^{-14}$ m$^2$ | 5x10$^{-14}$ m$^2$ | 1x10$^{-13}$ m$^2$ | 1x10$^{-12}$ m$^2$ | 1x10$^{-15}$ m$^2$ | 1x10$^{-14}$ m$^2$ | 5x10$^{-14}$ m$^2$ | 1x10$^{-13}$ m$^2$ | 1x10$^{-12}$ m$^2$ |
| 20 | 1.0 | 0.0 | 0.0 | 0.0 | 0.0 | 0.0 | 0.0 | 0.0 | 0.0 | 0.0 | 0.0 | 0.0 | 0.0 | 0.0 | 0.0 | 0.0 |
| | 1.5 | 0.0 | 0.0 | 0.0 | 0.0 | 0.0 | 0.0 | 0.0 | 0.0 | 0.0 | 0.0 | 0.0 | 0.0 | 0.0 | 0.0 | 0.0 |
| | 2.5 | 0.0 | 0.0 | 0.0 | 0.0 | 0.0 | 0.0 | 0.0 | 0.0 | 0.0 | 0.0 | 0.0 | 0.0 | 0.0 | 0.0 | 0.0 |
| | 3.5 | 0.0 | 0.0 | 0.0 | 0.1 | 0.2 | 0.0 | 0.0 | 0.0 | 0.1 | 0.3 | 0.0 | 0.0 | 0.0 | 0.1 | 0.4 |
| | 5.0 | 0.0 | 0.1 | 0.4 | 0.5 | 0.8 | 0.0 | 0.1 | 0.4 | 0.7 | 1.3 | 0.0 | 0.1 | 0.4 | 0.8 | 2.1 |
| 35 | 1.0 | 0.0 | 0.0 | 0.0 | 0.0 | 0.0 | 0.0 | 0.0 | 0.0 | 0.0 | 0.0 | 0.0 | 0.0 | 0.0 | 0.0 | 0.0 |
| | 1.5 | 0.0 | 0.0 | 0.0 | 0.0 | 0.0 | 0.0 | 0.0 | 0.0 | 0.0 | 0.1 | 0.0 | 0.0 | 0.0 | 0.0 | 0.1 |
| | 2.5 | 0.0 | 0.0 | 0.2 | 0.3 | 0.6 | 0.0 | 0.0 | 0.2 | 0.4 | 0.9 | 0.0 | 0.0 | 0.2 | 0.4 | 1.5 |
| | 3.5 | 0.0 | 0.3 | 1.1 | 1.5 | 2.1 | 0.0 | 0.3 | 1.4 | 2.1 | 3.5 | 0.0 | 0.3 | 1.5 | 2.6 | 5.9 |
| | 5.0 | 0.1 | 1.1 | 3.2 | 3.8 | 4.5 | 0.1 | 1.2 | 4.2 | 5.6 | 7.6 | 0.1 | 1.2 | 5.1 | 7.9 | 13.0 |
| 50 | 1.0 | 0.0 | 0.0 | 0.0 | 0.0 | 0.0 | 0.0 | 0.0 | 0.0 | 0.0 | 0.0 | 0.0 | 0.0 | 0.0 | 0.0 | 0.1 |
| | 1.5 | 0.0 | 0.0 | 0.1 | 0.1 | 0.4 | 0.0 | 0.0 | 0.1 | 0.1 | 0.6 | 0.0 | 0.0 | 0.1 | 0.1 | 0.8 |
| | 2.5 | 0.0 | 0.4 | 1.4 | 1.9 | 2.7 | 0.0 | 0.4 | 1.6 | 2.5 | 4.4 | 0.0 | 0.4 | 1.7 | 3.1 | 7.4 |
| | 3.5 | 0.1 | 1.1 | 3.5 | 4.4 | 5.4 | 0.1 | 1.2 | 4.5 | 6.3 | 8.9 | 0.1 | 1.2 | 5.3 | 8.6 | 15.3 |
| | 5.0 | 0.1 | 1.5 | 3.5 | 4.1 | 4.6 | 0.1 | 1.5 | 4.9 | 6.2 | 7.7 | 0.1 | 1.6 | 6.3 | 9.1 | 13.3 |

**Figure 3.6: Net Electric Power Production [in MWe] per Injection-Production Well Pair for a) Direct $CO_2$-Pumped and b) Indirect (binary) brine-pumped (R245fa) systems.** At depths less than 1 km, neither system produces electric power. The direct $CO_2$ system produces power at shallower depths than the brine system. The color coding indicates low (red), moderate (yellow), and substantial (green) power production per well pair. The base case, 0.27 m diameter production well and 0.41 m diameter injection well, is bounded by the two boxed values and falls within the yellow power production category, indicating that relatively conservative values are used as a base case and that much higher power production is likely possible (green elements), given more favorable conditions. For example, all else being equal, doubling the drilling depth of the direct $CO_2$ pumped system from 2.5 to 5 km, more than quintuples power production from 0.7 MWe to 3.7 MWe per injection-production well pair. For a single inverted 5-spot well pattern, each power value needs to be multiplied by four. For example, a 2.5 km, 35 °C km$^{-1}$ thermal gradient, 5 x10$^{-14}$ m$^2$ reservoir, with 0.41 m piping produces 0.9 MWe for the well pair using a direct $CO_2$ system and thus 3.6 MWe per inverted 5-spot well pattern. A standard indirect brine

system produces ~22% of the power of the direct $CO_2$ system under equivalent conditions (see also Figure 3.7).

Power output from both systems increases with increases in: reservoir depth and permeability, thermal gradient, and well diameter. The values in Figure 3.6 correspond to a single injection-production well pair and must be multiplied by four to obtain the total power output of a complete inverted 5-spot well system (Figure 3.1). Injection-production well pair electric power output values in Figure 3.6 are color-coded, indicating low (red), moderate (yellow), or substantial (green) power production rates. The base case is bounded by the two boxed values, producing approximately 0.7 MWe (2.8 MWe total for the inverted 5-spot well pattern) at a depth of 2.5 km, increasing more than five times to 3.7 MWe (14.8 MWe) when the depth increases to 5.0 km.

In contrast, power output at a depth of 1.0 km is negligible for all cases. Similarly, for a 20°C $km^{-1}$ thermal gradient with reservoir depths less than 2.5 km, and for a 35°C $km^{-1}$ geothermal gradient with reservoir depths 1.5 km and shallower, negligible amounts of power are produced.

Figure 3.7 shows the difference in electric power generation for the two systems represented by Figure 3.6, i.e., between a direct, pumped $CO_2$ system and a pumped indirect brine system with the latter employing an R245fa secondary power loop. Positive numbers indicate parameters where the $CO_2$ system produces more power than the brine system.

| Temp Gradient [°C km$^{-1}$] | Depth [km] | 0.27m Inj & Prod Diameter | | | | | 0.33m Inj & Prod Diameter | | | | | 0.41m Inj & Prod Diameter | | | | |
|---|---|---|---|---|---|---|---|---|---|---|---|---|---|---|---|---|
| | | 1x10$^{-15}$ m$^2$ | 1x10$^{-14}$ m$^2$ | 5x10$^{-14}$ m$^2$ | 1x10$^{-13}$ m$^2$ | 1x10$^{-12}$ m$^2$ | 1x10$^{-15}$ m$^2$ | 1x10$^{-14}$ m$^2$ | 5x10$^{-14}$ m$^2$ | 1x10$^{-13}$ m$^2$ | 1x10$^{-12}$ m$^2$ | 1x10$^{-15}$ m$^2$ | 1x10$^{-14}$ m$^2$ | 5x10$^{-14}$ m$^2$ | 1x10$^{-13}$ m$^2$ | 1x10$^{-12}$ m$^2$ |
| 20 | 1.0 | | | | | | | | | | | | | | | |
| | 1.5 | | | | | | | | | | | | | | | |
| | 2.5 | | | | | | | | | | | | | | 0.1 | 0.1 |
| | 3.5 | | | 0.1 | | | | | 0.1 | 0.1 | | | | 0.1 | 0.2 | |
| | 5.0 | | | -0.1 | -0.2 | -0.4 | | 0.1 | | -0.2 | -0.6 | | 0.1 | 0.1 | | -1.0 |
| 35 | 1.0 | | | | | | | | | | | | | | | |
| | 1.5 | | | 0.1 | 0.1 | 0.1 | | | 0.1 | 0.2 | 0.1 | | | 0.2 | 0.3 | 0.2 |
| | 2.5 | | 0.2 | 0.3 | 0.3 | | | 0.2 | 0.5 | 0.5 | 0.1 | | 0.2 | 0.7 | 0.9 | 0.3 |
| | 3.5 | 0.1 | 0.3 | -0.1 | -0.4 | -0.9 | 0.1 | 0.3 | 0.2 | -0.3 | -1.4 | | 0.4 | 0.8 | 0.2 | -2.3 |
| | 5.0 | 0.1 | 0.4 | -0.8 | -1.3 | -1.9 | 0.1 | 0.8 | -0.6 | -1.6 | -3.2 | 0.1 | 1.0 | 0.5 | -1.3 | -5.4 |
| 50 | 1.0 | | | | | | | | 0.1 | 0.1 | | | | 0.1 | 0.1 | 0.1 |
| | 1.5 | | 0.2 | 0.5 | 0.5 | 0.4 | | 0.2 | 0.7 | 0.9 | 0.7 | | 0.2 | 1.0 | 1.3 | 1.3 |
| | 2.5 | 0.1 | 0.5 | 0.2 | -0.2 | -0.8 | 0.1 | 0.6 | 0.8 | 0.2 | -1.3 | 0.1 | 0.7 | 1.7 | 1.2 | -1.9 |
| | 3.5 | 0.2 | 0.8 | -0.5 | -1.1 | -2.0 | 0.2 | 1.2 | 0.2 | -1.1 | -3.2 | 0.2 | 1.5 | 1.7 | -0.2 | -5.3 |
| | 5.0 | 0.7 | 3.0 | 2.5 | 2.2 | 1.9 | 0.7 | 4.3 | 4.7 | 4.0 | 3.2 | 0.7 | 5.6 | 9.0 | 7.9 | 5.8 |

**Figure 3.7: Electric Power Production Difference per Injection-Production Well Pair between the Direct Pumped $CO_2$ and the Indirect (binary) Brine (R245fa) Systems [in MWe].** Positive values indicate conditions under which the direct $CO_2$ system produces more electric power than the brine system. The direct $CO_2$ outperforms brine at intermediate depths and permeabilities. The base case is bounded by the two boxed values. From yellow to green colors, the performance advantage of the direct $CO_2$ system, compared to the indirect brine system, increases.

Direct $CO_2$ systems produce more power than brine systems, which are always indirect, in shallower and less permeable reservoirs. The few instances where brine systems produce more power are in hot, particularly permeable locations. The difference between the two systems is most pronounced at a permeability of 5 x$10^{-14}$ m$^2$, due to the lower pressure losses of $CO_2$, relative to those of brine, as it flows through the reservoir (Figure 3.2). At high permeability, the reservoir pressure losses of each system are negligible and the brine systems can produce more power because of the larger heat capacity of brine. Consequently, the direct $CO_2$ system behaves quite differently than its brine alternative, and will produce more power in shallower, cooler, less permeable environments.

Of particular interest is the substantially larger power production in the 50 °C km$^{-1}$, 5.0 km scenarios of the direct $CO_2$ system. While $CO_2$ tends to produce more power in shallower, cooler, less permeable cases, in agreement with Carroll and Stillman (2014); it

deviates from their findings by also producing more power in very hot and deep environments, where the injection temperature of the brine is limited to prevent silica precipitation (DiPippo, 1985) as shown in Figure 3.7. As $CO_2$ is a relatively poor solvent of minerals, it has no such limitation and is able to extract more thermal energy from the geologic fluid, producing more power than brine.

### 3.3.1 Comparison of Net Electric Power Output for the Six Systems for the Base Case

The six systems are compared using the base-case parameters and depths from 1 to 5 km. The results provided in Figure 3.8 show that for a given permeability, temperature gradient, and well diameter, all six systems produce more net electric power as the depth, therefore the reservoir temperature, and therefore system thermodynamic efficiency, increase. Pumped and thermosiphon direct $CO_2$ systems provide greater net power than the brine options until a depth of approximately 3.5 km. The pumped $CO_2$ system always produces more net power than its thermosiphon-driven, unpumped counterpart. Direct $CO_2$ systems produce more net power than indirect $CO_2$ systems except at 5 km, where the indirect $CO_2$ (with $CO_2$ as secondary working fluid) system produces 0.2 MWe (5%) more net power than the Direct $CO_2$ Thermosiphon system.

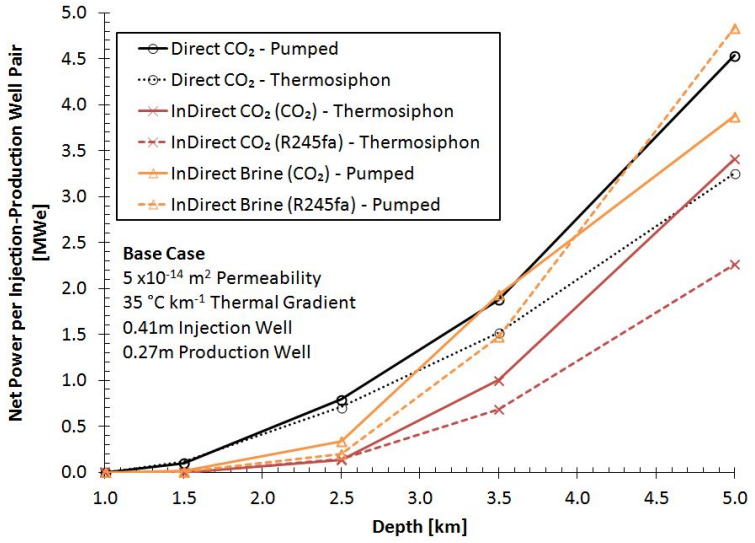


**Figure 3.8: Net Power Output Comparison of all Six Power Systems. [Base-case]** $CO_2$ systems produce several times more power at intermediate depths, such as 2.5 km, than brine.

Pumping direct $CO_2$ systems increases net power production. Use of $CO_2$, as the secondary Rankine fluid, generally produces more power than when using R245fa.

Using $CO_2$ as the secondary Rankine cycle working fluid generally produces more net power than when using R245fa. For example, the use of $CO_2$ as a secondary working fluid, on average, increases net power production by 22% and 20% for brine and $CO_2$ systems, respectively. $CO_2$ Rankine cycles are trans-critical and do not have the "pinch point" problem during heating, as discussed before, and can thus extract more energy from the primary geologic fluid than systems that employ R245fa as the secondary working fluid. This result is consistent with Maraver, et al. (2014). Systems that have a temperature glide (i.e. non-constant temperature heat addition) will tend to avoid the "pinch point" problem and have higher utilization efficiencies (Yin et al., 2013). Future work might include the addition of R32 into the secondary $CO_2$ working fluid, which creates a zeotropic mixture that shifts the ORC to a Brayton cycle, increasing overall heat rejection temperatures, reducing parasitic losses, and decreasing overall cycle pressure (Chen et al., 2011).

In rare circumstances, such as the 5.0 km, 35°C $km^{-1}$ brine scenario shown in Figure 3.8, systems with R245fa as the secondary working fluid produce more net power than trans-critical $CO_2$ systems due to boiler and preheater temperatures that allow a majority of the heat to be extracted from the primary, i.e., subsurface, geologic working fluid. The net power output of the brine system is further limited in the 5.0 km case by the 101°C injection temperature limitation to prevent the precipitation of amorphous silica, as discussed previously.

When $CO_2$ is the primary subsurface heat extraction fluid, a Rankine cycle with $CO_2$ as the secondary working fluid always produces more net power than using R245fa as the secondary working fluid. This results from employing matched primary and secondary working fluids within the counter-flow heat exchanger, which allows a majority of the heat to be transferred with few thermodynamic losses.

### 3.3.2 Electric Power Breakdown for the Base Case

Rankine cycles using $CO_2$ as the secondary working fluid are able to extract more heat from the geothermal fluid than those that use R245fa; however, R245fa cycles tend to have a higher thermal efficiency, consistent with other low-temperature ORC refrigerant comparisons (Shengjun, Huaixin, and Tao, 2011). The decreased thermal efficiency when employing $CO_2$ as the secondary working fluid is due to its large secondary-loop pumping requirement. This is shown in Figure 3.9 by the allotment of power for individual system components. The total height of each bar indicates the gross turbine power output; the net power output for each scenario is shown by the blue (bottom) bar.

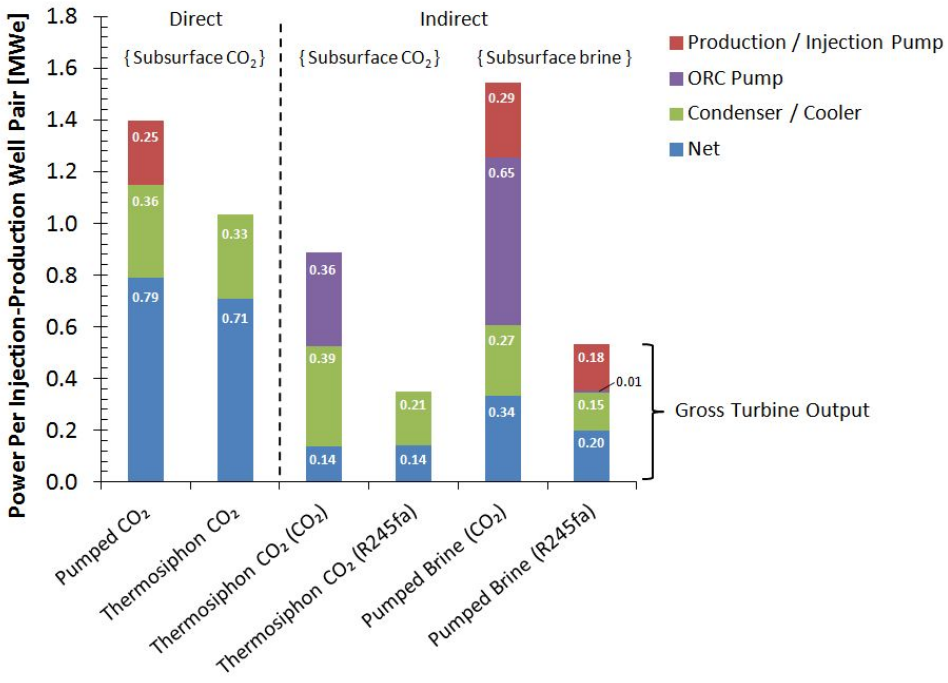


**Figure 3.9: Electric power per injection-production well pair [MWe] breakdown of all six power systems investigated [Base Case].** Direct systems have the smallest portion of the gross turbine power used for parasitic losses. Using $CO_2$ as the secondary Rankine fluid produces more net power; however, substantial power is used to drive the secondary pumps, as opposed to when R245fa is the secondary working fluid. The secondary Rankine fluid is shown in parentheses. The total height of a bar indicates the gross turbine power output.

Direct systems have the smallest number of components and the least parasitic power losses—for the base case shown in Figure 3.9, only 32% of the gross turbine power for

the thermosiphon direct $CO_2$ system is consumed by the fan power for the cooling towers. Conversely, when $CO_2$ is used as the secondary working fluid in an indirect system, 78% to 85% of the gross turbine output can be consumed by parasitic losses. The losses drop to 60% when R245fa is used as the secondary working fluid. Despite the larger parasitic loss fractions, the net power output for the $CO_2$ indirect systems tends to be larger than the R245fa systems.

When $CO_2$ is used as the secondary working fluid, the ORC pump is a large source of parasitic losses. This is due to the small difference in density between the pump and turbine. The pressure differences across both the pump and turbine in a Rankine cycle are essentially equal, but the power is inversely proportional to the density of the fluid that passes through, $P_{turbine/pump} = \dot{m}\int \frac{1}{\rho} dP$, described in substantial detail in Adams et al. (2013). When R245fa is used, the density difference is about two orders of magnitude, decreasing from roughly 1300 kg $m^{-3}$ in the turbine to 10 kg $m^{-3}$ in the pump. When $CO_2$ is used, the reduction in density (800 kg $m^{-3}$ in the pump to 150 kg $m^{-3}$ in the turbine) is much more moderate. The result is that the pumping power, when using $CO_2$ as the secondary working fluid, can be half the total parasitic loss, as shown in Figure 3.9. However when considering the substantially higher rate of heat input obtained by a constant temperature difference between both fluids in the heat exchanger, the $CO_2$ system will generate more net power, typical of supercritical systems (Tofollo et al., 2014). The advantage of using $CO_2$ as the secondary working fluid diminishes in particularly deep, hot geothermal systems, where R245fa has a similar rate of heat input, and with higher thermal efficiency.

### 3.3.3 Electric Power Production Influenced by Well Diameter

Electric power production depends on fluid mass flowrate, which is influenced by the pressure losses in the wells and in the reservoir (Adams, et al., 2014). Therefore, the well diameter may substantially impact the power output of a system. Four well diameters are investigated in varying combinations between the injection and production wells for the

indirect brine, with R245fa as the secondary working fluid, and for the $CO_2$ direct base-case scenarios. The resulting net power outputs are shown in Figure 3.10 as a function of the other major factor of pressure loss: reservoir permeability.

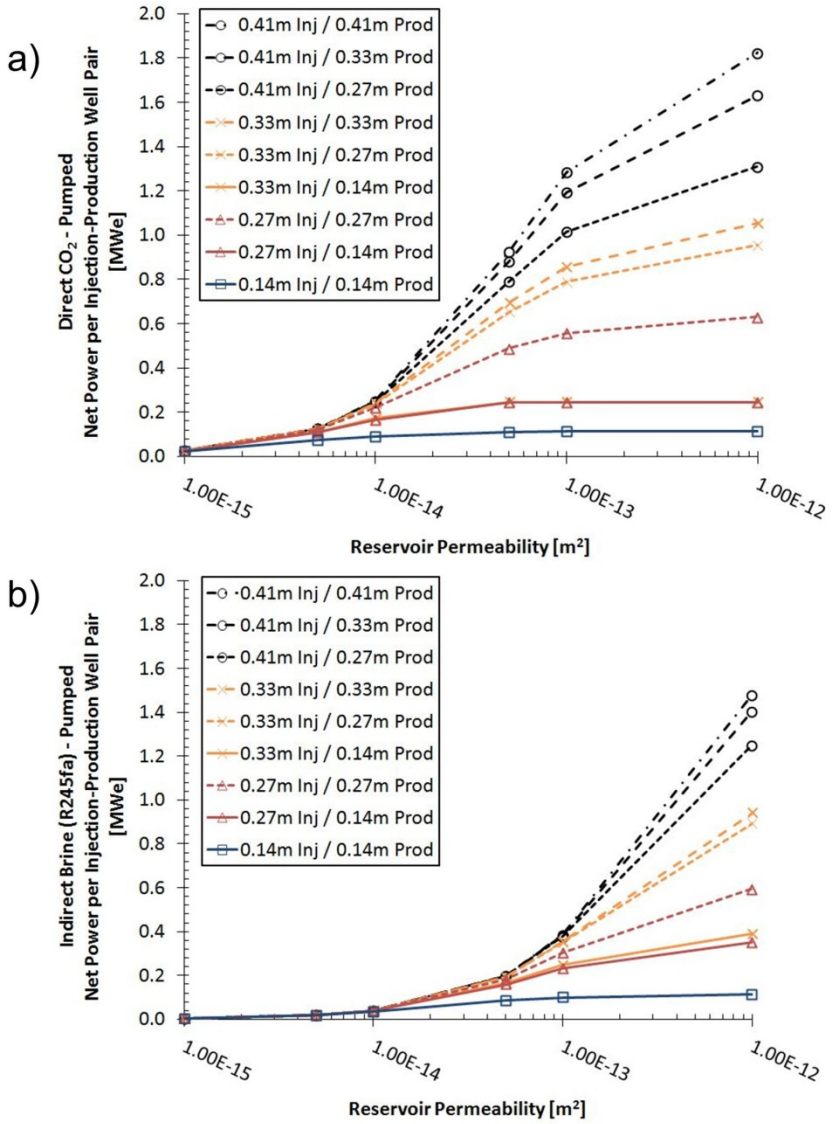


**Figure 3.10: Net Power Output dependence on Well Diameter and Reservoir Permeability for a) direct pumped $CO_2$ and b) indirect pumped brine, the latter with R245fa as the secondary working fluid [Base Case].** At low permeabilities, the power produced tends to be the same for any system. When piping pressure losses become comparable to reservoir pressure losses, at permeabilities above $10^{-14}$ $m^2$ for $CO_2$ and $10^{-13}$ $m^2$ for brine, the well diameter begins to have an impact on power production.

Electric power production increases as the well diameter increases, as expected. The effect of well diameter increase in power production is more pronounced for more permeable reservoirs. When a 0.14 m well diameter is used, system power output is restricted to low values—at most 0.25 MWe and 0.35 MWe for $CO_2$ and brine, respectively—independent of reservoir permeability, because the majority of system pressure losses occur within the wells. Likewise, at small permeabilities below $10^{-14}$ $m^2$ for $CO_2$ and below $10^{-13}$ $m^2$ for brine, the well diameter does not have much impact, but as the reservoir permeability increases, the diameter begins to have a larger impact on power production. Finally, at high reservoir permeabilities of ~$10^{-12}$ $m^2$, the power production curves for $CO_2$ tend to level off with further permeability increases. This differs from brine, for which reservoir pressure losses are still substantial at a permeability of $10^{-12}$ $m^2$, where the curves have not yet inflected; however, the occurrence of reservoir permeability larger than $10^{-12}$ $m^2$ appears unlikely (Runkel et al., 2007; Coleman and Cahan, 2012).

In unreported simulations, injection and production wells are sized to equate pressure losses in each well, but it appears that no sizing guidelines have emerged from these results—except that increasing well diameter always produces more power.

### 3.3.4 Surface Plant and Reservoir Pairing

We evaluate the six systems to determine how net power production varies with reservoir permeability, otherwise using base-case parameters. The resultant power curves are shown in Figure 3.11.

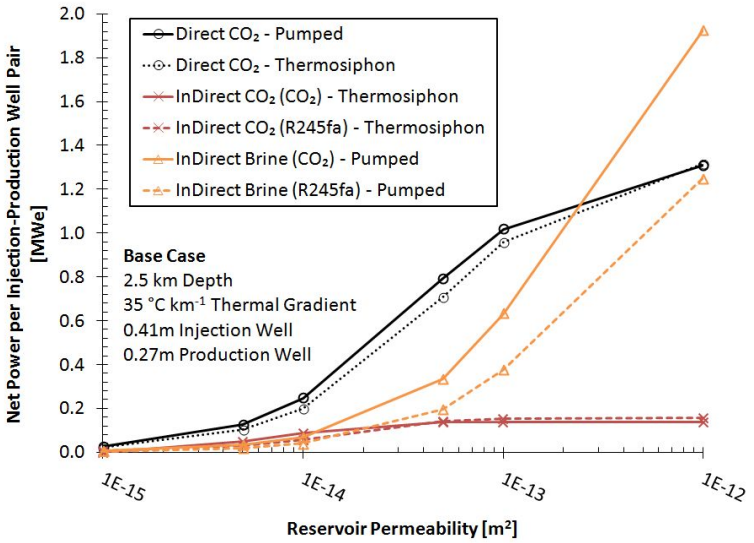


**Figure 3.11: Net Electric Power Output Dependence on System Type and Reservoir Permeability [Base Case].** Direct $CO_2$ systems begin producing power at lower permeabilities than brine and produce more power than indirect systems, except for very high, likely unrealistic (see main text), reservoir permeabilities of ~$10^{-12}$ $m^2$ and higher. The secondary Rankine fluid is shown in parentheses.

Direct $CO_2$ systems produce the most power at permeabilities below about $2x10^{-13}$ $m^2$, while brine systems produce the most power at higher permeabilities. Indirect $CO_2$ systems exhibit low power production throughout the range of permeabilities examined due to the constant low production temperature (~59 °C) and therefore low thermal efficiency of the Rankine cycle. Unlike brine, which drops in pressure substantially but maintains its temperature, $CO_2$ expands in the production well with moderate decreases in both temperature and pressure. Indirect brine Rankine systems have a higher thermal efficiency due to the higher brine production temperature (~102 °C); therefore larger amounts of power are produced when the permeability increases and the system mass flowrate correspondingly increases. Despite the low production temperature (~59 °C), direct $CO_2$ systems produce power by using the large pressure differential between the production and injection wellheads to drive a turbine and therefore have a comparable thermal efficiency to the overall indirect brine system.

At the base-case permeability of 5 $x10^{-14}$ $m^2$, the direct $CO_2$ pumped system produces more power than brine by a factor of 2.3 and 4.1, for $CO_2$ and R245fa secondary systems,

respectively. The decreasing slope of the $CO_2$ curves at high permeabilities, shown in Figure 3.11, indicates that the reservoir pressure losses are becoming less significant and are thus no longer the limiting factor in power production. However the reservoir pressure losses, when using brine, continue to be a significant fraction of the overall system pressure losses. Thus increases in reservoir permeability continue to increase power production for the brine systems. Even at high permeabilities ($1x10^{-12}$ $m^2$), the reservoir parameter (Equation 3.1) for brine is $R$=5.7 kPa s $kg^{-1}$, compared to $R$=1.1 kPa s $kg^{-1}$ for $CO_2$, resulting in greater pressure losses by a factor of 5.3 in the reservoir when using brine than when using $CO_2$. Overall, the results suggest that, at minimum, direct $CO_2$ systems exhibit beneficial electric power production characteristics for permeabilities less than $10^{-13}$ $m^2$, compared to traditional brine systems.

Net electric power production for most of the combinations of depth and thermal gradient follow a similar trend to those listed above for the base case; however, at a depth of 5 km and a geothermal gradient of 50°C $km^{-1}$, as shown in Figure 3.12, several of the trends reverse: the indirect $CO_2$ (R245fa) system can produce more net power than the direct pumped $CO_2$ system; the brine systems never have a larger net power production than the direct pumped $CO_2$ system; and the indirect $CO_2$ system has larger net power production when using R245fa, instead of $CO_2$, as the secondary working fluid.

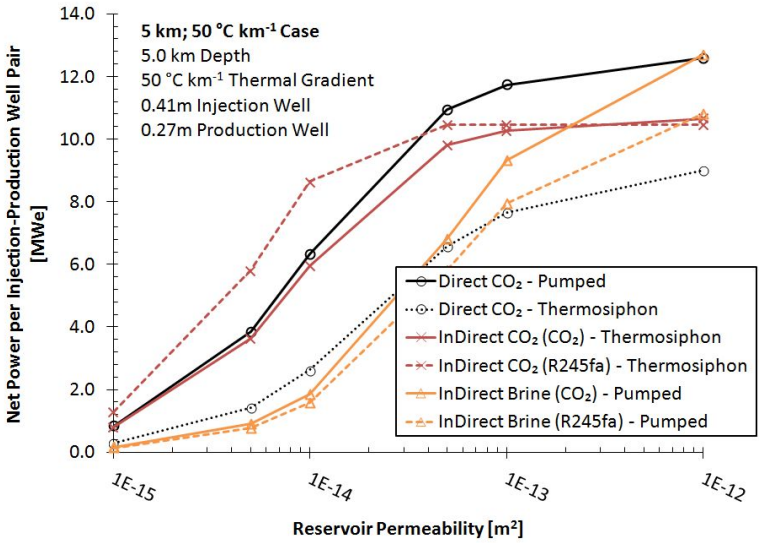


**Figure 3.12: Net Electric Power Output Dependence on System Type and Reservoir Permeability. [5 km; 50 °C km$^{-1}$]** At great depth and temperature, the indirect $CO_2$ scenario produces more electric power than the direct System.

At a depth of 5 km and a geothermal gradient of 50 °C km$^{-1}$, the advantage of using $CO_2$ as the reservoir heat extraction fluid is at its weakest of the investigated cases as $S_{brine}$ is only larger than $S_{CO2}$ by a factor of 2.2 (Figure 3.2). Despite the comparable pressure losses of brine at these depths and pressures, the brine systems do not produce more net power than $CO_2$. This is largely due to the Silica precipitation constraint which limits the temperature reduction of the produced brine to only 85 °C, necessitating the re-injection of 174 °C brine into the reservoir, which still contains useful thermal energy. The $CO_2$-based systems do not suffer from this constraint.

In addition, at this high reservoir temperature, the indirect $CO_2$ (R245fa) system produces more power than the direct pumped $CO_2$ system at permeabilities less than 5 x10$^{-14}$ m$^2$. At a permeability of 10$^{-14}$ m$^2$, the indirect $CO_2$ (R245fa) system has a mass flowrate of 182 kg s$^{-1}$, compared to 160 kg s$^{-1}$ for indirect $CO_2$ ($CO_2$), 167 kg s$^{-1}$ for direct pumped $CO_2$, and 48 kg s$^{-1}$ for indirect brine (R245fa) systems. The high mass flowrate of the indirect $CO_2$ (R245fa) system, combined with its high ORC thermal efficiency, low pumping loads, and a minimal pinch-point constraint cause this system to produce more power under these reservoir conditions than the $CO_2$ ($CO_2$) system, which is uncommon.

## 3.4 Conclusions

We modeled comparable $CO_2$ and brine geothermal systems in sedimentary basins. We provide the following conclusions:

*$CO_2$ experiences less pressure loss in a sedimentary reservoir than brine at comparable fluid mass flowrates.* The pressure loss through a reservoir is directly proportional to the fluid's average specific kinematic viscosity, *S*, for a given reservoir permeability. At a 1 km depth, *S* for brine, $S_{brine}$, is 8 to 12 times greater than *S* for $CO_2$, denoted $S_{CO2}$. At 5 km, $S_{CO2}$ decreases to 2 to 5 times greater than $S_{brine}$. The ratio $S_{brine}/S_{CO2}$ decreases with increasing depth and temperature, indicating $CO_2$ has significantly lower reservoir pressure losses and pumping power requirements in relatively shallower, cooler reservoirs, compared to brine.

*$CO_2$ direct systems produce more net power than brine systems at low to moderate reservoir depths and permeabilities.* $CO_2$ direct systems produce net power at depths as shallow as 1.5 km, and consistently more net power than brine systems until depths of about 3.5 km. Additionally, at permeabilities below $10^{-13}$ $m^2$, $CO_2$ can produce much more power than brine. For example, in the base-case scenario, at a permeability of 5 $x10^{-14}$ $m^2$ and a depth of 2.5 km, the direct pumped $CO_2$ system produces a factor of 4.1 times more net power than the indirect brine system with R245fa as the secondary Rankine fluid (current state-of-the-art technology). The comparative advantage for using $CO_2$ is a result, in part, of the generally low average specific kinematic viscosity, *S*, of $CO_2$ compared to that of brine.

*$CO_2$ direct systems produce substantially more power than brine systems in hot and deep reservoirs.* At a depth of 5 km and a geothermal gradient of 50 °C $km^{-1}$, the $CO_2$ direct pumped system produced between 0.7 MWe and 9.0 MWe more net power (an increase between 40% and 500%) over the brine system using R245fa as the secondary fluid (current state-of-the-art technology). The brine silica precipitation constraint limits the

injection temperature to 176 °C in this case, resulting in the re-injection of useful thermal energy into the geothermal reservoir. Subsurface $CO_2$ is a poor solvent of minerals and, thus, does not have this constraint, which allows the underground $CO_2$ working fluid to capture and utilize more thermal energy.

*$CO_2$ is a better working fluid in secondary Rankine cycles than R245fa.* R245fa cycles operate with a higher thermal efficiency, but 'pinch-point' heat transfer constraints within heat exchangers limit the rate at which thermal energy can be captured from the geologic heat extraction fluid. Thus, $CO_2$ Rankine cycles can operate with more than 50% parasitic losses; however, they nonetheless result in higher net power output because they utilize more of the available geothermal heat. When using $CO_2$ as the secondary working fluid within secondary Rankine cycles, instead of R245fa, for base-case systems, net power production increases 22% and 20% for brine and $CO_2$ systems, respectively.

*Increasing the well diameter substantially increases power production*. Pressure losses within the wells are a major constraint on the fluid mass flowrate of a system, which directly affects power output in both $CO_2$ and brine systems. For example, for a 2.5 km deep, 35°C $km^{-1}$ thermal gradient, and 5 $x10^{-14}$ $m^2$ permeability reservoir, increasing injection and production well diameters from 0.27m to 0.33m to 0.41m, which are still technologically reasonable well diameters, particularly in sedimentary or stratigraphic basin formations (DOE, 2012), increases direct pumped $CO_2$ net power production from 0.49 MWe to 0.70 MWe (+42%) to 0.93 MWe (+33%), respectively, resulting in a 90% overall increase in power by increasing diameter from 0.27 m to 0.41 m. For comparison, typical oil-and-gas well diameters (0.14 m) do not produce significant amounts of power in any configuration simulated, but were used in previous CPG studies (Pan et al., 2015). It is, thus, imperative that power output sensitivity to well diameter is considered in geothermal power production research and implementation.

This study focused on the comparison of electrical power production values of $CO_2$-Plume Geothermal (CPG) and brine geothermal systems for a given set of geologic and

operating conditions. Future research will consider economic factors such as capital cost which also affects the design and operation of geothermal power production systems.

## 3.5 Nomenclature

Nomenclature for these simulations is provided in Table 3.3.

**Table 3.3: Nomenclature**

| | |
|---|---|
| $A$ | Effective Vertical Reservoir Cross-Section [$m^2$] |
| $D$ | Well Pipe Diameter [m] |
| $f$ | Darcy Friction Factor [-] |
| $g$ | Gravitational Constant [9.81 m $s^{-2}$] |
| $h$ | Specific Enthalpy [kJ $kg^{-1}$] |
| $L$ | Effective Reservoir Length [m] |
| $L_{pipe}$ | Pipe length [m] |
| $\dot{m}$ | Fluid Mass Flowrate [kg $s^{-1}$] |
| $P$ | Pressure [kPa] |
| $P_{net}$ | Net Power Generated [$kW_e$] |
| $Q$ | Heat Energy Transfer Rate [$kW_{th}$] |
| $R$ | Reservoir Parameter [kPa s $kg^{-1}$] |
| $S$ | Average Specific Kinematic Viscosity [m $s^{-1}$] |
| $T$ | Temperature [°C] |
| $V$ | Velocity [m $s^{-1}$] |
| $z$ | Elevation [m] |
| $\kappa$ | Scalar Reservoir Permeability [$m^2$] |
| $\mu$ | Dynamic Fluid Viscosity [N s $m^{-2}$] |
| $\rho$ | Fluid Density [kg $m^{-3}$] |

## 3.6 Acknowledgements

Funding from a National Science Foundation (NSF) Sustainable Energy Pathways (SEP) Program grant (1230691) is gratefully acknowledged. We would also like to thank the Initiative for Renewable Energy and the Environment (IREE), a signature program of the Institute on the Environment (IonE) at the University of Minnesota (UMN), for initial seed funding. M.O.S. thanks the George and Orpha Gibson endowment for its support of the Hydrogeology and Geofluids Research Group. Any opinions, findings, conclusions, or recommendations in this material are those of the authors and do not necessarily reflect the views of the NSF, IREE, IonE, or UMN.

## 3.7 Disclaimer

Drs. Randolph and Saar have a significant financial interest, and Dr. Saar has a business interest, in TerraCOH Inc., a company that may commercially benefit from the results of this research. The University of Minnesota has the right to receive royalty income under the terms of a license agreement with TerraCOH Inc. These relationships have been reviewed and managed by the University of Minnesota in accordance with its conflict of interest policies.

## 3.8 Supplemental Information

This section contains assumptions and methodology that are used in the paper "A comparison of electric power output of $CO_2$ Plume Geothermal (CPG) and brine geothermal systems for varying reservoir conditions" by Benjamin M. Adams, Thomas H. Kuehn, Jeffrey M. Bielicki, Jimmy B. Randolph, and Martin O. Saar.

Section 3.8.1 contains error analyses for the regressions to obtain the average specific kinematic viscosity, *S*, used to characterize the TOUGH2 model. The next two sections provide the cooling and condensing tower modeling assumptions for the surface plant (Section 3.8.2) and the boiling temperature optimization point for the indirect systems (Section 3.8.3). Then, results, which were used to determine operating parameters, are shown in Section 3.8.4, including the selection of a mass flowrate (Section 3.8.4.1) and the selection of an approach temperature (Section 3.8.4.2). Section 3.8.5 contains electrical power production tables for the six geothermal and power conversion systems analyzed. Section 3.8.6 provides instructions to obtain the complete dataset used in this paper. Finally, Section 3.8.7 provides references for this supplemental information.

### 3.8.1 Uncertainty Analysis of the Average Specific Kinematic Viscosity, *S*, of the Reservoir

The standard error of *S,* denoted here $SE_S$, is the standard deviation of the predicted values of *S*, given by the regression of the results of the TOUGH2 reservoir simulations

(Equation 3.8). The uncertainty, $U_S$, is based on the standard error, uses a 95% confidence level (CL), and is shown in Equation 3.9. In both equations, $N$ is the number of $S$ values considered.

$$SE_S = \sqrt{\sum \frac{\left(S_{\text{predicted}} - S_{\text{actual}}\right)^2}{N-1}} \tag{3.8}$$

$$U_S = \pm t_{95\%,\text{N}} \frac{SE_S}{\sqrt{N}} \tag{3.9}$$

The standard error is the standard deviation of the predicted $S$ values using our simple Darcy characterization from the actual TOUGH2 simulations. To facilitate comparison between the individual regressions, the standard error and uncertainty values are divided by $S$ found from each regression, and these relative percentages are shown. For $CO_2$, the standard errors are on average 1.35%, with $N$=66 for each regression, an average $R^2$ of 0.98, and an average uncertainty of ±0.33% (95% CL). Similarly for the brine, the average standard error is 0.11%, with $N$=66 for each regression, an average $R^2$ of 0.999, and an average uncertainty of ±0.03% (95% CL). These excellent fits support the validity of approximating TOUGH2 reservoir behavior within 1% by using $S$ instead of solving TOUGH2 simultaneously for each case with the surface power plant models.

The results of a multi-simulator comparison by Class et al. (2009) are used to estimate the uncertainty of TOUGH2. For a fixed pressure drop, Class et al., (2009) compared mass flowrates using six simulators and found a 6% variation in the results across simulators. Therefore, the simulator uncertainty dominates the characterization uncertainties and we thus use an overall uncertainty of the reservoir pressure drop of ±6%.

### 3.8.2 Cooling and Condensing Tower Performance

Cooling and condensing towers are two similar types of equipment that remove heat from a fluid, but their performances vary slightly from each other. A cooling tower reduces the temperature of a single-phase fluid, while a condensing tower changes the phase of a

fluid from gas to liquid; the different fluid state mixtures within the piping cause differing heat transfer characteristics of each tower type. Thus, both cooling and condensing towers are separately characterized hereafter.

The cooling and condensing towers are modeled to determine the parasitic power losses they impose on the power plant. The low thermal efficiency of geothermal systems in general (on the order of 10%) requires 10 MW of thermal energy to be rejected through the condensing tower to generate 1 MW of electrical power. To achieve these levels of heat rejection at the surface, large volumes of air must be passed through the towers, and therefore large cooling fan loads are needed. We use existing cooling and condensing tower performance data for three Baltimore AirCoil production models: 1) PC2-509-1218-30, 509 nominal ton, R22, condensing tower, and models 2) FXV-0812B-12D-J and 3) FXV-1212C-16Q-K, which are 98 ton and 123 ton, respectively, glycol, closed-circuit cooling towers (BAC, 2013). Each of the towers are capable of both dry (sensible) and wet (sensible plus latent) cooling, therefore they are characterized with respect to the cooling method that is chosen. When $CO_2$ is used as the working fluid in a tower, it may be cooled or condensed at temperatures far below 0°C, unlike water. Thus, and as BAC does not produce $CO_2$ equipment, R22 and Glycol are selected as the working fluid, in lieu of water.

The parasitic power load is characterized by the parasitic load fraction, $\lambda$, which is the ratio of parasitic energy load ($kW_e$) to heat rejection energy ($kW_{th}$), as shown in Equations (3.10-3.11). This form of $\lambda$ does not account for variations in heat transfer when varying fluid types and flowrates are used in the tower.

$$P_{cooler} = \lambda_{cooler} Q_{cooler} \tag{3.10}$$

$$P_{condenser} = \lambda_{condenser} Q_{condenser} \tag{3.11}$$

The parasitic load values are found using an online calculator (BAC, 2013) for all three towers for approach temperatures of 4°C to 40°C, wet and dry cooling conditions, ambient temperatures from -25°C to 25°C, and ranges from 2°C to 20°C. The approach temperature is the difference between the exit temperature of the tower and either the ambient wet-bulb or dry-bulb temperatures, depending on the cooling type. The range is the difference between the entrance and exit temperature of the cooled fluid—the range for a condensing fluid is always zero. When the BAC online calculator did not provide results because the calculated flowrate was outside a predefined range for the conditions submitted, those data were omitted. The results of these simulations are shown in Figure 3.13.

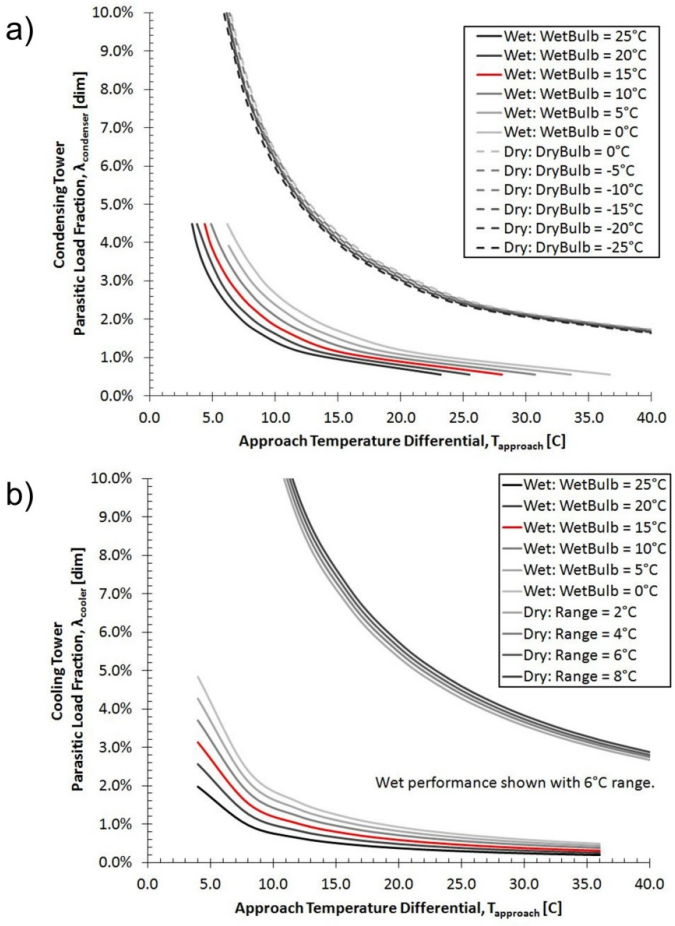


**Figure 3.13: Parasitic Load Fraction, λ, for a) Wet and Dry Condensing Towers and b) Wet and Dry Cooling Towers with respect to wet-bulb and dry-bulb temperature.** Using a wet tower substantially decreases the parasitic load. Dry tower load does not vary substantially with dry-bulb temperature (a), thus, cooling tower performance was characterized with respect to

temperature range (b). The parasitic load fraction is proportional to the inverse approach temperature—doubling the approach temperature halves the parasitic load.

We regress the data for the curves in Figure 3.13 using Equation (3.12) as the regression model. The resulting coefficients are shown in Table 3.4. Also shown are the overall standard error and uncertainty in calculating the parasitic load fraction, λ, which are found using the difference between the load fraction provided by BAC and the value calculated from Equation 3.12, using Equations 3.10-3.11.

$$\lambda = a \cdot T_r + b \cdot T_r \cdot T_{wb} + c \cdot \left(\frac{1}{T_{app}}\right) + d \cdot T_{wb} \cdot \left(\frac{1}{T_{app}}\right) + e \cdot T_r \cdot \left(\frac{1}{T_{app}}\right) \qquad (3.12)$$

**Table 3.4: Coefficients for regression curves for the parasitic load fraction, λ, of cooling and condensing towers.**

| Type | | a | b | c | d | e | $SE_\lambda$ | $U_\lambda$ |
|---|---|---|---|---|---|---|---|---|
| cooling | wet | $-1.00 \times 10^{-4}$ | $1.91 \times 10^{-6}$ | 0.196 | - 0.00462 | | ± 0.0007 | ± 0.00003 |
| cooling | dry | | | 1.044 | | 0.0131 | ± 0.006 | ± 0.0009 |
| condensing | wet | | | 0.268 | - 0.0049 | | ± 0.0009 | ± 0.0002 |
| condensing | dry | | | 0.619 | | | ± 0.002 | ± 0.0005 |

The performance of the wet tower depends on the ambient air temperature; the parasitic load fraction decreases as the ambient wet-bulb temperature increases. In contrast, the dry tower performance does not appear to vary substantially by dry-bulb temperature, so that we do not use it as a factor. The dry tower requires much more parasitic power than the wet tower. For example, at a 15°C ambient temperature and 10°C approach temperature, the wet tower parasitic load fractions are 1.3% (cooling) and 1.6% (condensing), whereas the dry tower parasitic load fractions are 9.2x (cooling) and 3.2x (condensing) higher. Ultimately, the selection of either a condensing tower or a cooling tower depends on the processes (cooling, condensing, or both) necessary to reduce the fluid to a saturated liquid state.

Due to the larger parasitic loads for dry cooling, wet tower technology is always preferred, even when the ambient temperature is below $0^{o}$C. The condensing temperature within a wet cooling tower may not be below the freezing point of water, otherwise ice will damage the unit. Therefore the condensing or cooling temperature of any liquid passing through a cooling or condensing wet tower is at least 7°C. At subzero ambient temperatures, we increase the approach temperature to maintain the outlet temperature at 7°C. Increasing the heat rejection temperature decreases the thermal efficiency of a system, but when the ambient temperature is below $0^{o}$C, the decrease in parasitic load fraction due to the increased approach temperature still results in higher power output than is attainable with a dry system.

### 3.8.3 Indirect System Operating Point Optimization

When using R245fa as the secondary working fluid in an Organic Rankine Cycle, the power plant operator sets the boiling temperature by controlling the high-side pressure (Figure 3.5, States 9, 13, and 14 – see Section 3.2.3.2). At high boiling temperatures, the thermal efficiency of the system is large, but the overall mass flowrate is small because of the pinch-point constraint. Similarly, at low boiling temperatures, the thermal efficiency of the Rankine cycle is low, but the mass flowrate is large. Therefore, an optimal boiling temperature for R245fa, for each inlet temperature into the Rankine cycle (Figure 3.5, State 6), exists, where power production is maximized. Figure 3.14 shows this optimal boiling temperature for each inlet $CO_2$ or brine temperature. The discontinuity around 180°C inlet temperature for R245fa is due to the non-linear shifting ratio of boiling to preheating thermal energy as boiling temperature increases and approaches the critical temperature, $T_{crit,R245fa}$ = 154 °C.

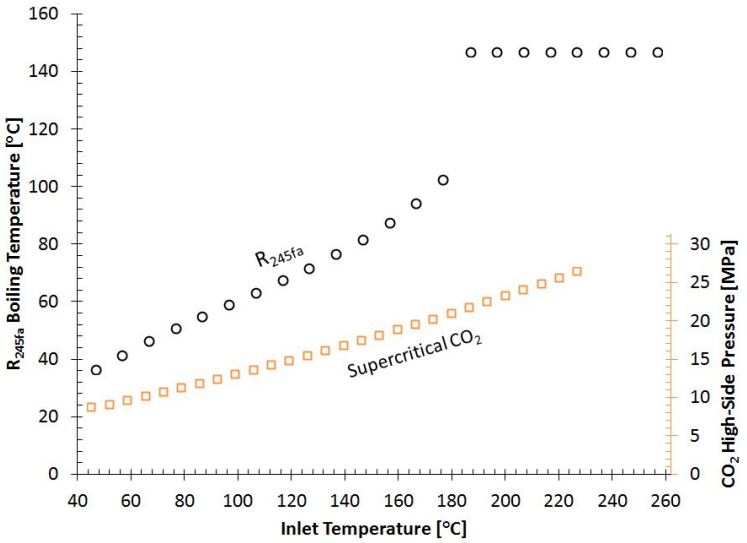


**Figure 3.14: Secondary Rankine Cycle Operating Points.** The high-side temperature or pressure of the secondary Rankine cycle is used which will produce the most power, based on its working fluid.

Similarly, the power plant operator sets the high-side pressure of the supercritical $CO_2$ Rankine indirect system. If the pressure is too high, the pump outlet temperature becomes high, and the energy input into the system decreases, decreasing power. If the pressure is too low, the pressure differential across the turbine is small, and power decreases. Therefore, an optimal secondary $CO_2$ pressure exists for all primary inlet $CO_2$ or brine temperatures (Figure 3.5, State 6), shown on the secondary axis in Figure 3.14. The secondary working fluid $CO_2$ system does not operate near the critical point resulting in a relatively linear curve.

We perform a linear regression for each of the roughly linear regions in Figure 3.14. For supercritical $CO_2$, the optimal high-side pressure is predicted by Equation 3.13:

$$P_{CO2}(\text{MPa}) = 0.096 * T_{inlet}(°\text{C}) + 3.78, \qquad (3.13)$$

with an $R^2$ value of 0.995. Similarly, for brine with an inlet temperature below 180°C, the optimal boiling temperature is predicted by Equation 3.14:

$$T_{R245fa}(°C) = 0.48 * T_{inlet}(°C) + 13.1, \quad (3.14)$$

with an $R^2$ value of 0.991, whereas for inlet temperatures above 180°C, the optimal boiling temperature is constant at 147°C.

### 3.8.4 Assumptions and Reduction of Parameters

Given the large number of variables, the fluid mass flowrate, approach temperature, and cooling tower technology are examined in the following sections and then fixed for the simulations in the main paper. To note, using the average annual temperature results in conservative estimates of the average annual power production.

#### 3.8.4.1 Optimal Fluid Mass Flowrate

The fluid mass flowrate is set in different ways for each type of system. In pumped systems, the mass flowrate is set by regulating the pumping power applied, and thus pressure differential induced, by the pumps. In thermosiphon-driven systems, the mass flowrate is set by regulating the outlet pressure of the turbine or by adjusting the pressure drop through the pre-injection throttle valve. Figure 3.15 shows the power curves for the base case, un-pumped, direct system. Analogous power curves exist for each combination of well diameter, geothermal temperature gradient, reservoir depth and permeability, and surface plant design. For each combination, there is a mass flowrate where system inefficiencies and throughput are in balance, and the net power output is maximized.

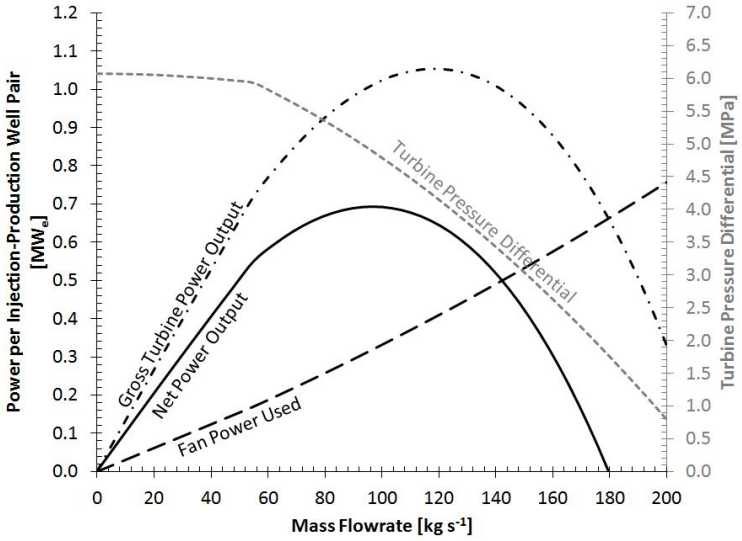


**Figure 3.15 (Also Figure 4 in main text): Example of Net Power Output of an Un-pumped Direct $CO_2$ System for One Injection-Production Well Pair as a function of Fluid Mass Flowrate. [Base-case]** At low fluid mass flowrates, turbine power output is small, despite high thermodynamic cycle efficiencies. At high mass flowrates, turbine output drops due to decreasing pressure differential caused by increased system pressure losses. This interaction results in a net power curve with a maximum value (here ~100 kg $s^{-1}$). This mass flowrate is unique and must be found for every scenario.

Figure 3.15 illustrates the tradeoff between net power production and losses in the unpumped direct $CO_2$ Plume Geothermal (CPG) system base-case for one injection-production well pair. At low mass flowrates, the system thermodynamic efficiency is high due to the small amount of irreversibilities (pressure losses – minor temperature losses are not accounted for due to the adiabatic assumption), but the net power generated is also small due to low fluid mass flowrates. As mass flowrate increases, the pressure losses increase by the square of the mass flowrate (Equation 6) and less pressure is available to drive the turbine. As a result, the net power output goes to zero at high mass flowrates. In this example, the net power reaches zero when the mass flowrate reaches 180 kg $s^{-1}$, where the gross turbine output equals the parasitic fan load.

Thus, the mass flowrate that provides the largest net power output for each scenario is used.

### 3.8.4.2 Approach Temperature

In the direct system and on the secondary side of the indirect system, the approach temperature is set by selecting the outlet pressure of the turbine, thereby selecting the condensing temperature. To demonstrate the strong influence of approach temperature, the net power output is shown in Figure 3.16 for approach temperatures ranging from 4 °C to 30 °C for the direct, pumped base-case scenario.

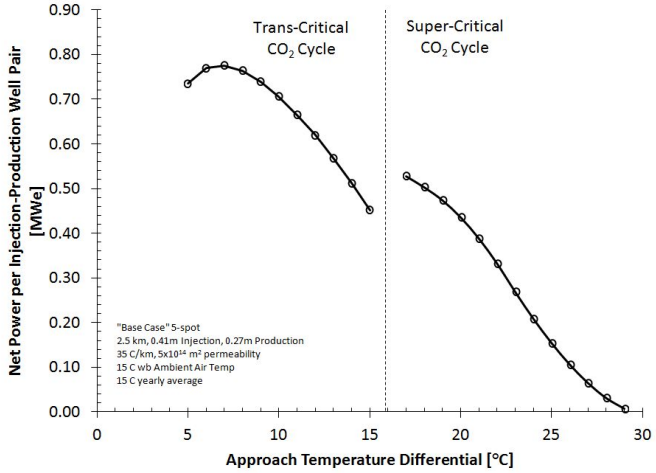


**Figure 3.16: Net Power Output for the Base Case.** Increasing the approach temperature increases the injection temperature of the geothermal fluid and decreases turbine power output, whereas decreasing the approach temperature decreases the parasitic condensing/cooling tower load. This results in an optimal net power output near 7 °C which is used in all other scenarios.

At low approach temperatures, the system thermodynamic efficiency is higher than at large approach temperatures because the heat rejection temperature is low, however, the parasitic condensing and cooling loads are also high. As the approach temperature increases, the parasitic load drops faster than the system efficiency. The optimal approach temperature, yielding maximum net power output, exists near 7°C, which is used hereafter.

The net power increases when the approach temperature increases from 15°C to 17°C due to the substantial decrease in pumping power needed in the super-critical cycle. In the trans-critical cycle, the pressure at the turbine exit (Figure 3.3, State 5) is fixed by the

condensation temperature (Figure 3.3, State 6); however, in the super-critical cycle, the pressure and temperature can vary independently. The result is a larger turbine exit pressure while maintaining the same approach temperature, but reducing pumping power by 90%. This thermodynamic trade-off only occurs near the critical point of $CO_2$ (approach temperature = 16°C), and overall net power is still maximized using the trans-critical cycle with an approach temperature of 7°C.

#### 3.8.4.3 Average Annual Power Production

The average annual wet-bulb temperature for a site can be used to approximate the average annual power production. The direct, pumped $CO_2$ system is simulated for the base-case at two sites over the course of a 'normal' year, averaged, and then compared with a single simulation using only the average wet-bulb temperature. Power production values are simulated for Dallas, Texas (TX), and Williston, North Dakota (ND), which have average wet-bulb temperatures of 14.3°C and 2.5°C, respectively. These two cities are at different latitudes within the continental United States and can thus represent the expected extremes in ambient conditions. The monthly wet-bulb temperature values are obtained from the Climate Normals, provided by the National Climactic Data Center (NCDC, 2013).

Our simulated average power production over the year for Dallas is 0.90 MWe per injection-production well pair in the inverted 5-spot well pattern, using the monthly average wet bulb temperature, compared with 0.81 MWe, a decrease of 11%, when the annual average value is used. Similarly, the average power production per injection-production well pair in Williston is 1.41 MWe using monthly values, and decreases only 0.7% to 1.40 MWe when the annual average wet-bulb temperature is used. The inverted 5-spot well pattern contains 4 injection-production pairs, thus, the injection-production power must be multiplied by 4 to obtain the power production for one inverted 5-spot well system (Figure 3.1). Thus, the inverted 5-spot well systems are expected to generate an average of approximately 3.2 MWe and 5.6 MWe in Dallas and Williston,

respectively. Typically, multiple such 5-spot systems would be combined in one overall geothermal power plant system.

Williston, ND, exhibits the small difference in monthly versus yearly-averaged power production because of the extremely cold winter conditions. When the ambient temperature drops below $0^{o}$C, the condensing temperature of the tower must stay above $0^{o}$C. The thermal efficiency of most systems increases with decreasing wet-bulb temperatures, but sub-zero weather mitigates this effect and results in a linear relationship between temperature and power production. Warmer climates, like Dallas, TX, have larger changes in thermal efficiency throughout the year, and tend to produce on average more power than the average annual temperature would predict. Therefore, the average annual temperature is typically a conservative estimate of average annual power production with an estimated uncertainty of 11%.

### 3.8.5 Net Electric Output Power Tables

The net electric power produced for all six surface plant types are shown in Figure 3.17, where each value represents a single injection-production pair. The values must be multiplied by four to obtain the total power production for the entire inverted 5-spot well system. Each of the surface plant tables displays 225 values of the 945 calculated. The parameters which are not displayed are: one permeability of 5 $x10^{-15}$ $m^2$ and six combinations of injection (Inj) and production (Prod) well inner diameter pairs: (0.41m Inj / 0.33m Prod), (0.41m Inj / 0.27m Prod), (0.33m Inj / 0.27m Prod), (0.33m Inj / 0.14m Prod), (0.27m Inj / 0.14m Prod), and (0.14m Inj / 0.14m Prod).

**Direct $CO_2$ - Pumped**

Power Output per Production-Injection Pair [MWe]

| Temp Gradient [°C km⁻¹] | Depth [km] | 0.27m Inj & Prod Diameter | | | | | 0.33m Inj & Prod Diameter | | | | | 0.41m Inj & Prod Diameter | | | | |
|---|---|---|---|---|---|---|---|---|---|---|---|---|---|---|---|---|
| | | 1x10⁻¹⁵ m² | 1x10⁻¹⁴ m² | 5x10⁻¹⁴ m² | 1x10⁻¹³ m² | 1x10⁻¹² m² | 1x10⁻¹⁵ m² | 1x10⁻¹⁴ m² | 5x10⁻¹⁴ m² | 1x10⁻¹³ m² | 1x10⁻¹² m² | 1x10⁻¹⁵ m² | 1x10⁻¹⁴ m² | 5x10⁻¹⁴ m² | 1x10⁻¹³ m² | 1x10⁻¹² m² |
| 20 | 1.0 | 0.0 | 0.0 | 0.0 | 0.0 | 0.0 | 0.0 | 0.0 | 0.0 | 0.0 | 0.0 | 0.0 | 0.0 | 0.0 | 0.0 | 0.0 |
| | 1.5 | 0.0 | 0.0 | 0.0 | 0.0 | 0.0 | 0.0 | 0.0 | 0.0 | 0.0 | 0.0 | 0.0 | 0.0 | 0.0 | 0.0 | 0.0 |
| | 2.5 | 0.0 | 0.0 | 0.0 | 0.0 | 0.0 | 0.0 | 0.0 | 0.0 | 0.1 | 0.1 | 0.0 | 0.0 | 0.0 | 0.1 | 0.1 |
| | 3.5 | 0.0 | 0.0 | 0.1 | 0.1 | 0.1 | 0.0 | 0.0 | 0.1 | 0.2 | 0.2 | 0.0 | 0.0 | 0.2 | 0.3 | 0.4 |
| | 5.0 | 0.0 | 0.1 | 0.3 | 0.3 | 0.4 | 0.0 | 0.2 | 0.4 | 0.5 | 0.6 | 0.0 | 0.2 | 0.6 | 0.8 | 1.1 |
| 35 | 1.0 | 0.0 | 0.0 | 0.0 | 0.0 | 0.0 | 0.0 | 0.0 | 0.0 | 0.0 | 0.0 | 0.0 | 0.0 | 0.0 | 0.0 | 0.0 |
| | 1.5 | 0.0 | 0.0 | 0.1 | 0.1 | 0.1 | 0.0 | 0.0 | 0.1 | 0.2 | 0.2 | 0.0 | 0.0 | 0.2 | 0.3 | 0.3 |
| | 2.5 | 0.0 | 0.2 | 0.5 | 0.6 | 0.6 | 0.0 | 0.2 | **0.7** | 0.9 | 1.1 | 0.0 | 0.3 | **0.9** | 1.3 | 1.8 |
| | 3.5 | 0.1 | 0.6 | 1.0 | 1.1 | 1.2 | 0.1 | 0.7 | 1.6 | 1.8 | 2.1 | 0.1 | 0.7 | 2.3 | 2.9 | 3.6 |
| | 5.0 | 0.2 | 1.5 | 2.3 | 2.5 | 2.6 | 0.2 | 1.9 | 3.7 | 4.0 | 4.4 | 0.2 | 2.2 | 5.6 | 6.5 | 7.7 |
| 50 | 1.0 | 0.0 | 0.0 | 0.0 | 0.0 | 0.0 | 0.0 | 0.0 | 0.1 | 0.1 | 0.1 | 0.0 | 0.0 | 0.1 | 0.1 | 0.1 |
| | 1.5 | 0.0 | 0.2 | 0.6 | 0.7 | 0.7 | 0.0 | 0.3 | 0.8 | 1.0 | 1.2 | 0.0 | 0.3 | 1.1 | 1.5 | 2.1 |
| | 2.5 | 0.1 | 0.8 | 1.6 | 1.7 | 1.9 | 0.1 | 1.0 | 2.4 | 2.7 | 3.1 | 0.1 | 1.0 | 3.4 | 4.3 | 5.4 |
| | 3.5 | 0.3 | 1.9 | 3.0 | 3.2 | 3.4 | 0.3 | 2.3 | 4.7 | 5.2 | 5.7 | 0.3 | 2.6 | 7.0 | 8.4 | 10.0 |
| | 5.0 | 0.8 | 4.4 | 6.0 | 6.2 | 6.5 | 0.8 | 5.9 | 9.6 | 10.2 | 10.9 | 0.8 | 7.2 | 15.3 | 17.1 | 19.1 |

**Direct $CO_2$ - No Pump**

Power Output per Production-Injection Pair [MWe]

| Temp Gradient [°C km⁻¹] | Depth [km] | 0.27m Inj & Prod Diameter | | | | | 0.33m Inj & Prod Diameter | | | | | 0.41m Inj & Prod Diameter | | | | |
|---|---|---|---|---|---|---|---|---|---|---|---|---|---|---|---|---|
| | | 1x10⁻¹⁵ m² | 1x10⁻¹⁴ m² | 5x10⁻¹⁴ m² | 1x10⁻¹³ m² | 1x10⁻¹² m² | 1x10⁻¹⁵ m² | 1x10⁻¹⁴ m² | 5x10⁻¹⁴ m² | 1x10⁻¹³ m² | 1x10⁻¹² m² | 1x10⁻¹⁵ m² | 1x10⁻¹⁴ m² | 5x10⁻¹⁴ m² | 1x10⁻¹³ m² | 1x10⁻¹² m² |
| 20 | 1.0 | 0.0 | 0.0 | 0.0 | 0.0 | 0.0 | 0.0 | 0.0 | 0.0 | 0.0 | 0.0 | 0.0 | 0.0 | 0.0 | 0.0 | 0.0 |
| | 1.5 | 0.0 | 0.0 | 0.0 | 0.0 | 0.0 | 0.0 | 0.0 | 0.0 | 0.0 | 0.0 | 0.0 | 0.0 | 0.0 | 0.0 | 0.0 |
| | 2.5 | 0.0 | 0.0 | 0.0 | 0.0 | 0.0 | 0.0 | 0.0 | 0.0 | 0.0 | 0.0 | 0.0 | 0.0 | 0.0 | 0.0 | 0.0 |
| | 3.5 | 0.0 | 0.0 | 0.1 | 0.1 | 0.2 | 0.0 | 0.0 | 0.1 | 0.2 | 0.3 | 0.0 | 0.0 | 0.2 | 0.3 | 0.4 |
| | 5.0 | 0.0 | 0.2 | 0.3 | 0.4 | 0.4 | 0.0 | 0.2 | 0.5 | 0.6 | 0.7 | 0.0 | 0.2 | 0.7 | 0.9 | 1.2 |
| 35 | 1.0 | 0.0 | 0.0 | 0.0 | 0.0 | 0.0 | 0.0 | 0.0 | 0.0 | 0.0 | 0.0 | 0.0 | 0.0 | 0.0 | 0.0 | 0.0 |
| | 1.5 | 0.0 | 0.0 | 0.1 | 0.1 | 0.1 | 0.0 | 0.1 | 0.2 | 0.2 | 0.2 | 0.0 | 0.1 | 0.2 | 0.3 | 0.3 |
| | 2.5 | 0.0 | 0.2 | 0.4 | 0.5 | 0.6 | 0.0 | 0.2 | **0.6** | 0.8 | 1.0 | 0.0 | 0.2 | **0.8** | 1.1 | 1.7 |
| | 3.5 | 0.1 | 0.4 | 0.9 | 1.0 | 1.1 | 0.1 | 0.5 | 1.3 | 1.5 | 1.8 | 0.1 | 0.5 | 1.7 | 2.3 | 3.1 |
| | 5.0 | 0.1 | 1.0 | 1.7 | 1.8 | 1.9 | 0.1 | 1.1 | 2.6 | 2.9 | 3.3 | 0.1 | 1.3 | 3.7 | 4.6 | 5.7 |
| 50 | 1.0 | 0.0 | 0.0 | 0.0 | 0.0 | 0.0 | 0.0 | 0.0 | 0.1 | 0.1 | 0.1 | 0.0 | 0.0 | 0.1 | 0.1 | 0.1 |
| | 1.5 | 0.0 | 0.2 | 0.6 | 0.7 | 0.7 | 0.0 | 0.2 | 0.8 | 1.0 | 1.2 | 0.0 | 0.2 | 1.0 | 1.5 | 2.1 |
| | 2.5 | 0.1 | 0.5 | 1.2 | 1.3 | 1.5 | 0.1 | 0.6 | 1.7 | 2.0 | 2.5 | 0.1 | 0.6 | 2.2 | 3.1 | 4.3 |
| | 3.5 | 0.1 | 1.0 | 1.9 | 2.1 | 2.3 | 0.1 | 1.1 | 2.8 | 3.3 | 3.9 | 0.1 | 1.2 | 3.9 | 5.2 | 6.8 |
| | 5.0 | 0.3 | 2.0 | 3.4 | 3.6 | 3.9 | 0.3 | 2.4 | 5.2 | 5.8 | 6.5 | 0.3 | 2.7 | 7.7 | 9.3 | 11.3 |

**Indirect Brine ($CO_2$) - Pumped**

Power Output per Production-Injection Pair [MWe]

| Temp Gradient [°C km⁻¹] | Depth [km] | 0.27m Inj & Prod Diameter | | | | | 0.33m Inj & Prod Diameter | | | | | 0.41m Inj & Prod Diameter | | | | |
|---|---|---|---|---|---|---|---|---|---|---|---|---|---|---|---|---|
| | | 1x10⁻¹⁵ m² | 1x10⁻¹⁴ m² | 5x10⁻¹⁴ m² | 1x10⁻¹³ m² | 1x10⁻¹² m² | 1x10⁻¹⁵ m² | 1x10⁻¹⁴ m² | 5x10⁻¹⁴ m² | 1x10⁻¹³ m² | 1x10⁻¹² m² | 1x10⁻¹⁵ m² | 1x10⁻¹⁴ m² | 5x10⁻¹⁴ m² | 1x10⁻¹³ m² | 1x10⁻¹² m² |
| 20 | 1.0 | 0.0 | 0.0 | 0.0 | 0.0 | 0.0 | 0.0 | 0.0 | 0.0 | 0.0 | 0.0 | 0.0 | 0.0 | 0.0 | 0.0 | 0.0 |
| | 1.5 | 0.0 | 0.0 | 0.0 | 0.0 | 0.0 | 0.0 | 0.0 | 0.0 | 0.0 | 0.0 | 0.0 | 0.0 | 0.0 | 0.0 | 0.0 |
| | 2.5 | 0.0 | 0.0 | 0.0 | 0.0 | 0.0 | 0.0 | 0.0 | 0.0 | 0.0 | 0.1 | 0.0 | 0.0 | 0.0 | 0.0 | 0.1 |
| | 3.5 | 0.0 | 0.0 | 0.1 | 0.1 | 0.3 | 0.0 | 0.0 | 0.1 | 0.2 | 0.5 | 0.0 | 0.0 | 0.1 | 0.2 | 0.7 |
| | 5.0 | 0.0 | 0.1 | 0.6 | 0.8 | 1.1 | 0.0 | 0.2 | 0.7 | 1.0 | 1.8 | 0.0 | 0.2 | 0.7 | 1.3 | 3.1 |
| 35 | 1.0 | 0.0 | 0.0 | 0.0 | 0.0 | 0.0 | 0.0 | 0.0 | 0.0 | 0.0 | 0.0 | 0.0 | 0.0 | 0.0 | 0.0 | 0.0 |
| | 1.5 | 0.0 | 0.0 | 0.0 | 0.0 | 0.1 | 0.0 | 0.0 | 0.0 | 0.0 | 0.1 | 0.0 | 0.0 | 0.0 | 0.0 | 0.2 |
| | 2.5 | 0.0 | 0.1 | 0.3 | 0.5 | 0.9 | 0.0 | 0.1 | **0.3** | 0.6 | 1.4 | 0.0 | 0.1 | **0.3** | 0.7 | 2.3 |
| | 3.5 | 0.0 | 0.4 | 1.5 | 2.0 | 2.7 | 0.0 | 0.4 | 1.8 | 2.7 | 4.4 | 0.0 | 0.4 | 2.0 | 3.5 | 7.4 |
| | 5.0 | 0.1 | 0.9 | 2.5 | 3.0 | 3.6 | 0.1 | 0.9 | 3.4 | 4.5 | 6.0 | 0.1 | 0.9 | 4.1 | 6.3 | 10.4 |
| 50 | 1.0 | 0.0 | 0.0 | 0.0 | 0.0 | 0.1 | 0.0 | 0.0 | 0.0 | 0.0 | 0.1 | 0.0 | 0.0 | 0.0 | 0.0 | 0.1 |
| | 1.5 | 0.0 | 0.0 | 0.1 | 0.2 | 0.6 | 0.0 | 0.0 | 0.1 | 0.2 | 0.9 | 0.0 | 0.0 | 0.1 | 0.3 | 1.3 |
| | 2.5 | 0.0 | 0.4 | 1.6 | 2.3 | 3.2 | 0.0 | 0.4 | 1.9 | 3.1 | 5.2 | 0.0 | 0.4 | 2.1 | 3.7 | 8.9 |
| | 3.5 | 0.1 | 0.9 | 2.8 | 3.5 | 4.3 | 0.1 | 0.9 | 3.6 | 5.1 | 7.2 | 0.1 | 0.9 | 4.3 | 6.9 | 12.4 |
| | 5.0 | 0.2 | 1.7 | 4.1 | 4.8 | 5.4 | 0.2 | 1.8 | 5.8 | 7.3 | 9.1 | 0.2 | 1.9 | 7.4 | 10.7 | 15.6 |

**Indirect Brine (R245fa) - Pumped**

Power Output per Production-Injection Pair [MWe]

| Temp Gradient [°C km⁻¹] | Depth [km] | 0.27m Inj & Prod Diameter | | | | | 0.33m Inj & Prod Diameter | | | | | 0.41m Inj & Prod Diameter | | | | |
|---|---|---|---|---|---|---|---|---|---|---|---|---|---|---|---|---|
| | | 1x10⁻¹⁵ m² | 1x10⁻¹⁴ m² | 5x10⁻¹⁴ m² | 1x10⁻¹³ m² | 1x10⁻¹² m² | 1x10⁻¹⁵ m² | 1x10⁻¹⁴ m² | 5x10⁻¹⁴ m² | 1x10⁻¹³ m² | 1x10⁻¹² m² | 1x10⁻¹⁵ m² | 1x10⁻¹⁴ m² | 5x10⁻¹⁴ m² | 1x10⁻¹³ m² | 1x10⁻¹² m² |
| 20 | 1.0 | 0.0 | 0.0 | 0.0 | 0.0 | 0.0 | 0.0 | 0.0 | 0.0 | 0.0 | 0.0 | 0.0 | 0.0 | 0.0 | 0.0 | 0.0 |
| | 1.5 | 0.0 | 0.0 | 0.0 | 0.0 | 0.0 | 0.0 | 0.0 | 0.0 | 0.0 | 0.0 | 0.0 | 0.0 | 0.0 | 0.0 | 0.0 |
| | 2.5 | 0.0 | 0.0 | 0.0 | 0.0 | 0.0 | 0.0 | 0.0 | 0.0 | 0.0 | 0.0 | 0.0 | 0.0 | 0.0 | 0.0 | 0.0 |
| | 3.5 | 0.0 | 0.0 | 0.0 | 0.1 | 0.2 | 0.0 | 0.0 | 0.0 | 0.1 | 0.2 | 0.0 | 0.0 | 0.0 | 0.1 | 0.2 |
| | 5.0 | 0.0 | 0.1 | 0.4 | 0.5 | 0.8 | 0.0 | 0.1 | 0.4 | 0.7 | 1.3 | 0.0 | 0.1 | 0.4 | 0.8 | 2.1 |
| 35 | 1.0 | 0.0 | 0.0 | 0.0 | 0.0 | 0.0 | 0.0 | 0.0 | 0.0 | 0.0 | 0.0 | 0.0 | 0.0 | 0.0 | 0.0 | 0.0 |
| | 1.5 | 0.0 | 0.0 | 0.0 | 0.0 | 0.0 | 0.0 | 0.0 | 0.0 | 0.0 | 0.1 | 0.0 | 0.0 | 0.0 | 0.0 | 0.1 |
| | 2.5 | 0.0 | 0.0 | 0.2 | 0.3 | 0.6 | 0.0 | 0.0 | **0.2** | 0.4 | 0.9 | 0.0 | 0.0 | **0.2** | 0.4 | 1.5 |
| | 3.5 | 0.0 | 0.3 | 1.1 | 1.5 | 2.1 | 0.0 | 0.3 | 1.4 | 2.1 | 3.5 | 0.0 | 0.3 | 1.5 | 2.6 | 5.9 |
| | 5.0 | 0.1 | 1.1 | 3.2 | 3.8 | 4.5 | 0.1 | 1.2 | 4.2 | 5.6 | 7.6 | 0.1 | 1.2 | 5.1 | 7.9 | 13.0 |
| 50 | 1.0 | 0.0 | 0.0 | 0.0 | 0.0 | 0.0 | 0.0 | 0.0 | 0.0 | 0.0 | 0.0 | 0.0 | 0.0 | 0.0 | 0.0 | 0.1 |
| | 1.5 | 0.0 | 0.0 | 0.1 | 0.1 | 0.4 | 0.0 | 0.0 | 0.1 | 0.1 | 0.6 | 0.0 | 0.0 | 0.1 | 0.1 | 0.8 |
| | 2.5 | 0.0 | 0.4 | 1.4 | 1.9 | 2.7 | 0.0 | 0.4 | 1.6 | 2.5 | 4.4 | 0.0 | 0.4 | 1.7 | 3.1 | 7.4 |
| | 3.5 | 0.1 | 1.1 | 3.5 | 4.4 | 5.4 | 0.1 | 1.2 | 4.5 | 6.3 | 8.9 | 0.1 | 1.2 | 5.3 | 8.6 | 15.3 |
| | 5.0 | 0.1 | 1.5 | 3.5 | 4.1 | 4.6 | 0.1 | 1.5 | 4.9 | 6.2 | 7.7 | 0.1 | 1.6 | 6.3 | 9.1 | 13.3 |

**Indirect $CO_2$ ($CO_2$) - Thermosiphon**

Power Output per Production-Injection Pair [MWe]

| Temp Gradient [°C km⁻¹] | Depth [km] | 0.27m Inj & Prod Diameter | | | | | 0.33m Inj & Prod Diameter | | | | | 0.41m Inj & Prod Diameter | | | | |
|---|---|---|---|---|---|---|---|---|---|---|---|---|---|---|---|---|
| | | 1x10⁻¹⁵ m² | 1x10⁻¹⁴ m² | 5x10⁻¹⁴ m² | 1x10⁻¹³ m² | 1x10⁻¹² m² | 1x10⁻¹⁵ m² | 1x10⁻¹⁴ m² | 5x10⁻¹⁴ m² | 1x10⁻¹³ m² | 1x10⁻¹² m² | 1x10⁻¹⁵ m² | 1x10⁻¹⁴ m² | 5x10⁻¹⁴ m² | 1x10⁻¹³ m² | 1x10⁻¹² m² |
| 20 | 1.0 | 0.0 | 0.0 | 0.0 | 0.0 | 0.0 | 0.0 | 0.0 | 0.0 | 0.0 | 0.0 | 0.0 | 0.0 | 0.0 | 0.0 | 0.0 |
| | 1.5 | 0.0 | 0.0 | 0.0 | 0.0 | 0.0 | 0.0 | 0.0 | 0.0 | 0.0 | 0.0 | 0.0 | 0.0 | 0.0 | 0.0 | 0.0 |
| | 2.5 | 0.0 | 0.0 | 0.0 | 0.0 | 0.0 | 0.0 | 0.0 | 0.0 | 0.0 | 0.0 | 0.0 | 0.0 | 0.0 | 0.0 | 0.0 |
| | 3.5 | 0.0 | 0.0 | 0.0 | 0.0 | 0.0 | 0.0 | 0.0 | 0.0 | 0.0 | 0.0 | 0.0 | 0.0 | 0.0 | 0.0 | 0.0 |
| | 5.0 | 0.0 | 0.1 | 0.1 | 0.1 | 0.1 | 0.0 | 0.1 | 0.1 | 0.2 | 0.2 | 0.0 | 0.1 | 0.2 | 0.3 | 0.3 |
| 35 | 1.0 | 0.0 | 0.0 | 0.0 | 0.0 | 0.0 | 0.0 | 0.0 | 0.0 | 0.0 | 0.0 | 0.0 | 0.0 | 0.0 | 0.0 | 0.0 |
| | 1.5 | 0.0 | 0.0 | 0.0 | 0.0 | 0.0 | 0.0 | 0.0 | 0.0 | 0.0 | 0.0 | 0.0 | 0.0 | 0.0 | 0.0 | 0.0 |
| | 2.5 | 0.0 | 0.1 | 0.1 | 0.1 | 0.1 | 0.0 | 0.1 | **0.2** | 0.2 | 0.2 | 0.0 | 0.1 | **0.3** | 0.4 | 0.4 |
| | 3.5 | 0.0 | 0.4 | 0.7 | 0.7 | 0.7 | 0.0 | 0.5 | 1.0 | 1.1 | 1.2 | 0.0 | 0.6 | 1.6 | 1.9 | 2.2 |
| | 5.0 | 0.0 | 1.4 | 2.0 | 2.0 | 2.1 | 0.0 | 1.8 | 3.1 | 3.4 | 3.6 | 0.0 | 2.2 | 5.0 | 5.6 | 6.3 |
| 50 | 1.0 | 0.0 | 0.0 | 0.0 | 0.0 | 0.0 | 0.0 | 0.0 | 0.0 | 0.0 | 0.0 | 0.0 | 0.0 | 0.0 | 0.0 | 0.0 |
| | 1.5 | 0.0 | 0.1 | 0.1 | 0.1 | 0.1 | 0.0 | 0.1 | 0.2 | 0.2 | 0.2 | 0.0 | 0.1 | 0.3 | 0.3 | 0.3 |
| | 2.5 | 0.0 | 0.7 | 1.1 | 1.1 | 1.2 | 0.0 | 0.8 | 1.7 | 1.9 | 2.0 | 0.1 | 0.8 | 2.5 | 3.0 | 3.6 |
| | 3.5 | 0.0 | 1.7 | 2.6 | 2.7 | 2.8 | 0.0 | 2.1 | 4.0 | 4.4 | 4.7 | 0.0 | 2.4 | 6.2 | 7.2 | 8.4 |
| | 5.0 | 0.0 | 4.2 | 5.6 | 5.8 | 6.0 | 0.0 | 5.6 | 9.0 | 9.5 | 10.0 | 0.0 | 6.8 | 14.4 | 15.9 | 17.7 |

**Indirect $CO_2$ (R245fa) - Thermosiphon**

Power Output per Production-Injection Pair [MWe]

| Temp Gradient [°C km⁻¹] | Depth [km] | 0.27m Inj & Prod Diameter | | | | | 0.33m Inj & Prod Diameter | | | | | 0.41m Inj & Prod Diameter | | | | |
|---|---|---|---|---|---|---|---|---|---|---|---|---|---|---|---|---|
| | | 1x10⁻¹⁵ m² | 1x10⁻¹⁴ m² | 5x10⁻¹⁴ m² | 1x10⁻¹³ m² | 1x10⁻¹² m² | 1x10⁻¹⁵ m² | 1x10⁻¹⁴ m² | 5x10⁻¹⁴ m² | 1x10⁻¹³ m² | 1x10⁻¹² m² | 1x10⁻¹⁵ m² | 1x10⁻¹⁴ m² | 5x10⁻¹⁴ m² | 1x10⁻¹³ m² | 1x10⁻¹² m² |
| 20 | 1.0 | 0.0 | 0.0 | 0.0 | 0.0 | 0.0 | 0.0 | 0.0 | 0.0 | 0.0 | 0.0 | 0.0 | 0.0 | 0.0 | 0.0 | 0.0 |
| | 1.5 | 0.0 | 0.0 | 0.0 | 0.0 | 0.0 | 0.0 | 0.0 | 0.0 | 0.0 | 0.0 | 0.0 | 0.0 | 0.0 | 0.0 | 0.0 |
| | 2.5 | 0.0 | 0.0 | 0.0 | 0.0 | 0.0 | 0.0 | 0.0 | 0.0 | 0.0 | 0.0 | 0.0 | 0.0 | 0.0 | 0.0 | 0.0 |
| | 3.5 | 0.0 | 0.0 | 0.0 | 0.0 | 0.0 | 0.0 | 0.0 | 0.0 | 0.0 | 0.0 | 0.0 | 0.0 | 0.0 | 0.0 | 0.0 |
| | 5.0 | 0.0 | 0.0 | 0.1 | 0.1 | 0.1 | 0.0 | 0.0 | 0.1 | 0.1 | 0.1 | 0.0 | 0.0 | 0.1 | 0.2 | 0.2 |
| 35 | 1.0 | 0.0 | 0.0 | 0.0 | 0.0 | 0.0 | 0.0 | 0.0 | 0.0 | 0.0 | 0.0 | 0.0 | 0.0 | 0.0 | 0.0 | 0.0 |
| | 1.5 | 0.0 | 0.0 | 0.0 | 0.0 | 0.0 | 0.0 | 0.0 | 0.0 | 0.0 | 0.0 | 0.0 | 0.0 | 0.0 | 0.0 | 0.0 |
| | 2.5 | 0.0 | 0.0 | 0.1 | 0.1 | 0.1 | 0.0 | 0.1 | **0.1** | 0.2 | 0.2 | 0.0 | 0.1 | **0.2** | 0.3 | 0.3 |
| | 3.5 | 0.0 | 0.2 | 0.4 | 0.4 | 0.5 | 0.0 | 0.3 | 0.6 | 0.7 | 0.8 | 0.0 | 0.3 | 1.0 | 1.1 | 1.3 |
| | 5.0 | 0.2 | 1.0 | 1.4 | 1.4 | 1.4 | 0.2 | 1.2 | 2.2 | 2.3 | 2.5 | 0.2 | 1.5 | 3.4 | 3.9 | 4.4 |
| 50 | 1.0 | 0.0 | 0.0 | 0.0 | 0.0 | 0.0 | 0.0 | 0.0 | 0.0 | 0.0 | 0.0 | 0.0 | 0.0 | 0.0 | 0.0 | 0.0 |
| | 1.5 | 0.0 | 0.0 | 0.1 | 0.1 | 0.1 | 0.0 | 0.0 | 0.1 | 0.1 | 0.1 | 0.0 | 0.0 | 0.1 | 0.1 | 0.2 |
| | 2.5 | 0.0 | 0.3 | 0.6 | 0.6 | 0.6 | 0.0 | 0.4 | 0.9 | 1.0 | 1.1 | 0.0 | 0.4 | 1.3 | 1.6 | 1.9 |
| | 3.5 | 0.2 | 1.1 | 1.7 | 1.7 | 1.8 | 0.2 | 1.4 | 2.6 | 2.8 | 3.1 | 0.2 | 1.5 | 4.0 | 4.7 | 5.4 |
| | 5.0 | 1.1 | 5.9 | 7.9 | 8.2 | 8.5 | 1.1 | 7.9 | 12.8 | 13.5 | 14.3 | 1.1 | 9.6 | 20.4 | 22.6 | 25.0 |

**Figure 3.17: Net Electric Power Production per Injection-Production Well Pair for all Six Surface Plant Configurations.** These plots show all six surface plant configurations, unlike Figure 5 I the main paper, which only displays values for the Direct $CO_2$-Pumped and the Indirect (always pumped) Brine (with R245fa as secondary working fluid) system. The net power values are color coded to show low (red), moderate (yellow), and substantial (green) electrical production. The values shown are for a single injection-production pair and must be multiplied by four to obtain the value for the entire inverted 5-spot. The two boxed values in each plot bound the base-case (0.41m injection and 0.27m production well inner diameters).

### 3.8.6 Electric Power and Mass Flowrate Data

The calculated electric power and mass flowrate values are attached to this supplemental information in the form of an EXCEL (*.xlsx) file. The information can be filtered by any of the input parameters. Column labels correspond the Figures 3.3 or 3.4. A value of zero in either the Net Power or Mass Flowrate column indicates that either the model was not able to solve for the given set of parameters, or the model did solve it but did not yield a positive net power for any mass flowrate.

### 3.8.7 Nomenclature

Nomenclature for this supplemental information (Section 3.8) is provided in Table 3.5.

**Table 3.5: Nomenclature.**

| | |
|---|---|
| $a…e$ | Fit coefficients |
| $N$ | Number of samples [-] |
| $P_{CO2}$ | Pressure of $CO_2$ [kPa] |
| $P_{cooler}$ | Power required for Cooler [$kW_e$] |
| $P_{condenser}$ | Power required for Condenser [$kW_e$] |
| $Q$ | Heat Energy Transfer Rate [$kW_{th}$] |
| $S$ | Average Specific Kinematic Viscosity [$m\ s^{-1}$] |
| $SE_S$ | Standard Error in prediction of $S$ [$m\ s^{-1}$] |
| $t$ | Student's-t Value [-] |
| $T$ | Temperature [°C] |
| $T_{app}$ | Approach Temperature Differential [°C] |
| $T_r$ | Tower Range [°C] |
| $T_{wb}$ | Ambient Wet Bulb Temperature [°C] |
| $U_S$ | Uncertainty in regression of S [$m\ s^{-1}$] |
| $\lambda$ | Parasitic Loss Fraction [$kW_e\ kW_{th}^{-1}$] |

Chapter 4

# Electricity with Time

## Preface

The electrical power production of a CPG system was found in Chapter 3 for a large parameter space of well diameter, permeability, depth, and temperature gradient. However, the simulations were for a reservoir with non-depleting temperature production and ideal pressure difference. In reality, a CPG system will be established on a reservoir initially filled with brine and with finite thermal energy.

In this paper, the CPG power production from a more realistic radially symmetric reservoir is simulated for 50 years. The reservoir is initially filled with brine and then injected with $CO_2$ to establish a sufficiently high $CO_2$ mass fraction at the production well. In addition to the parameters used in Adams et al. (2015) of well diameter, permeability, depth, and temperature gradient, two reservoir thicknesses of 50 and 300 m are simulated, as well as two reservoir radii of 300 and 707 m. Thus, for a given reservoir, a CPG developer may use these results to make appropriate well diameter and placement decisions.

## Citation

Adams, B.M., Kuehn, T.H., Bielicki, J.M., Garapati, N., & Saar, M.O. (In preparation). A characterization of temperature depletion in sedimentary basins and its effect on the electric power output of $CO_2$ Plume Geothermal (CPG) power systems. *Geothermics.*

# A Characterization of Temperature Depletion in a Sedimentary Basin and its Effect on the Electric Power Output of $CO_2$ Plume Geothermal (CPG) Power Systems

**Benjamin M. Adams[a], Thomas H. Kuehn[a]*, Jeffrey M. Bielicki[b,c], Nagasree Garapati[d], Martin O. Saar[d,e]**

kuehn001@umn.edu

[a]Department of Mechanical Engineering, University of Minnesota, 111 Church St SE, Minneapolis, MN 55455, U.S.A.

[b]Department of Civil, Environmental, and Geodetic Engineering, The Ohio State University, 2070 Neil Ave, Columbus, OH 43210, U.S.A.

[c]John Glenn School of Public Affairs, The Ohio State University, 1810 College Road, Columbus, OH 43210, U.S.A.

[d]Department of Earth Sciences, University of Minnesota, 310 Pillsbury Drive SE, Minneapolis, MN 55455, U.S.A.

[e]Department of Earth Sciences, ETH-Zürich, Sonneggstrasse 5, 8092 Zürich, Switzerland

**Keywords**

Carbon Dioxide; Geothermal Energy; CCUS; Heat Depletion; Sedimentary Basin Geothermal

**Highlights**

- The thermal decay and pressure differential of a sedimentary basin is characterized.
- Correctly sized well spacing will provide the greatest average power over time.
- Over-estimating the spacing impacts the average power less than under-estimation.
- Correctly sized well spacing is more important with decreased permeability.
- Reducing the well diameter regulates heat extraction and may increase capacity factor.

## Paper Summary

$CO_2$ Plume Geothermal energy systems extract crustal energy from naturally permeable sedimentary basins by circulating sequestered $CO_2$. CPG systems have been shown to perform better than brine in moderate temperature and permeability environments; however, to date, the time-dependent electrical generation has not been found, and thus we simulate this here. We find that for a given reservoir, there is an optimum production and injection well spacing which will provide the most power over the reservoir lifetime; reservoirs with closely spaced wells have lower resistance to flow but deplete quickly, while reservoirs with large well spacing maintain their temperature over time but inhibit the density-driven thermosiphon flow.

## 4.1 Introduction

Global $CO_2$ emissions must be reduced by 78% to 114% by 2100 to maintain the earth's surface temperature within 2 °C of pre-industrial levels so as to avoid serious environmental consequences (IPCC, 2014). Without lifestyle, behavioral, and structural changes, a reduction in $CO_2$ emissions must come from industrial sources, such as power generation, which accounts for one-third of U.S. $CO_2$ emissions (Princiotta & Loughlin, 2014; U.S. President, 2013). To meet this reduction goal, several strategies have been identified, including: technological improvements to generation efficiency, the use of low-carbon fossil resources (e.g. natural gas instead of coal), demand-side conservation programs, and $CO_2$ sequestration. While the intermediate plan to decrease $CO_2$ emissions by 30% by 2030 in the United States does not include sequestration (EPA, 2014), it is very likely that most fossil electrical generation will require carbon capture and sequestration into deep saline reservoirs to meet the long term $CO_2$ emissions goal (Azar et al., 2006; Global CCS Institute, 2014).

Instead of just landfilling the $CO_2$ into a sedimentary basin, it can be circulated back to the surface to generate geothermal power through the use of so-called $CO_2$ Plume Geothermal (CPG). Unlike traditional brine-based geothermal systems, the use of $CO_2$

has many advantages, such as: reduced frictional losses through the reservoir due to increased mobility ($\rho/\mu$), and a density-driven induced flowrate, or thermosiphon, which eliminates the need for submersible pumps (Atrens et al., 2009; Carroll and Stillman, 2014; Adams et al., 2014). Additionally, sedimentary basins are naturally permeable, unlike the shallow, fracture-based networks that are prevalent in traditional brine systems, reducing the need for environmentally controversial hydraulic fracturing. The high mobility of geologic $CO_2$ enables electric power production from reservoirs of lower temperature and permeability than those required for traditional brine-based systems (Adams et al., 2015). Thus, CPG systems tend to more readily and effectively convert geothermal heat into electricity than brine systems.

In the United States, it is estimated that approximately 200,000 exajoules of extractable thermal energy is available in the earth's crust (MIT, 2006); however, technological developments are needed to economically extract and utilize this energy. In 2012, electrical production accounted for 2020 Mt of $CO_2$ emitted in the U.S. or 37% of the total $CO_2$ emissions (EPA, 2012). In a reservoir of moderate temperature and permeability (i.e. a reservoir 2.5 km deep with a permeability of 5 $x10^{-14}$ $m^2$ and a geologic temperature gradient of 35 °C $km^{-1}$), 8 Mt $CO_2$ can enable the generation of 3 MWe (Adams et al., 2015). Therefore, conservatively assuming only 10% of the annual 2020 Mt were sequestered at comparable CPG-enabled sites, 75 MWe of carbon-free electricity would be brought online annually from geothermal resources not otherwise obtainable. This would be an annual increase of 2% from the current 3.4 GWe of installed geothermal power production capacity (NREL, 2014), or 0.015% of total U.S. generation (EIA, 2015).

While research into brine-based geothermal systems is relatively extensive, $CO_2$ was only recently proposed as a subsurface working fluid (Brown, 2000; Pruess, 2006). Initially, $CO_2$ was considered only for Enhanced Geothermal Systems (EGS), where impermeable basement rock is fractured to create flow paths for the injected $CO_2$ (Atrens et al., 2009, 2010; Beckers et al., 2014). Beckers et al. (2014) provided perhaps the most varied EGS

simulations, using the MIT-EGS model, and provided capital costs and LCOE. Unfortunately, their selection of small pipe diameter and mass flowrate yielded high LCOE (>>\$100 $MW^{-1}$ $hr^{-1}$), in agreement with Atrens et al. (2011).

Unlike EGS, $CO_2$ Plume Geothermal (CPG) utilizes sedimentary aquifers overlain with an impermeable caprock. Sedimentary reservoirs have several advantages over fracture-based reservoirs. They are common, naturally permeable formations that are found under approximately half of the United States (Coleman & Cahan, 2012). The relatively homogenous nature of sedimentary basins, when compared to EGS, provides a large surface area in contact with the flowing $CO_2$, allowing for effective transfer of heat. Additionally, they are already a target of current Carbon Capture and Sequestration efforts—sequestration into several such basins has already begun (Global CCS Institute, 2014).

Research into $CO_2$ Plume Geothermal (CPG) has been limited in scope as geologic modeling tends to be performed separately from surface plant modeling. Randolph and Saar (2011a; 2011b) initially estimated power production using a simple Carnot-based surface plant model, focusing primarily on the reservoir dynamics of an inverted 5-spot well pattern filled with pure $CO_2$. Recently, Nagasree et al. (2014a; 2014b) more realistically simulated brine displacement and heat extraction from a comparable, improved 2D radially-symmetric reservoir. Conversely, Janke and Kuehn (2011) simulated the power production of the surface plant for varying atmospheric temperatures and turbine efficiencies, but used fixed values of reservoir temperature, flowrate, and pressure differential. Adams et al. (2014) coupled the reservoir and wells, and showed the mass flowrate of the thermosiphon established. Only recently have coupled reservoir, well, and surface plant models been used to calculate CPG power production (Adams et al., 2015; Pan et al., 2015). Pan et al. (2015) analyzed few parameters, typically a 3 km deep reservoir with a temperature of 152 °C and a permeability of $10^{-13}$ $m^2$, using either 0.1 or 0.18 m diameter piping. However, Adams et al. (2015) analyzed a large parameter space of 945 parameter combinations, including: four well diameters from 0.14 to 0.41

m, five reservoir depths from 1 to 5 km, three geologic temperature gradients from 20 to 50 °C $km^{-1}$, seven permeabilities from $10^{-15}$ to $10^{-12}$ $m^2$, and a total of six types of surface plants for brine and $CO_2$-based systems.

Thus far, no CPG research using a coupled reservoir and surface plant model has simulated power production as the reservoir depletes. Beckers et al. (2014) did account for thermal depletion in an EGS reservoir; however they utilized a fixed-percentage thermal drawdown model instead of simulating the actual reservoir. For $CO_2$, thermal depletion of sedimentary basins has been simulated for the reservoir only (Eliott et al., 2013; Randolph and Saar, 2011a; Garapati et al., 2014a); however, to do so, a heat extraction rate was fixed. As the $CO_2$ mass flowrate through a system and heat extraction rate are inseparably linked (Adams et al., 2014), only a simulator with combined reservoir, well, and surface plant models can accurately predict the time-dependent power production.

In this paper, we compute the time-dependent power production of a CPG power system as the production temperature of the sedimentary basin decreases with time. The net power values are found for the full range of expected reservoir and system parameters, overlapping with previously used values (Adams, et al., 2015). A detailed list of these parameters is provided in Table 4.1. The reservoir is modeled as a truncated cylinder with a cap rock above, fluid injected at the center (vertical axis of the cylinder), and the fluid extracted at a specified radius from the center under the cap rock similar to the configuration used by Nagasree et al. (2014a; 2014b).

**Table 4.1: Model parameters**

| | |
|---|---|
| Well Diameter | 0.14 m, 0.27 m, 0.33 m, and/or 0.41 m |
| | |
| *Reservoir Conditions* | |
| Depth | 1.5 km, 2.5 km, 3.5 km, or 5.0 km |
| Thickness | 50 m or 300 m |
| Radius | 300 m or 707 m |
| Geothermal Gradient | 20 °C $km^{-1}$, 35 °C $km^{-1}$, or 50 °C $km^{-1}$ |
| Permeability | $1x10^{-12}$ $m^2$ to $1x10^{-15}$ $m^2$ |

This paper differs from earlier work, such as Adams et al. (2014) which considered only initial power output, by considering the time-dependent thermal decay of the reservoir, as well as adding two new parameters: reservoir thickness and radius of the active reservoir, assumed to be a truncated cylinder. Additionally, unlike the inverted 5-spot of Adams et al. (2014) which is assumed to be filled with 100% $CO_2$, the geologic model is improved to use a two component fluid, $CO_2$/NaCl-brine, within the radially symmetric reservoir, which is initially filled only with 20 wt% NaCl brine. A Direct-$CO_2$ CPG system with supplemental pumping is used, identical to that used previously (Adams et al, 2015). To facilitate the simulation of the large number of parameters given in Table 4.1, the time dependent temperature and pressure results of the reservoir were necessarily characterized to reduce computational time.

## 4.2 Methods

Figure 4.1 shows the system being simulated including the radially symmetric reservoir.

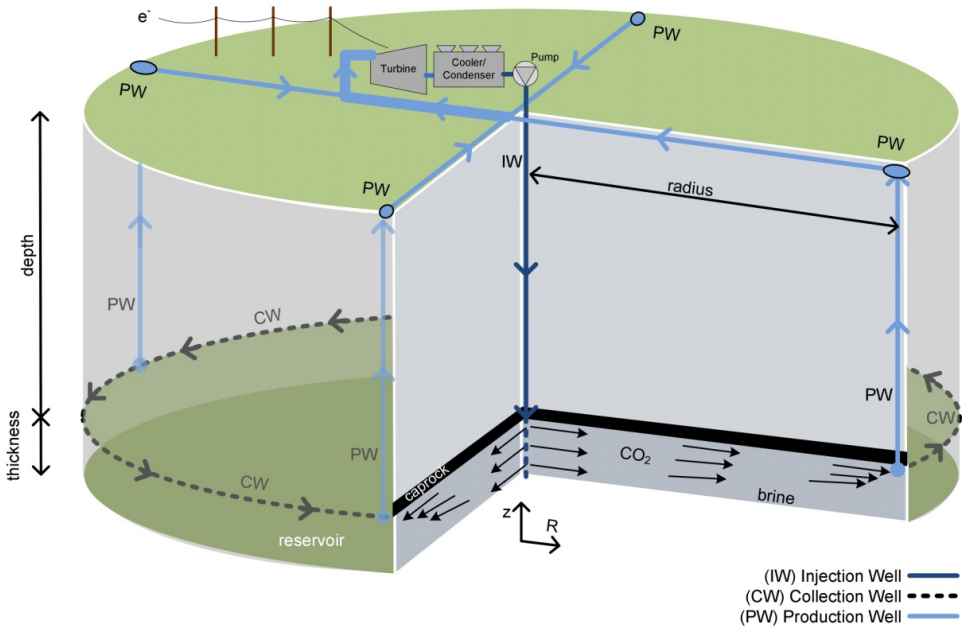


**Figure 4.1: Schematic of a CPG System.**

The cylindrical reservoir has a single, vertical injection well (IW) located at the center, and a continuous, circular collection well (CW) at the perimeter, directly beneath the caprock. The $CO_2$ is produced to the surface through one of four equally spaced vertical production wells (PW) which adjoin the horizontal collection well. Once at the surface, the fluid is run through a turbine and condenser, and then reinjected through the central injection well back into the formation.

The simulation of the CPG system uses two software packages: TOUGH2 for the subsurface simulation, and Engineering Equation Solver (EES), a simultaneous equation solver with built-in thermophysical property data for the surface plant and well piping. Traditionally for brine, the subsurface and surface simulations have been performed separately (e.g. GETEM—DOE (2012)); however, the TOUGH2 and EES simulators need to be coupled, as the mass flowrate, temperature, and pressure at the downhole injection and production points, where the models interface, are interdependent. A .Net code was developed to couple the models; however, the computational time limited the number of simulations that could be reasonably executed. Thus, to reduce computational time, the TOUGH2 simulator results were characterized by the relevant system parameters (i.e. depth, temperature gradient, permeability, radius, and $CO_2$ injection fluid state) into to a set of dimensionless curves, which were then integrated into the EES simulator.

### 4.2.1 Reservoir Modeling

The reservoir is considered to be homogeneous, horizontal, and radially symmetric; initially at uniform temperature and pressure. The reservoir was modeled using TOUGH2 (Pruess, 2004) with the ECO2N and ECO2H equation of state modules (Pruess 2004, 2005; Spycher and Pruess, 2011) with parameters as given in Table 4.2. The initial temperature of the reservoir is the product of the geothermal temperature gradient and reservoir depth plus the average ambient air temperature, taken to be 15 °C. The initial pressure is the hydrostatic head of pure water at the given depth. The injection well is vertical and centrally located (R=0). The grid spacing in the reservoir increases with

radial distance, up to the radial extent of the reservoir, 100 km, to account for brine displacement, thermal expansion, and over-pressurization which occur from $CO_2$ injection (Garapati et al., 2014a; Garapati et al., 2014b). The collection well is horizontal and circular, located directly beneath the impermeable caprock, a radial distance given by the reservoir radius, R. Unreported simulations have shown the pressure loss through the horizontal collection well to be insignificant in comparison to the loss in the vertical production wells, thus the horizontal collection well is assumed to have uniform pressure. Similarly, it was found that a single vertical production well substantially limited power generation due to high frictional losses. Thus, four vertical production wells operating in parallel were considered.

**Table 4.2: TOUGH2 Parameters for Reservoir Characterization**

| | |
|---|---|
| Primary System (Reservoir) Fluid | $CO_2$ injected into 20 wt% NaCl-brine |
| Thickness | 50 to 300 m |
| Radial Extent | 300 to 1200 m |
| Rock Density | 2300 kg $m^{-3}$ |
| Rock Specific Heat | 0.92 kJ $kg^{-1}$ °$C^{-1}$ |
| Rock Thermal Conductivity | 2.1 W $m^{-1}$ °$C^{-1}$ |
| Porosity | 0.10 |
| Permeability | 5 x$10^{-14}$ $m^2$ |
| $CO_2$ Injected (δ = 50 m) | 2 to 6 Mt $CO_2$ (See Garapati et al., In Review) |
| $CO_2$ Injected (δ = 300 m) | 10 Mt $CO_2$ |

The reservoir is initially composed of 20 wt% NaCl-brine and pure $CO_2$ is injected without production, displacing the brine over the course of 2 or 2.5 years, for 300 m and 50 m reservoir thicknesses, respectively, when the production well achieves a minimum 94% mass-fraction of $CO_2$ (Garapati et al., In Review). This minimum required mass fraction was set from operating condition requirements from perspective turbine manufacturers. The injection temperature of $CO_2$ into the reservoir was based on the isentropic compression of saturated liquid $CO_2$ at ambient temperature plus a seven degree approach temperature in the condensing tower (i.e. 22 °C) to the hydrostatic

pressure at the reservoir depth. Thus, the injection temperature is assumed to be 35, 46, 58, and 65 °C for depths of 1.5, 2.5, 3.5, and 5 km, respectively.

To characterize the reservoir, the produced fluid temperature was simulated for $CO_2$ injection mass flowrates of 3 (95.1), 4 (126.8), 5 (158.5), and 6 Mt $yr^{-1}$ (190.2 kg $s^{-1}$), initially ramping linearly from zero to the specified mass flowrate over two years, for a minimum of 50 years. To increase the reliability of the TOUGH2 characterization, Table 4.2 shows the increased number of parameters used instead of those previously specified in Table 4.1. Thus, these simulations were performed for: reservoir thicknesses of 50 and 300 m, radii of 300, 500, 707, 1000, and 1200 m, and depths of 1.5, 2.5, 3.5, and 5.0 km, and geologic thermal gradients of 35 and 50 C $km^{-1}$, although not all combinations of these variables were simulated. A permeability of 5 $x10^{-14}$ $m^2$ was used for all simulations as previous work has shown that pressure change values can be reliably scaled with permeability (Adams, et al., 2015). The resulting 330 datasets were then analyzed.

#### 4.2.1.1 Pressure Differential Characterization

The pressure differential across the reservoir, $\Delta P$, is the pressure in the injection well at the greatest reservoir elevation (just under the cap rock) less the pressure of the circumferential collection well. For each of the 330 datasets, the pressure differential was plotted versus a non-dimensional time quantity, $\tau = t\ \nu\ /\ R^2$, where the kinematic viscosity, $\nu$, was determined using the injection fluid properties. Thus, for a given set of reservoir parameters (e.g. depth, radius, thickness, etc.), $\tau$ is dependent only on time and Figure 4.2 shows the asymptotic approach of reservoir pressure differential with time to a steady-state value, $\Delta P_0$. The first two years of data were omitted because they had a non-steady injection mass flowrate. A power fit was used of the form $\Delta P = \Delta P_0\ a\ \tau^b + \Delta P_0$, and 330 values of $\Delta P_0$, a, and b were obtained, one for each data set.

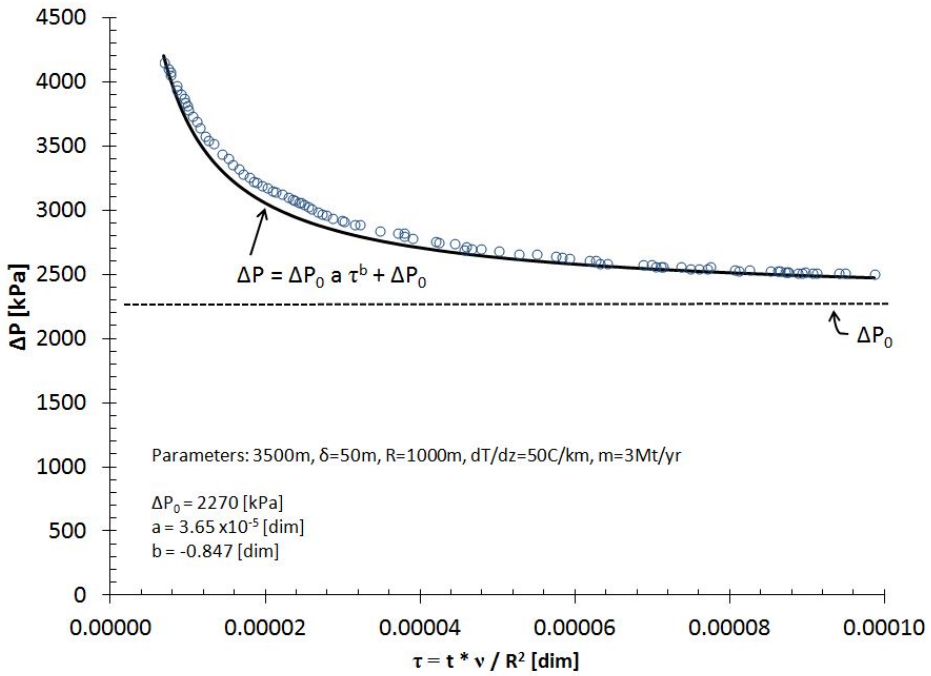


**Figure 4.2: Example of Reservoir Pressure Differential, ΔP, versus the Non-Dimensional Time Quantity: $\tau = t * \nu / R^2$ for a 3.5 km Depth Reservoir with a 50 m Thickness, 1000 m Radius, 50 °C km$^{-1}$ Temperature Gradient, and a Mass Flowrate of 3 Mt yr$^{-1}$.** This non-dimensional plot shows the asymptotic approach of the pressure differential with time.

The steady pressure differential, $\Delta P_0$, was characterized in terms of the Darcy equation. In homogeneous reservoirs with laminar flow, the pressure differential can be found using the 1D Darcy Equation,

$$Q = \frac{\kappa A}{\mu}\left(\frac{dP}{dR}\right), \tag{4.1}$$

where Q is the volumetric flowrate and A is the cross-sectional area. When solving for a simple 1D radial flow of thickness δ and substituting $Q = \dot{m}/\rho$, the equation becomes

$$\left(\frac{dP}{dR}\right) = \left(\frac{\dot{m}}{\rho}\right)\frac{\mu}{\kappa(2\pi R\delta)}. \tag{4.2}$$

Integration from the inner radius, $R_0$, to the radius of the collection well, R, yields,

$$\Delta P_{ideal} = \left( \frac{\dot{m}\,\mu}{\rho\,\kappa\,2\pi\,\delta} \right) \left( \ln(R) - \ln(R_0) \right),$$

which simplifies to,

$$\Delta P_{ideal} = \frac{\dot{m}\,\mu \ln(R)}{\rho\,\kappa\,2\pi\,\delta}, \tag{4.3}$$

when the inner diameter, $R_0$, is assumed to be unity. When the fit term $\Delta P_0$ was normalized by $\Delta P_{ideal}$ and plotted versus the ratio of thickness to depth, a linear trend emerged. This trend, shown in Figure 4.3, shows the deviation of the steady pressure differential values, $\Delta P_0$, from the ideal value predicted from the Darcy equation. The Darcy equation under-predicts reservoirs of increasing thickness due to the corresponding increase in un-swept volume.

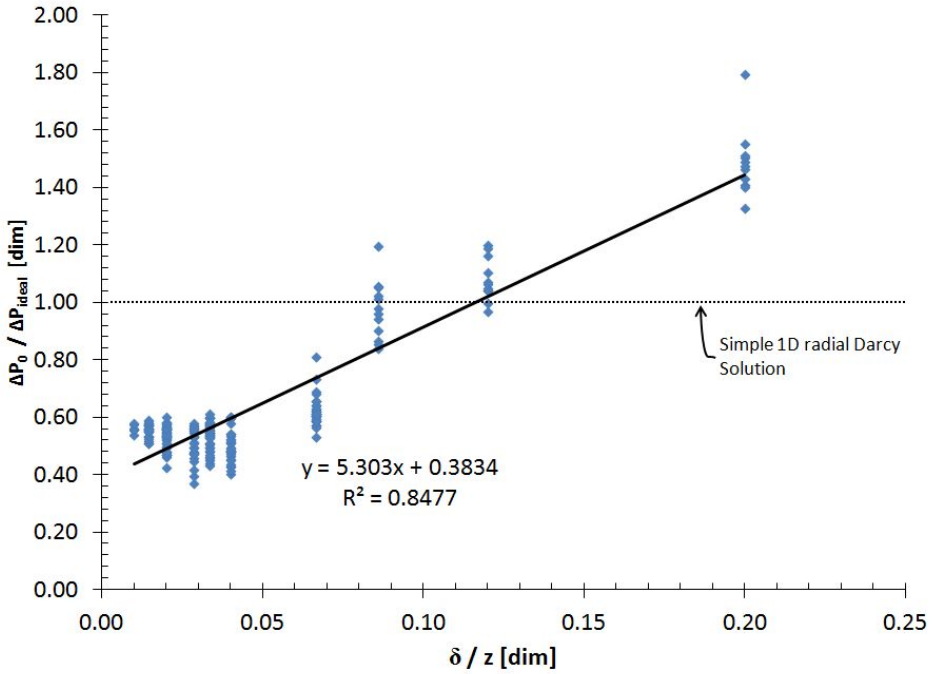


**Figure 4.3: Prediction of Steady Pressure Differential, $\Delta P_0$, from Ratio of Thickness to Depth.** [non-dimensional]

In a similar fashion, *a* and *b* were predicted, shown in Figure 4.4. *b* was best predicted from the ratio of reservoir radius to depth, while *a* was best predicted by *b*. Thus, *a* and *b*

are interdependent, and the entire pressure differential prediction only has two factors, *b* and $\Delta P_0$.

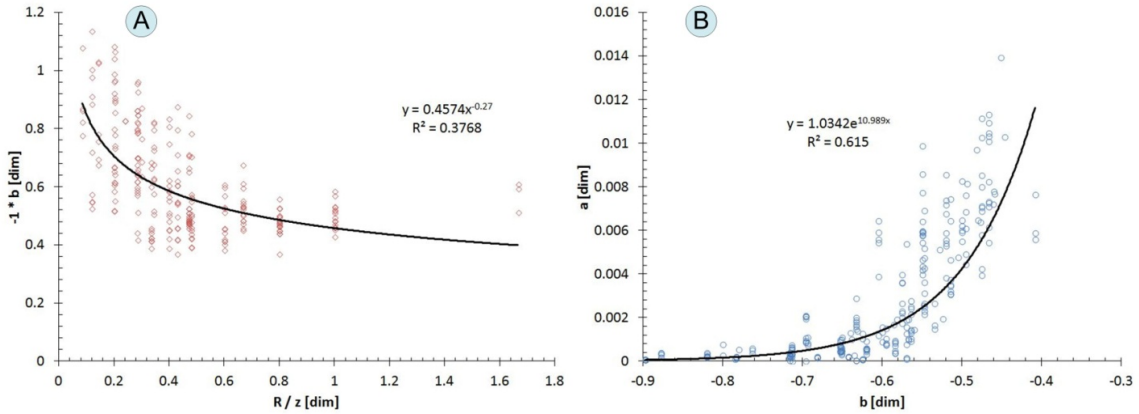


**Figure 4.4: Prediction of Fit Values: A) a, Based on Ratio of Radius to Depth, and B) b, based on a.**

The quality in prediction of ΔP from the following regressions was found from the standard error of estimate,

$$se_{\Delta P} = \sqrt{\frac{\sum \left(\Delta P_{pred} - \Delta P_{actual}\right)^2}{N-2}}, \tag{4.4}$$

where the difference between predicted and actual pressure differential was found for every value in each of the 330 datasets. Then, because the standard error of estimate is the standard deviation of the predicted values from actual, the probability of predicting a value to within 95% of the actual value is the prediction interval, the standard error of estimate multiplied by the two-sided 95% t-value,

$$\Delta P_{95\%} = \pm t_{0.025,N} \cdot se_{\Delta P} = 1.96 \cdot se_{\Delta P}. \tag{4.5}$$

The standard error of estimate and prediction interval were normalized by the actual pressure difference at every point. The resulting standard error of estimate is 15% and the 95% prediction interval is ±30%. These values are large and future work could refine these predictors. The 1D Darcy model here does not consider the complexities of a two-component working fluid, buoyancy effects, or non-uniform flow.

#### 4.2.1.2 Thermal Decay Characterization

The time-dependent temperature of the fluid extracted from each reservoir was characterized using non-dimensional values for each of the 330 datasets. Temperature was non-dimensionalized into the temperature fraction,

$$\Gamma = \frac{\left(T - T_{inj}\right)}{\left(T_{initial} - T_{inj}\right)}, \tag{4.6}$$

where the injection temperature was previously defined, based on $CO_2$ liquid that is compressed isentropically from the surface. The initial temperature is equal to the product of geothermal temperature gradient and depth plus an average surface temperature of 15 °C. The temperature fraction was plotted with respect to the total Joules of energy removed, normalized by the initial Joules of available energy, or "reservoirs of energy extracted," Ψ, defined as

$$\Psi = \frac{\int_0^t \dot{m}\left(h_{prod} - h_{inj}\right)dt}{\pi R^2 \delta \rho_{rock} C_{p,rock}\left(T_{initial} - T_{inj}\right)}. \tag{4.7}$$

Initially, all cases will have an initial temperature fraction of 1. For a simple reservoir without heat conduction from surrounding rock, the temperature fraction would decay in the form of an error function, having a temperature fraction of zero (Γ=0) at one unit of reservoir energy extracted (Ψ=1), similar to that shown for fracture networks (Pruess and Bodvarsson, 1984; Armstead and Tester, 1987). However, the heat conduction from surrounding rock allows more energy to be extracted than is available in the reservoir rock alone (i.e. Ψ>1), and the temperature fraction will decay to a non-zero value for large values of Ψ, shown in Figure 4.5 by variable $p_3$. As the temperature decays and the radial temperature profile becomes uniform, the function will take on an exponential shape, consistent with a first-order thermal decay process. Thus, a combined error function and exponential function was used to characterize the curves, where the transition point is located at a point of 50% decay, shown in Figure 4.5.

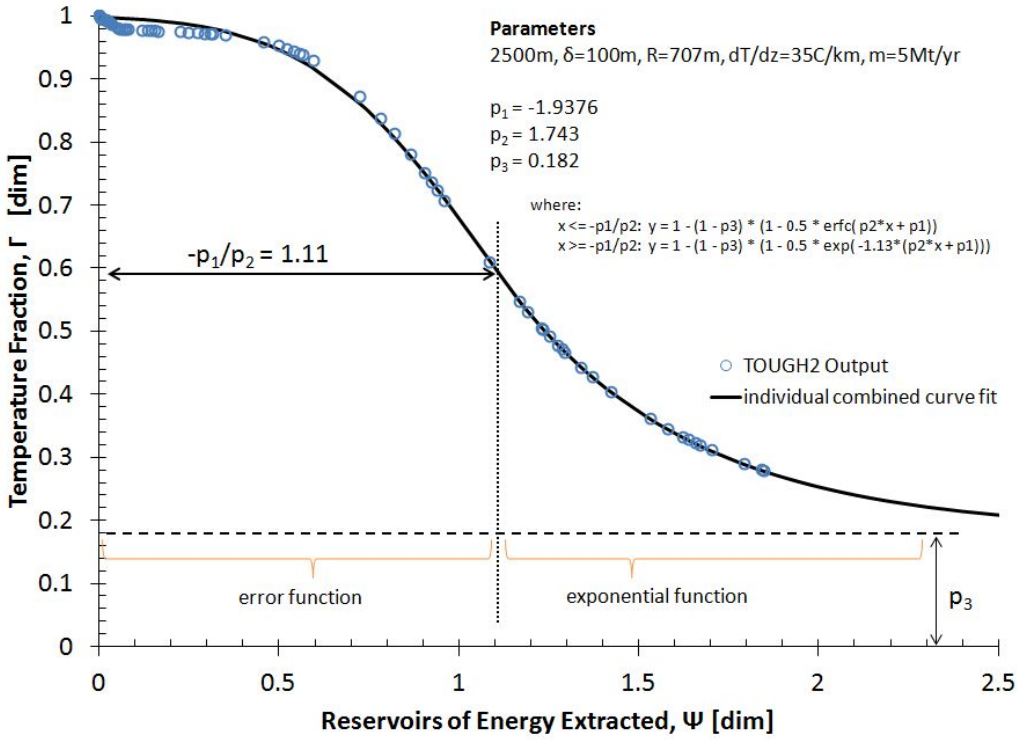


**Figure 4.5: Example Temperature Fraction versus Reservoirs of Energy Extracted for a Single Set of Reservoir Parameters Showing the Fit of a Combined Error Function and Exponential Curve.**

The combined error function and exponential curve was scaled using three values, $p_1$, $p_2$, and $p_3$. The curve was translated and scaled horizontally, using $p_1$ and $p_2$, respectively, while it was horizontally offset from zero using $p_3$, according to Equations 4.8 and 4.9,

$$x <= \left(-\frac{p_1}{p_2}\right) : y = 1 - (1 - p_3)(1 - 0.5\, erfc(p_2\, x + p_1)) \,, \tag{4.8}$$

$$x >= \left(-\frac{p_1}{p_2}\right) : y = 1 - (1 - p_3)(1 - 0.5\, exp(-C(p_2\, x + p_1))), \tag{4.9}$$

where C is a scaling factor to match the function slopes at the interface,

$$C = \frac{d\left(0.5\,erfc(x)\right)}{d\left(0.5\exp(x)\right)}\bigg|_{x=0} = 1.13, \tag{4.10}$$

and a vertical scaling factor of 0.5 was applied to limit the function to a domain of $0 < y < 1$. The results shown in Figure 4.5 indicate the combined function fits individual temperature decay profiles well—the average $r^2$ of all 330 individually fit datasets is 0.989. The small temperature drop that occurs near at the onset of production is attributed to the Joule-Thompson cooling of the $CO_2$ near the collection well as the reservoir is initially depressurized from hydrostatic pressure to the production pressure. Supporting this hypothesis, the temperature decay is larger for smaller depths, where the value $\partial T/\partial P$ is large due to closer proximity to the critical point of $CO_2$ ($P_{crit}$ = 7.4 MPa).

Values of $p_3$, the asymptotic value, are found for all 330 datasets and are shown in Figure 4.6. Many large radius reservoirs, especially those with large thickness and low mass flowrate, did not decay more than 50% to their estimated steady value, $p_3$, which expectedly introduced large errors into the fit and were disregarded, removing approximately 15% of trials.

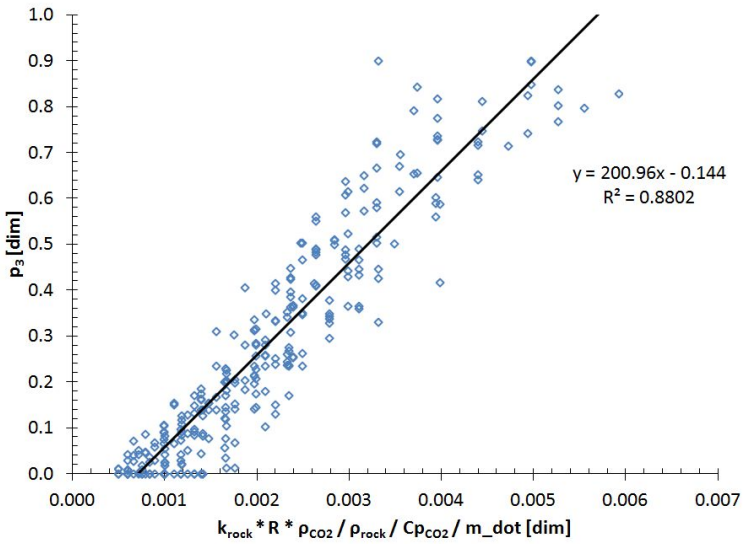


**Figure 4.6: Characterization of $p_3$ Based on Reservoir and Fluid Properties.** [Non-dimensional]

Variable $p_3$ represents the quasi-steady-state temperature fraction where the temperature rise of the injected $CO_2$ is equal to the heat conducted into the reservoir volume from the surrounding rock. As such, $p_3$ was fit with respect to variables which would appear in a conduction-dominated fluid-solid heat transfer solution, such as rock thermal diffusivity, fluid density, specific heat, and mass flowrate. All fluid properties were evaluated at hydrostatic pressure at the injection temperature.

Using a linear estimate of $p_3$, confined to $1 \geq p_3 \geq 0$, all datasets were re-fit, and 330 values of $p_1$ and $p_2$ were obtained. The characterization of these variables is shown in Figure 4.7. Outlier removal on $p_1$ disregarded 12% of the data, mostly those of radius larger than 1 km, which did not decay sufficiently in the simulation time period. The best predictor of $p_1$ was a combination of reservoir parameters, fluid properties, and fluid mass flowrate, while the best predictor for $p_2$ was $p_1$, indicating only two independent factors in the fit for thermal decay, $p_1$ and $p_3$.

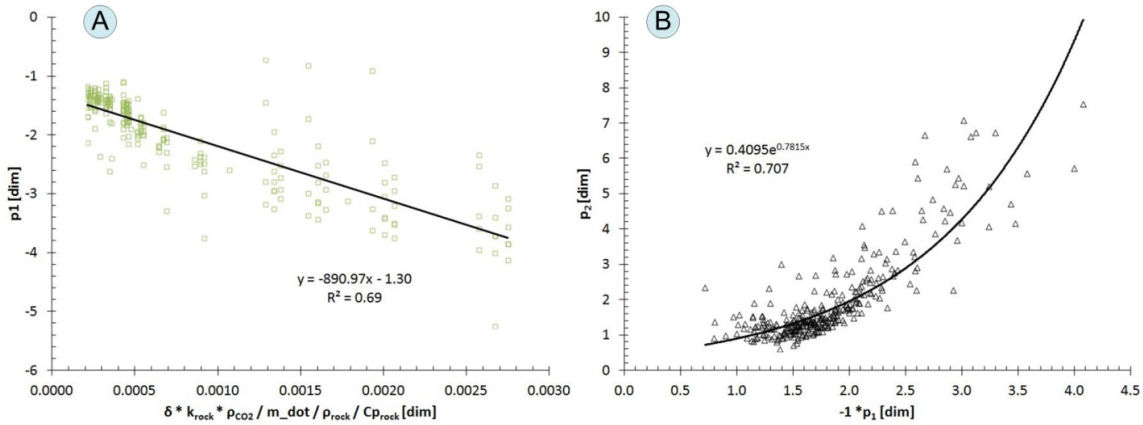


**Figure 4.7: Parameter Fit Curves for A) Variable $p_1$ as a Function of Reservoir and Fluid properties, and B) Variable $p_2$ as a function of $p_1$.**

Of note is the weak dependence on reservoir depth of factors $p_1$, $p_2$, or $p_3$; none of the characterizations take depth into account directly—it is only accounted for in the varying $CO_2$ properties with depth and the increased temperature used to calculate reservoir energy extracted. Note that most reservoirs have a value of $-3 < p_1 < -1$.

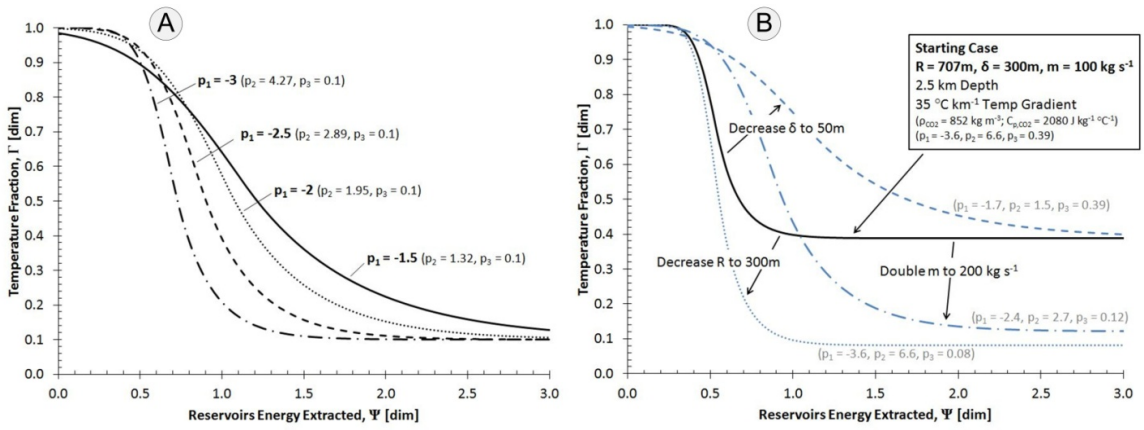


**Figure 4.8: A) Temperature Decay Profiles for Select Values of $p_1$ from -3 to -1.5, and B) Effect of Decreasing Thickness, Decreasing Radius, and Doubling Mass Flowrate on 2.5 km, 35 °C km$^{-1}$ Starting Case.**

Factors $p_1$ and $p_2$ affect the horizontal translation of the decay curve, as shown in Figure 4.8A, for a fixed value of $p_3$ = 0.1, and can be best explained as a correction factor to account for the decrease in swept area and heat conduction from the surrounding rock as the reservoir thickness increases. The reservoirs of energy extracted is the energy extracted divided by total energy contained within the reservoir volume (Equation 4.7), and despite that a 300 m thick reservoir contains more energy than a 50 m thick reservoir, when divided by reservoir volume, it appears to have less access to the available energy (shown by decreasing values of $p_1$ in Figure 4.8A and a corresponding shift for increased thickness in Figure 4.8B). In a similar fashion, Figure 4.8B shows that decreasing the reservoir radius only has the effect of shifting the steady-state temperature to a lower value, and doubling the mass flowrate both increases $p_1$ and decreases $p_3$, although the change in $p_3$ has a greater effect on the decay curve than $p_1$.

Overall, when predicting the temperature fraction using factors $p_1$, $p_2$, and $p_3$, the standard error of estimate, using Equations 4.4 and 4.5, is 0.048, with a 95% prediction interval of ±0.096. This is not unreasonable given the small number of factors used in this zeroeth-order fit; however, future work could improve upon this fit by re-defining the

reservoirs energy extracted (Equation 4.7) to account for the unswept area within the reservoir, especially as its thickness increases.

### 4.2.2 Surface Plant Modeling

The surface plant converts the geothermal heat flux to electrical power. It includes production and injection well piping, a direct-$CO_2$ turbine, cooler, condenser, and a surface injection pump, as shown in Figure 4.9. The system is identical to that used previously (Adams et al., 2014). Engineering Equation Solver (EES) was used to solve for $CO_2$ fluid properties, based on Span and Wagner (1996).

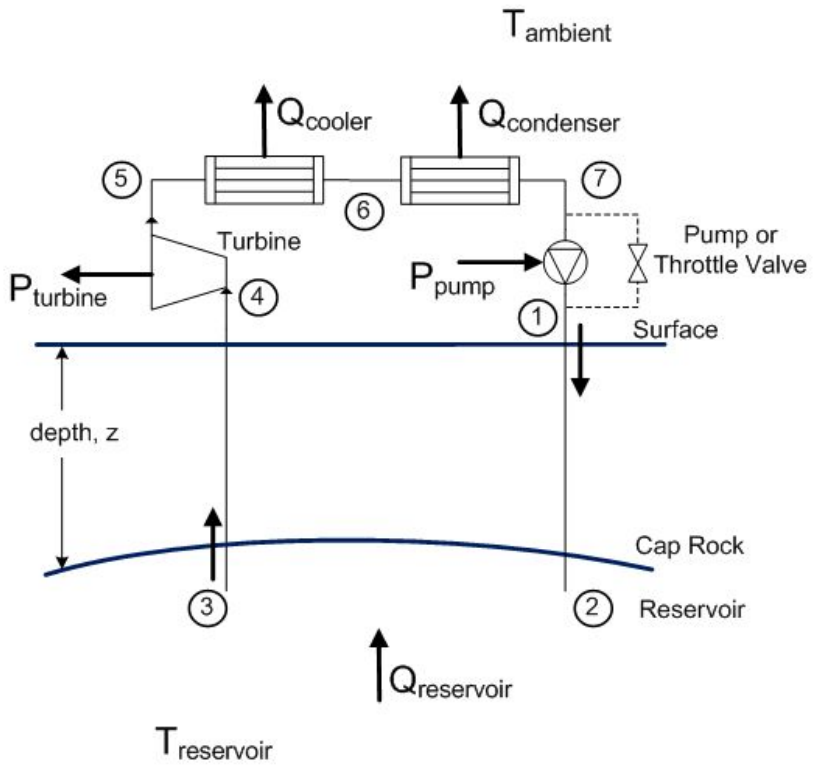


**Figure 4.9: Direct CPG System Schematic (Source: Adams et al., 2015).**

Saturated liquid $CO_2$ at a temperature equal to ambient plus a seven degree approach temperature (State 1) is injected from the surface, where it is compressed nearly isentropically, and is injected at State 2. The $CO_2$ flows through the reservoir, increasing

in temperature and decreasing in pressure an equivalent amount to the pressure differential found in previous sections, to State 3, where the absolute pressure is hydrostatic. The $CO_2$ flows isobarically through the horizontal collection well and up to the surface in the production wells to State 4. The $CO_2$ expands through a turbine with an isentropic efficiency of 78% to State 5. It is isobarically de-superheated in a cooler to State 6, and then isobarically condensed to State 7 at a pressure equivalent to the saturation pressure of $CO_2$ at 22 °C. The $CO_2$ is either pumped or throttled to the requisite pressure at State 1 which will maintain the pressure of State 3 assumed to be hydrostatic for the given reservoir depth, temperature, and permeability.

The CPG system is operated at the mass flowrate that provides the largest net power,

$$P_{net} = P_{turbine} + P_{pump} + P_{cooler} + P_{condenser} \tag{4.11}$$

where the pump, cooler, and condenser powers are parasitic loads, and therefore negative. Power and heat values are the product of the mass flowrate and the $CO_2$ enthalpy difference between entrance and exit of the corresponding component.

For every combination of well diameter, permeability, radius, and thickness, the net power was found in 5 year increments from years 0 to 50. At each time step, the reservoir produced fluid temperature and pressure differential were recalculated using the fits described previously. For those fit parameters using mass flowrate, an average mass flowrate was used, calculated from the previously solved time steps.

## 4.3 Results and Discussion

The net power produced was found for each of the parameter combinations shown in Table 4.1. Figure 4.10 shows the time-series values of A) net power, B) temperature fraction, and C) mass flowrate for a 2.5 km deep, 35 °C $km^{-1}$ temperature gradient, and 5 $x10^{-14}$ $m^2$ reservoir with 0.41 m diameter injection and production wells.

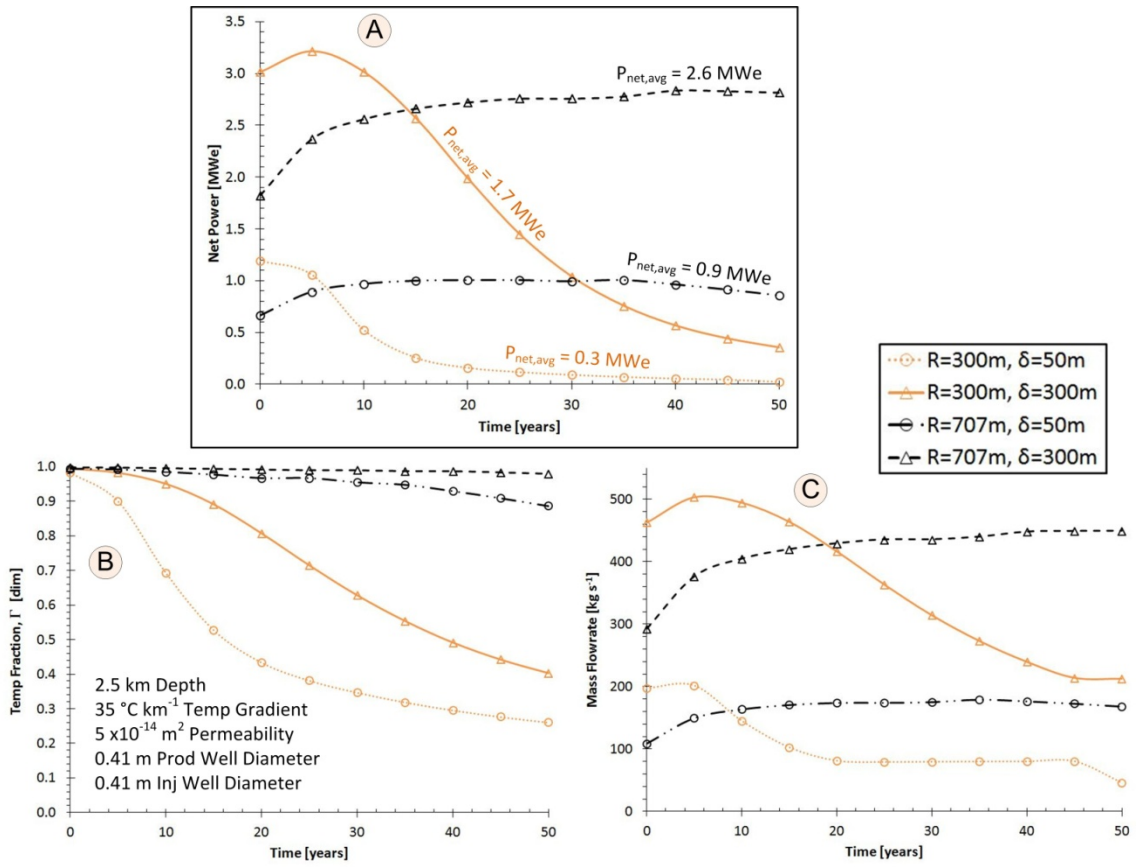


**Figure 4.10: A) Net Power [MWe], B) Temperature Fraction, Γ [dim], and C) Mass Flowrate Versus Time of the Same System for Two Radii and Thicknesses [kg s$^{-1}$]**

In each reservoir case, the maximum mass flowrate (Figure 4.10C) occurs at non-zero values of time. This maximum is created by the interaction of the reservoir pressure differential and production temperature. As the reservoir pressure differential drops with time (Figure 4.2), the overall system frictional losses decrease, more effectively utilizing the pressure differential created by the thermosiphon. At the same time, the reservoir downhole production temperature (Figure 4.10B) decreases with time, which decreases the density differential between injection and production wells, decreasing mass flowrate (Adams et al., 2014). Thus, for systems with rapid thermal drawdown, such as those with the shorter 300 m radius, the decreasing pressure differential is quickly countered by the decreasing production temperature, yielding a maximum mass flowrate at lower values of time. Similarly, the systems with greater radii have a larger thermal mass, therefore the

production temperature decreases more slowly, and the mass flowrate peaks at larger time values.

Figure 4.10A shows that increasing the reservoir thickness always increases the net power production. This is due to the inverse relationship between thickness and pressure differential in the Darcy equation (Equation 4.3): increasing the thickness decreases the pressure difference and thus increases the mass flowrate and net power. Similarly, decreasing the reservoir radius decreases the pressure differential, though this effect is small at large values of radius ($R>>R_0$). However, decreases in reservoir radius, while increasing mass flowrate and instantaneous net power, also decrease the time to thermal breakthrough. Thus, while the 300 m radius reservoirs in Figure 4.10A have a larger maximum power than the 707 m reservoirs, they have lower average power values. Therefore, for any given reservoir thickness, there will be a radius which will provide the maximum average net power over a given time period.

### 4.3.1 Optimal Radius for Reservoir Thickness

For any given reservoir, the optimum radius is the radius which will produce the greatest average power over the lifetime of the reservoir. To more clearly define this optimum radius, additional simulations were run for 50 years of operation for a reservoir depth of 2.5 km, geothermal temperature gradient of 35 °C $km^{-1}$, and permeabilities of 5 $x10^{-15}$ and 5 $x10^{-14}$ $m^2$, with thicknesses of 50, 100, 200, and 300 m. The results are shown in Figure 4.11.

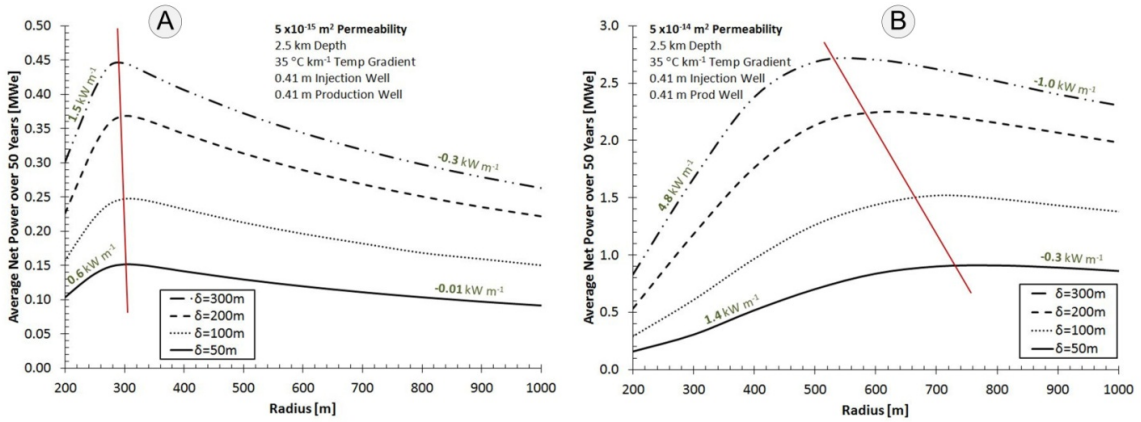


**Figure 4.11: Average Net Power over 50 Years versus Reservoir Radius for 4 Thicknesses at a permeability of A) 5 x10$^{-15}$ m$^2$ and B) 5 x10$^{-14}$ m$^2$ [MWe].** A red line indicates the trend of optimum radius values across thicknesses. The slopes of the power curves, approximated as linear, are provided on each side of the optimum radius for thicknesses of 50 and 300 m.

In all cases, for a given reservoir radius, increasing thickness corresponds to increased power. For each of the thicknesses shown in Figure 4.11, a maximum average net power is obtained within the radius range of 200 to 1000 m. Described previously, the optimum radius occurs due to the interaction between the differential pressure and thermal mass which affect the average net power production in opposing ways as the reservoir radius is decreased. For a permeability of 5 x10$^{-14}$ m$^2$ (Figure 4.11B), the optimum radii are near 500 m and 800 m for reservoir thicknesses of 300 and 50 m, respectively. A red line showing the trend of maximum power across thicknesses is shown with a negative slope, indicating a decreased optimum radius for increasing thickness.

The optimum radius is larger for thinner reservoirs to counter the reduction in thermal mass that would otherwise occur; however, the reservoir volume is not maintained constant—thinner reservoirs require less volume as they have an increased capacity to conduct heat from the surroundings and smaller mass flowrates than an otherwise equivalent, thicker reservoir.

For a permeability of 5 x10$^{-15}$ m$^2$ (Figure 4.11A), a similar line of negative slope indicates the relationship between optimum radius and thickness; however, the line has a

much steeper slope at this low permeability, due, in part, to the relatively low mass flowrates and the sensitivity of mass flowrate to radius.

For a given reservoir thickness, the slope of the power curve, in units of kWe $m^{-1}$ indicates the energy penalty for an incorrect choice of radius. The slopes are shown in Figure 4.11 for 50 and 300 m thicknesses. For example, for a 5 $x10^{-15}$ $m^2$ permeability reservoir (Figure 4.11A) with a thickness of 300 m, 0.3 kWe are lost for every meter of over-sizing; thus the use of a 600 m radius well will decrease power by approximately 90 kWe, or 20% of peak power. All else equal, the magnitude of slope tends to be a factor of 5 larger for small radii than large radii, indicating an oversized reservoir radius will have less impact on the average net power generation over the lifetime of the system than selecting a radius that is too small. However, as permeability decreases, the magnitudes of the slopes increase, indicating that the selection of a correctly sized collection well radius is more important at small permeabilities.

The optimum radius will vary depending on the time period over which the maximum average power is sought. For decreased time periods (such as 30 years instead of 50 years), the thermal energy required to be extracted will decrease, decreasing the necessary reservoir radius. Thus, for decreasing time of interest, the optimum radius also decreases.

### 4.3.2 Average Net Power Variability across the Parameter Space

The average net power production values were found for each parameter in Table 4.1 and a subset are displayed in Figure 4.12 with fixed injection and production well diameters of 0.41 m. Additionally, the full data are available as a supplement (see Section 4.6). The values are colored to indicate low (red), intermediate (yellow), and high (green) values of net power production. As power values were previously found to be negligible for depths less than 3.5 km at a temperature gradient of 20 °C $km^{-1}$ and less than 2.5 km at a temperature gradient of 35 °C $km^{-1}$ (Adams et al., 2015), those values were not simulated and are represented as blank cells. For comparison, the parameter combinations which

had larger CPG power production values than using brine in Adams et al. (2015—see Figure 3.7) are bordered with a dark line. This is shown only for the combinations with 300 m thickness and 707 m radius, which most closely align with the reservoir used in that study.

Average Net Power Produced over 50 Years [MWe]

| Temp Gradient [°C km$^{-1}$] | Depth [km] | Permeability [m$^2$] | 1x10$^{-15}$ | | | | 1x10$^{-14}$ | | | | 5x10$^{-14}$ | | | | 1x10$^{-13}$ | | | | 1x10$^{-12}$ | | | |
|---|---|---|---|---|---|---|---|---|---|---|---|---|---|---|---|---|---|---|---|---|---|---|
| | | Thickness [m] | 50 | | 300 | | 50 | | 300 | | 50 | | 300 | | 50 | | 300 | | 50 | | 300 | |
| | | Radius [m] | 300 | 707 | 300 | 707 | 300 | 707 | 300 | 707 | 300 | 707 | 300 | 707 | 300 | 707 | 300 | 707 | 300 | 707 | 300 | 707 |
| 20 | 1.5 | | | | | | | | | | | | | | | | | | | | | |
| | 2.5 | | | | | | | | | | | | | | | | | | | | | |
| | 3.5 | | 0.0 | 0.0 | 0.0 | 0.0 | 0.1 | 0.0 | 0.2 | 0.1 | 0.1 | 0.2 | 0.6 | 0.6 | 0.2 | 0.3 | 0.7 | 0.9 | 0.2 | 0.8 | 1.0 | 1.6 |
| | 5.0 | | 0.0 | 0.0 | 0.1 | 0.1 | 0.2 | 0.2 | 0.8 | 0.6 | 0.3 | 0.8 | 1.7 | 2.2 | 0.4 | 1.2 | 2.0 | 2.9 | 0.5 | 2.0 | 2.3 | 4.0 |
| 35 | 1.5 | | | | | | | | | | | | | | | | | | | | | |
| | 2.5 | | 0.0 | 0.0 | 0.1 | 0.1 | 0.2 | 0.2 | 0.8 | 0.6 | 0.3 | 0.9 | 1.7 | 2.6 | 0.3 | 1.3 | 1.9 | 3.9 | 0.6 | 2.0 | 2.2 | 6.2 |
| | 3.5 | | 0.1 | 0.1 | 0.3 | 0.2 | 0.5 | 0.7 | 2.4 | 2.2 | 0.7 | 2.3 | 3.9 | 7.4 | 0.8 | 3.0 | 4.3 | 9.5 | 1.4 | 4.5 | 5.0 | 12.4 |
| | 5.0 | | 0.3 | 0.2 | 1.2 | 0.9 | 1.2 | 2.3 | 6.3 | 8.1 | 0.3 | 5.9 | 8.9 | 19.5 | 2.0 | 7.1 | 9.6 | 22.7 | 2.9 | 9.5 | 10.4 | 26.3 |
| 50 | 1.5 | | 0.0 | 0.0 | 0.1 | 0.0 | 0.2 | 0.2 | 0.6 | 0.5 | 0.2 | 0.8 | 1.1 | 2.2 | 0.2 | 1.0 | 1.2 | 3.5 | 0.7 | 1.2 | 1.3 | 5.6 |
| | 2.5 | | 0.1 | 0.1 | 0.4 | 0.3 | 0.6 | 1.0 | 2.8 | 2.8 | 0.8 | 2.8 | 4.3 | 8.4 | 1.0 | 3.5 | 4.9 | 12.7 | 1.9 | 5.1 | 5.7 | 17.2 |
| | 3.5 | | 0.4 | 0.3 | 1.3 | 0.9 | 1.3 | 2.6 | 6.6 | 8.5 | 1.7 | 6.3 | 9.2 | 22.7 | 2.2 | 7.5 | 10.1 | 27.3 | 3.6 | 10.2 | 11.2 | 32.7 |
| | 5.0 | | 1.1 | 0.8 | 4.3 | 3.2 | 2.7 | 7.2 | 14.9 | 25.6 | 3.9 | 14.0 | 19.6 | 51.1 | 5.0 | 16.2 | 20.8 | 57.0 | 6.9 | 20.5 | 22.0 | 63.1 |

**Figure 4.12: Table of Average Net Power Produced for Selected Values of Permeability, Thickness, Radius, Depth, and Temperature Gradient with a Fixed Injection and Production Well Diameter of 0.41 m [MWe].** Permeability, depth, and temperature gradient combinations are highlighted which were previously shown to have higher power production than brine (Adams et al., 2015).

Consistent with previous findings, the average power increases with increases to depth, temperature gradient, and permeability. For fixed values of depth, temperature gradient, permeability, and radius, increasing the thickness results in an increase in power produced. These results may be compared to those of the pure-$CO_2$ inverted 5-spot reservoir of Adams et al. (2015) using the 300 m thickness and 707 m radius values. For injection and production well diameters of 0.41 m, a reservoir permeability of 5 x$10^{-14}$ m$^2$, temperature gradient of 35 °C km$^{-1}$, and depth of 2.5 km, Adams et al. (2015; Figure 3.6A) reported a net power of 3.6 MWe, which can be compared to 2.6 MWe here. The difference (-32%) can be attributed to the higher pressure differential of the more realistic reservoir considered here, which is initially filled with brine. The power shown here can be improved upon; it increased slightly (+0.1 MWe or 4%) through the improved selection of reservoir radius (Figure 4.11B).

As previously discussed, power does not necessarily increase with radius, although this tends to occur for the two radii shown in Figure 4.12, especially at high permeabilities. For permeabilities of 5 x$10^{-14}$ $m^2$ and above, a radius of 707 m produces more power on average than a 300 m radius; however, at low permeabilities, especially those at shallow depth and low temperature, the power output at a radius of 707 m can be lower than 300 m.

Averaging net power values over a 50 year period may include long periods where the temperature is depleted and power production is low (e.g. the 300 m radius power curves of Figure 4.10A). Therefore, Figure 4.13 shows the percent change in average net power when only a 30 year averaging period is used for the data sets shown in Figure 4.12. Values are colored to indicate positive (green) and negative (red) change in average power value.

Percent Change in Power from 50 to 30 Year Averages [%]

| Temp Gradient [°C km$^{-1}$] | Depth [km] | 1x10$^{-15}$ | | | | 1x10$^{-14}$ | | | | 5x10$^{-14}$ | | | | 1x10$^{-13}$ | | | | 1x10$^{-12}$ | | | | Permeability [m$^2$] |
|---|---|---|---|---|---|---|---|---|---|---|---|---|---|---|---|---|---|---|---|---|---|---|
| | | 50 | | 300 | | 50 | | 300 | | 50 | | 300 | | 50 | | 300 | | 50 | | 300 | | Thickness [m] |
| | | 300 | 707 | 300 | 707 | 300 | 707 | 300 | 707 | 300 | 707 | 300 | 707 | 300 | 707 | 300 | 707 | 300 | 707 | 300 | 707 | Radius [m] |
| 20 | 1.5 | | | | | | | | | | | | | | | | | | | | | |
| | 2.5 | | | | | | | | | | | | | | | | | | | | | |
| | 3.5 | | | | | | | -2 | -6 | 33 | -6 | 15 | -6 | 41 | -3 | 24 | -3 | 47 | 23 | 32 | 1 | |
| | 5.0 | | | | | 7 | -6 | 2 | -6 | 43 | -2 | 27 | -3 | 48 | 7 | 32 | -1 | 53 | 30 | 36 | 1 | |
| 35 | 1.5 | | | | | | | | | | | | | | | | | | | | | |
| | 2.5 | | | | | 20 | -6 | 5 | -6 | 49 | 3 | 39 | -3 | 57 | 18 | 44 | 0 | 57 | 49 | 57 | 6 | |
| | 3.5 | | | -3 | -6 | 32 | -6 | 17 | -6 | 49 | 12 | 43 | -1 | 51 | 28 | 44 | 2 | 54 | 42 | 44 | 6 | |
| | 5.0 | -1 | -6 | -1 | -6 | 40 | -4 | 32 | -4 | 32 | 24 | 44 | 2 | 53 | 36 | 45 | 4 | 55 | 43 | 45 | 6 | |
| 50 | 1.5 | | | | | 36 | -6 | 16 | -6 | 57 | 8 | 57 | -4 | 57 | 34 | 57 | 1 | 57 | 57 | 57 | 25 | |
| | 2.5 | -2 | | -2 | -6 | 39 | -6 | 23 | -6 | 51 | 20 | 47 | -1 | 55 | 36 | 47 | 5 | 57 | 46 | 49 | 11 | |
| | 3.5 | -2 | -6 | -2 | -6 | 43 | -3 | 32 | -5 | 52 | 29 | 47 | 3 | 54 | 40 | 47 | 6 | 56 | 46 | 47 | 10 | |
| | 5.0 | 0 | -6 | -1 | -6 | 47 | 1 | 42 | -2 | 54 | 37 | 47 | 5 | 55 | 43 | 47 | 7 | 56 | 45 | 47 | 9 | |

**Figure 4.13: Percent Change in Average Net Power Produced when a 30 Year Average is Used Instead of a 50 Year Average [%].** Positive changes are indicated by green while negative values are shown in red. Large positive changes between 50 and 30 year averages indicate a substantially depleted reservoir at the 30 year mark, while negative values indicate thermal breakthrough has not yet occurred.

For permeabilities of 5 x$10^{-14}$ $m^2$ and greater, average power increases for most 300 m radius reservoirs, while increases were moderate for a 707 m reservoir with a 50 m thickness and neutral for a 300 m thickness. Conversely, for a permeability of $10^{-14}$ $m^2$,

300m radius reservoirs have a moderate increase of net power, while 707 m reservoirs decrease in power. Similarly for a permeability of $10^{-15}$ $m^2$, all scenarios have a decrease in net power.

A positive change in average net power in Figure 4.13 (green) indicates that thermal breakthrough occurred in the reservoir and it is operating at a fraction of its peak power potential toward the end of its 50 year lifetime. Large values indicate substantial thermal depletion has occurred (e.g. most 300 m radius cases), and larger radius wells should be used. Conversely, negative changes in power (red) indicates that the net power is continuing to rise beyond 30 years (e.g. the 707 m radius curves in Figure 4.10A). In these cases, thermal breakthrough has not yet occurred, and continued decreases in the reservoir pressure differential with time (Figure 4.2) cause increased mass flowrate and net power.

From Figure 4.13 we can infer that for a 300 m thickness reservoir, a 707 m radius well will not deplete substantially for any of the reservoir combinations shown over a 50 year lifetime; however, improved performance may be found at smaller radii, as previously discussed. At low permeability, such as $10^{-14}$ $m^2$, a 707 m radius well does not deplete for either a 50 m or 300 m thickness, while none of the reservoir thicknesses and radii considered deplete over 50 years in a $10^{-15}$ $m^2$ reservoir.

As depth increases for most reservoirs, the percent change in average net power in Figure 4.13 tends to get more positive. This is typical as increases in depth lead to increases in mass flowrate, depleting the reservoir more quickly. Thus, decreasing the reservoir averaging time for deep reservoirs tends to produce higher average power values. However, the reverse trend occurs for a reservoir temperature gradient of 50 °C $km^{-1}$, at high permeabilities (>$10^{-13}$ $m^2$). In this subset of cases, the percent change increases with decreasing depths, indicating larger thermal depletion at shallow rather than deep reservoirs. This trend is caused by the $CO_2$ cycle operating close to the critical pressure ($P_c$ = 7.4 MPa) at high temperature. In these cases, the specific heat of $CO_2$ is much

higher than usual (>30%), resulting in higher heat extraction at shallow depths, despite lower mass flowrate.

### 4.3.3 Average Net Power Sensitivity to Well Pipe Diameter

The effect of well diameter on average net power is shown in Figure 4.14 for both a 5 $x10^{-14}$ $m^2$ and 1 $x10^{-12}$ $m^2$ permeability reservoir at a depth of 2.5 km and a 35 °C $km^{-1}$ geologic temperature gradient. Well diameter and reservoir permeability are two critical factors which affect the mass flowrate generated by the thermosiphon (Adams et al., 2014), thus they are shown in Figure 4.14 for comparison.

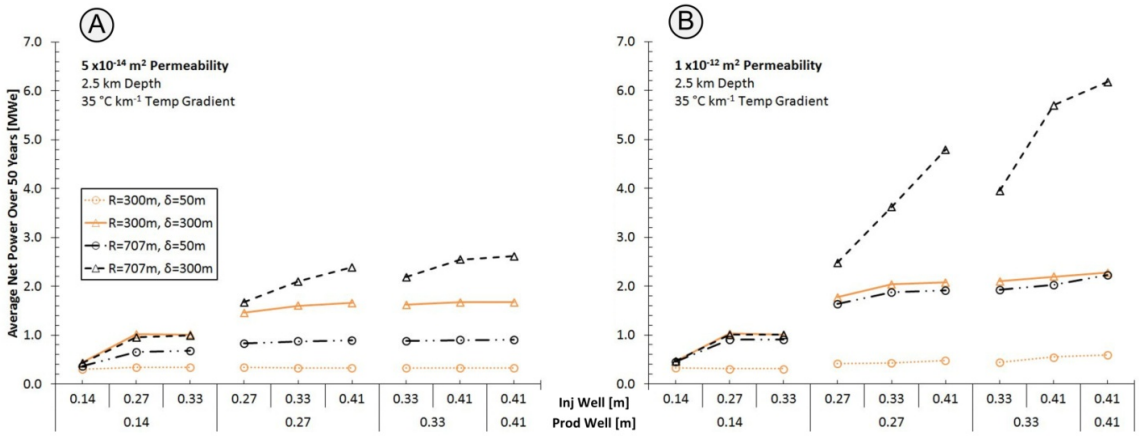


**Figure 4.14: Average Power Over 50 Years for Varying Well Diameters for: A) a 5 $x10^{-14}$ $m^2$ Permeability Reservoir, and B) a 1 $x10^{-12}$ $m^2$ Permeability Reservoir for Radii of 300 and 707 m and Thicknesses of 50 and 300 m [MWe]**

For increasing injection and production well diameter, the average net power tends to increase. Likewise, increases in permeability tend to increase power produced; however this effect is diminished at small pipe diameters. At large permeability (Figure 4.14B), the fraction of frictional pressure losses due to the reservoir tends to be low; therefore net power output is substantially increased by increasing well diameter. Likewise, at low permeability (Figure 4.14A) the fraction of frictional pressure losses due to the reservoir is large, so the net power output is less sensitive to the pipe diameter.

For each combination of thickness and radius, there appears to be a combination of injection and production well diameters where a plateau in net power production is achieved. The exception to this trend is the 707 m radius and 300 m thickness case in Figure 4.14B, where power increases for all increases in pipe diameter. These results notably differ from those previously found (Adams et al., 2015—Figure 3.10A), which indicated that power increased for all increases in pipe diameter. Adams et al. (2015) did not consider the temperature depletion that occurs with time and its effect on power production.

In Figure 4.14B, for injection and production well diameters greater than 0.27 m and 0.27 m, respectively, the power peaks due to the rapid thermal depletion of the reservoir which the larger diameter pipes provide. While the average power production of these cases is roughly equivalent, cases with larger pipe diameter have more variability of power production with time. Conversely, the 707 m radius and 300 m thickness case in Figure 4.14B does not thermally deplete the reservoir for large values of pipe diameter, as previously indicated in Figure 4.13. Thus, if a sufficiently large reservoir is used to prevent temperature depletion, large pipe diameters may be used to maximize power production; however, if the reservoir volume is pre-determined, the wells need to be sized accordingly to avoid installation of unnecessarily large piping. Further, the correct sizing of pipe will decrease the net power variation with time, decrease the over-sizing of power plant equipment, and therefore increase the capacity factor of that equipment.

## 4.4 Conclusions

In this paper, we characterized the pressure drop and temperature decay in sedimentary radial reservoirs used in CPG power systems and then found time-dependent values of power for variations in well diameter, reservoir radius, thickness, and permeability. Our findings are:

*For a given reservoir, an optimum radius exists which will produce the most average power over a specified time.* Increasing the reservoir radius increases both the pressure differential and the thermal mass available for heat extraction. Thus, small radius reservoirs will flow more quickly, but will deplete rapidly. Conversely, large radius reservoirs have slower flowrates and slowly deplete. Therefore, a radius can be selected which will provide the highest average power production over a specified time. Additionally, as the reservoir permeability increases, so does the optimum radius.

*Over-estimation of the reservoir radius affects the long-term power output less severely than under-estimation.* At radii larger than the optimum value, the average net power tends to decrease less per meter radius than at radii smaller than the optimum radius. The correct sizing of the radius is more important at small permeabilities where the percent decrease of average net power per meter radius on either side of the optimum radius is more substantial.

*Increasing injection and production well diameter for a fixed radius does not necessarily increase average net power production.* While increasing the well diameters will increase the instantaneous mass flowrate and therefore net power production, it will extract heat from the reservoir at a greater rate, thermally depleting it more quickly and will lead to a lower steady-state temperature. Thus, for a given reservoir thickness and radius, a smaller well can be used to extract energy at a slower, but more constant rate, yielding the same average net power production over the time period. Controlling the heat extraction rate in such a way would also decrease the installed capacity of the surface plant while allowing for a greater capacity factor.

*Increasing the reservoir thickness results in an increase in average power produced.* All other factors constant, increasing the reservoir thickness increases the reservoir cross-sectional area which is inversely proportional to the reservoir pressure differential (Equation 4.3). Decreases to the reservoir pressure differential result in higher mass

flowrates, and when combined with the increased thermal mass of rock from the increased thickness, the system produces more power over time.

*The temperature decay profile of a sedimentary reservoir can be approximated using a two-variable error function and exponential combination curve across the parameter space.* On average, the combined error function and exponential curve fit the 330 individual datasets well ($r^2 = 0.989$). The two variables, $p_1$ and $p_3$, scaled the curve vertically and horizontally, respectively; $p_1$ accounted for the decrease in swept area and heat conduction as reservoir thickness increases, while $p_3$ accounted for the shift in steady-state temperature as the ratio of heat extraction to conduction from the surrounding rock varied. Using the zeroeth-order fit provided here, temperature fraction was predicted well, with a 95% prediction interval of ±0.096.

## 4.5 Nomenclature

Nomenclature for these simulations is provided in Table 4.3.

**Table 4.3: Nomenclature**

| | |
|---|---|
| *a, b* | Pressure Differential Fit Variables [dim] |
| *A* | Reservoir Vertical Cross-Sectional Area [$m^2$] |
| *C* | Slope Constant at erfc/exp Interface [dim] |
| $C_p$ | Specific Heat at Constant Pressure [J $kg^{-1}$ °$C^{-1}$] |
| *h* | Specific Enthalpy of Fluid [J $kg^{-1}$] |
| *k* | Thermal Conductivity [W $m^{-1}$ °$C^{-1}$] |
| $\dot{m}$ | Mass Flowrate [kg $s^{-1}$] |
| *p1, p2* | Temperature Fraction Fit Variables [dim] |
| *p3* | Steady-State Temperature Fraction [dim] |
| *P* | Power [MWe] |
| $P_{net}$ | Net Power Generated [MWe] |
| $P_{net,avg}$ | Average Net Power Generated (50 Years) [MWe] |
| *ΔP, dP* | Reservoir Pressure Differential [kPa] |
| $\Delta P_0$ | Steady-state Reservoir Pressure Differential [kPa] |
| $\Delta P_{ideal}$ | Darcy 1D Pressure Differential [kPa] |
| $\dot{Q}$ | Heat Energy Transfer Rate [MWth] |
| *Q* | Volumetric Flowrate [$m^3$ $s^{-1}$] |
| *R* | Reservoir Radius [m] |
| $se_y$ | Standard Error of Estimate of *y* [*y* units] |

| | |
|---|---|
| $t$ | Time [s] |
| $T$ | Temperature [°C] |
| $T_{inj}$ | Temperature at Injection into Reservoir [°C] |
| $z$ | Elevation [m] |
| $\Gamma$ | Temperature Fraction [dim] |
| $\delta$ | Reservoir Thickness [m] |
| $\kappa$ | Scalar Reservoir Permeability [$m^2$] |
| $\mu$ | Dynamic Fluid Viscosity [N s $m^{-2}$] |
| $\nu$ | Kinematic Viscosity [$m^2$ $s^{-1}$] |
| $\rho$ | Fluid Density [kg $m^{-3}$] |
| $\tau$ | Dimensionless Time [dim] |
| $\Psi$ | Reservoirs of Heat Extracted [dim] |

## 4.6 Supplemental Data

The power production values for all cases simulated are attached to this paper as an EXCEL file.

## 4.7 Acknowledgements

The authors gratefully acknowledge funding from a National Science Foundation (NSF) Sustainable Energy Pathways (SEP) program grant (1230691). We also thank the Initiative for Renewable Energy (IREE) for initial seed funding.

Chapter 5

# CPG vs. Wind and Solar: A Dispatchable Renewable

## Preface

The previous chapters have been concerned with questions of CPG power production itself, such as: how can electricity be produced, how much electricity can be made, or how electricity production changes over time. However, the future utilization of CPG will not only depend on its power generation potential, but also on how flexibly it can deliver its power to meet electrical demand.

Geothermal electricity, unlike other renewable energies such as wind and solar, is a form of energy storage in-and-of itself. Heat is stored within the reservoir and it is extracted at

a time and rate set by the CPG plant operator. Conversely, wind and solar may only produce electricity when the wind blows or the sun shines. Therefore, geothermal electricity is dispatchable—its power may be provided on-demand, up to the nameplate limit of the plant.

Many states have mandated their electric utilities meet a renewable energy standard. For example, public utilities in Minnesota are required to generate 26.5% of their electricity from renewable sources by 2025 (DSIRE, 2015). This is not a trivial standard for electric utilities to meet—wind and solar tend to be erratic in production. Instead of relying on baseload power generation, electric utilities now have to purchase an unreliable power source and provide a dispatchable backup source for when it isn't available. Thus, a great opportunity exists for geothermal as it is both renewable and dispatchable.

In this paper, we estimate the size of a CPG, wind, or solar plant which would be needed to meet the electrical power demand of Minot, ND. Minot was chosen for its CPG generating potential—it is situated over a sedimentary basin (Williston) and has a low average ambient temperature causing electrical demand to peak in the winter (winter-peaking). A peak winter demand power curve more closely matches the power output of a CPG plant than winter-peaking or constant power demand. CPG has a low temperature differential between produced fluid and ambient air, thus, its power output is particularly sensitive to changes in ambient temperature, and power production is substantially greater in the winter. The site has a good to excellent wind potential rating (NREL, 2009b) and a low to moderate solar potential (NREL, 2012).

## Citation

Adams, B., & Kuehn, T.H. (2012). The complementary nature of $CO_2$-plume geothermal (CPG) energy production and electrical power demand. *Proceedings of the ASME 2012 International Mechanical Engineering Congress & Exposition*, IMECE2012-88704, November 9-15, 2012, Houston, Texas, USA. http://dx.doi.org/10.1115/IMECE2012-88704

**Proceedings of the ASME 2012 International Mechanical Engineering Congress & Exposition**
**IMECE2012**
**November 9-15, 2012, Houston, Texas, USA**

**IMECE2012-88704**

# The Complementary Nature of $CO_2$-Plume Geothermal (CPG) Energy Production and Electrical Power Demand

**Benjamin M. Adams**
University of Minnesota
Department of Mechanical Engineering
Minneapolis, Minnesota, USA
adam0068@umn.edu

**Thomas H. Kuehn**
University of Minnesota
Department of Mechanical Engineering
Minneapolis, Minnesota, USA
kuehn001@umn.edu

## Paper Summary

$CO_2$ Plume Geothermal (CPG) energy generation is a renewable technology that uses $CO_2$ as the geologic working fluid within naturally permeable, sedimentary thermal reservoirs. In this paper, we compare the ability for CPG geothermal technology to meet electrical demand requirements, compared with other renewable technologies, for a 10MW, northern climate town near Minot, North Dakota. Wind and solar are both supply-driven technologies, capturing energy when it is available; However CPG is demand-driven—the rate at which energy is removed from within the earth is chosen to

meet electrical demand. Using meteorological data, we compare estimated system performance with actual 2010 electrical load to gage each system's ability to meet demand.

CPG is found to most closely match system demand during the three-season (fall, winter, spring) year, where solar production is inversely related to demand. At the same time, wind does not track demand during any portion of the year, consistently having a large variability. None of these renewable technologies was found to track demand all year. Ultimately we show that CPG may be used to reliably track hourly demand during 95% of the year—an unattainable result for wind and solar.

**Keywords**: Geothermal, CO2, Renewable Energy, Electrical Demand, Load Following

## 5.1 Introduction

Recent legislation is curtailing the emission of carbon dioxide from new industrial emitters, such as coal-fired power plants. Coal is still in abundant supply, so Carbon Capture and Sequestration (CCS) technology is being utilized to capture emitted $CO_2$ and store it geologically. The preferred storage medium for this fluid is in deep, naturally permeable saline aquifers. In traditional CCS, this $CO_2$ is stored indefinitely.

A research team at the University of Minnesota has developed and researched a novel geothermal energy generation technology, $CO_2$ Plume Geothermal (CPG), which utilizes these sequestered $CO_2$ deposits to produce electricity as shown in Figure 5.1. In CPG, injected $CO_2$ is produced through a second well to the surface where it is used to power a turbine in a direct system, or to supply thermal energy to a secondary power system or organic Rankine cycle. CPG adds value to CCS operations by producing geothermal energy, instead of simply landfilling the gas. $CO_2$ has much lower viscosity than water found in traditional geothermal systems, which greatly reduces the geologic pressure losses, while having a similar specific heat.

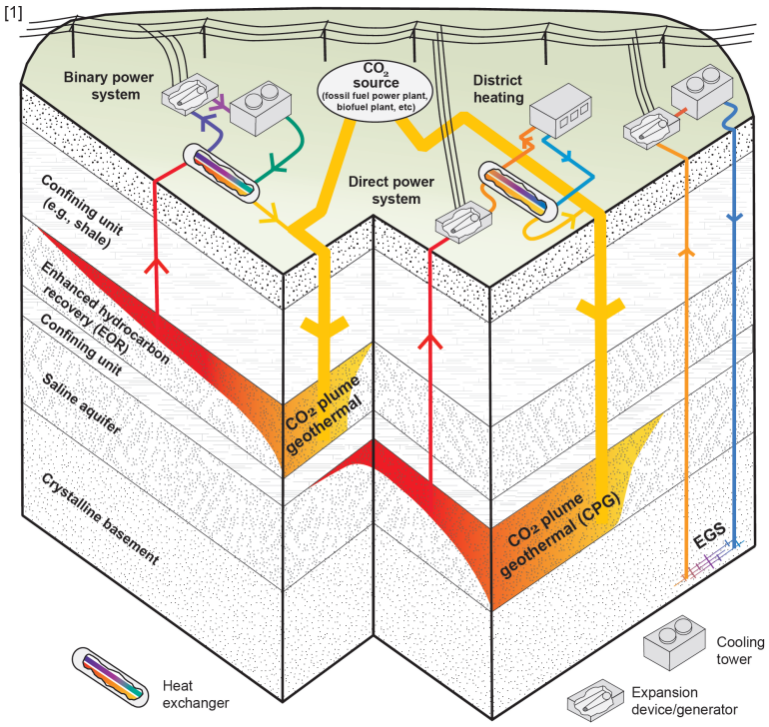


**Figure 5.1: CPG System Concept Showing $CO_2$ Sequestration in Saline Aquifers**
(source: Randolph and Saar, 2010)

CPG also has advantages when compared to other $CO_2$-based geothermal systems. Enhanced Geothermal Systems (EGS) use hydro-fracturing to increase the permeability of a reservoir to allow the working fluid to pass through; however, this process is costly and destructive. Conversely, CPG utilizes currently existing, high permeability formations, such as sandstone, which are available in most geographic locations.

Geothermal energy is a renewable energy resource that differs from most others. Wind and solar both derive from the sun and the immediate effects of solar radiation. However, geothermal energy is the removal of stored, naturally occurring energy within the earth, which occurs from cooling of the core and radioactive decay (SMU, 2012a; Blackwell and Richards, 2004). The geothermal temperature gradient of the crust in the United States is between 15 and 75 °C $km^{-1}$, depending on location (SMU, 2012b). So electrical production from a geothermal resource is governed by the heat extraction rate of the surface plant as demand dictates—not by a supply driven resource, such as wind and solar.

This paper analyzes the relationship between electrical demand and the ability for CPG, compared with wind and solar, to meet this demand. We use electrical demand data from 2010 from the Midwest, and model the production from these renewable technologies. First, we describe the development of our geothermal model and data selection, then we compare and size the technologies, illustrating the demand-matching capability of CPG power generation.

## 5.2 Method

$CO_2$ Plume Geothermal (CPG) technology is essentially a Supercritical Rankine heat engine, generating electrical power by transferring thermal energy from a higher temperature resource within the earth to the lower temperature atmosphere, as illustrated in Figure 5.2. The thermal efficiency of a heat engine is determined in part by the temperature difference between high and low temperature resources. Geothermal power plants often have only a 100°C to 150°C temperature difference that results in low (< 30%) thermal efficiencies. As such, the performance of a plant is greatly affected by the ambient rejection temperature. This is not a significant factor with high temperature (combustion) resources.

A CPG plant will have greater efficiency during periods of low rejection temperatures, as seen in winter, and lower efficiency in summer. This leads us to select a climate where electrical demand would be largest, or at least substantial, during the winter months. In addition, a geographic location for this study which is amenable to geothermal energy generation would be preferred. This leads us to select Minot, North Dakota, as the focal point of this research, due to its northern climate and location within the Williston Basin.

Climate data was collected for 2010 from the National Climactic Data Center, using hourly dry-bulb temperature readings from the Minot International Airport Weather Station (NCDC, 2012). A geothermal temperature gradient of 25 °C $km^{-1}$ was estimated using SMU heat maps, and a depth was selected to obtain a 100°C thermal reservoir (SMU, 2012b).

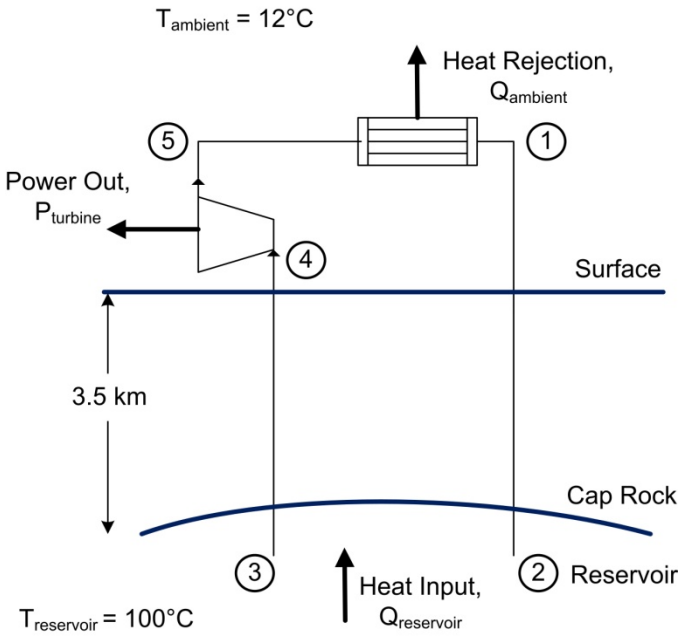


**Figure 5.2: CPG System Schematic for Minot, North Dakota**

Using this information, the CPG system was modeled using a direct system, shown in Figure 5.2. The $CO_2$ is injected from State 1 nearly-isentropically to State 2, with piping losses due to the 0.25 m diameter piping having a surface roughness of 45 μm. The fluid flows through the reservoir in a supercritical state, arriving at State 3 having heated completely to the reservoir temperature, and decreased to the hydrostatic pressure at depth, 35 MPa. The same porosity, permeability, and pressure losses are used as our base case simulations (Janke and Kuehn, 2011). Fluid is produced nearly-isentropically to State 4, subject to the same piping losses, where it propels a 78% efficient, multiphase turbine to State 5. The $CO_2$ is then cooled to within 5°C of ambient temperature, where it is again reinjected at State 1. This power data was normalized by the peak production value, to obtain hourly capacity factors for the year.

Engineering Equation Solver (EES) is a simultaneous equation solver with built-in thermodynamic state data which was used to evaluate the model. For the initial mass flowrate of 80 kg/s, we start at an initial known State 3, which is at the reservoir temperature of 100°C, and 35 MPa, consisting of 100% $CO_2$. Flow was numerically

integrated up the well in 30 sections, 117 meters long, using an energy balance, patched Bernoulli, and continuity Eqs. (5.1), (5.2), and (5.3), respectively.

$$h_2 + gz_2 = h_1 + gz_1 \tag{5.1}$$

$$P_2 + \rho_2 g z_2 = P_1 + \rho_1 g z_1 - f \frac{L}{D} \frac{\rho_1 V_1^2}{2} \tag{5.2}$$

$$\dot{m} = \rho A V \tag{5.3}$$

Subscripts 1 and 2 denote the beginning and end of the fluid element and the friction factor was found using the Reynolds number of the fluid combined with the assumed pipe surface roughness of 45 μm for Schedule 80 commercial steel piping and looking up the value on the Moody Chart (Moody, 1944). Bulk fluid values were used in all cases. This yields State 4.

State 5 was found from State 4 using the 78% isentropic turbine efficiency, however the low pressure side of the turbine is determined as an end result of the other thermodynamic processes within the system. Then the fluid is sub-cooled, resulting in a liquid, 5°C above the ambient temperature at State 1. State 2 was calculated numerically, with the same procedure as described above with Eqs. (1), (2), and (3). Finally, from the pressure loss through the reservoir was found using our existing TOUGH2 geologic model as described in Randolph and Saar (2010), with a rock permeability of 5 x$10^{-14}$ $m^2$. The low side pressure of the turbine was found last, such that States 1 and 2 had the appropriate pressures. The power produced is then the product of the mass flowrate and the enthalpy difference across the adiabatic turbine. The thermal efficiencies were found using Eqs. (5.4) and (5.5).

$$\eta_{th} = \frac{P_{turbine}}{Q_{reservoir}} = \frac{h_4 - h_5}{h_3 - h_2} \tag{5.4}$$

$$\eta_{th,carnot} = 1 - \frac{T_1}{T_3} \tag{5.5}$$

Several runs were made to find the dependence of power production on ambient temperature for an 80 kg $s^{-1}$ base case. The nearly linear dependence is shown in Figure 5.3, with the linear fit that was used with dry bulb temperature to calculate the power production of a single CPG unit. Note that the performance is not limited to above 0°C as in the case of a water-based system.

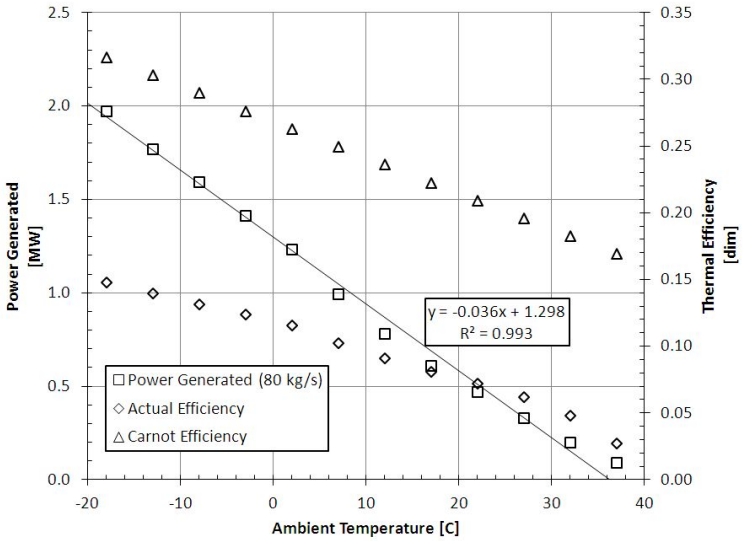


**Figure 5.3: Dependence of Power Produced on Ambient Air Temperature for 80 kg $s^{-1}$ Base Case**

Electrical demand data were obtained from Midwest Independent Transmission System Operator, Inc (MISO), which is a non-profit, member-run energy facilitator, providing for the transfer and reliability of electrical service in the Midwest, regulating ~131 GW of generation potential (MISO, 2012a). Hourly, historic demand data were provided for the "west" portion of their service area, covering Montana, the Dakotas, and presumably the western half of Minnesota, called the Summary "Historical Regional Forecast and Actual Load (rfal_HIST)" (MISO, 2012b). The data were normalized by the peak demand of 2010, to obtain hourly capacity factors for the year.

Solar data were obtained from the National Solar Radiation Database, a solar resource estimation initiative of the National Renewable Energy Laboratory (NREL, 2007a; Myers et al., 2005; NREL, 2007b). This resource provides a "Typical Meteorological Year v3"

dataset which provides solar flux on a horizontal surface specifically for the Minot, ND site, 727676. They account for solar flux measurements between the years 1976 to 2005, from 1400 measurement sites to develop a representative typical solar year. Minot is categorized as a class 1 site, indicating less than 11% uncertainty for the period. These data are not specifically for the year 2010; however these were used as they are time-averaged, quality controlled solar data, which has relatively low variability in annual mean solar flux. These data were normalized by the peak solar flux of the dataset, to obtain hourly capacity factors for the year.

Wind data were obtained from the Wind Integration Datasets provided by the National Renewable Energy Laboratory (NREL, 2006; NREL, 2009a). The dataset is an hourly estimated wind power production dataset for a hypothetical 309 MW wind farm near Minot, ND (48.17 lat, -101.23 long) for 2006. The data were normalized by the peak production value for the year, to obtain hourly capacity factors for wind.

## 5.3 Results

### 5.3.1 Trends in Demand and Production

The extent of the datasets required averaging by day, and later by week, to enhance visualization. Figure 5.4 shows the normalized power production data for the year, averaged by day with January 1$^{st}$ being Day 1. Demand has a winter peak, near day 340, and a summer peak, near day 220, with the lowest load in the spring and fall. Solar data tends to have a very low capacity factor, due to the limitation of daylight hours, with the peak of solar flux near day 180. CPG tends to meet the winter peak, but does not match the demand curve well in the summer. Wind tends to be very erratic, having no significant trend, varying across the full range of capacity factor throughout the year.

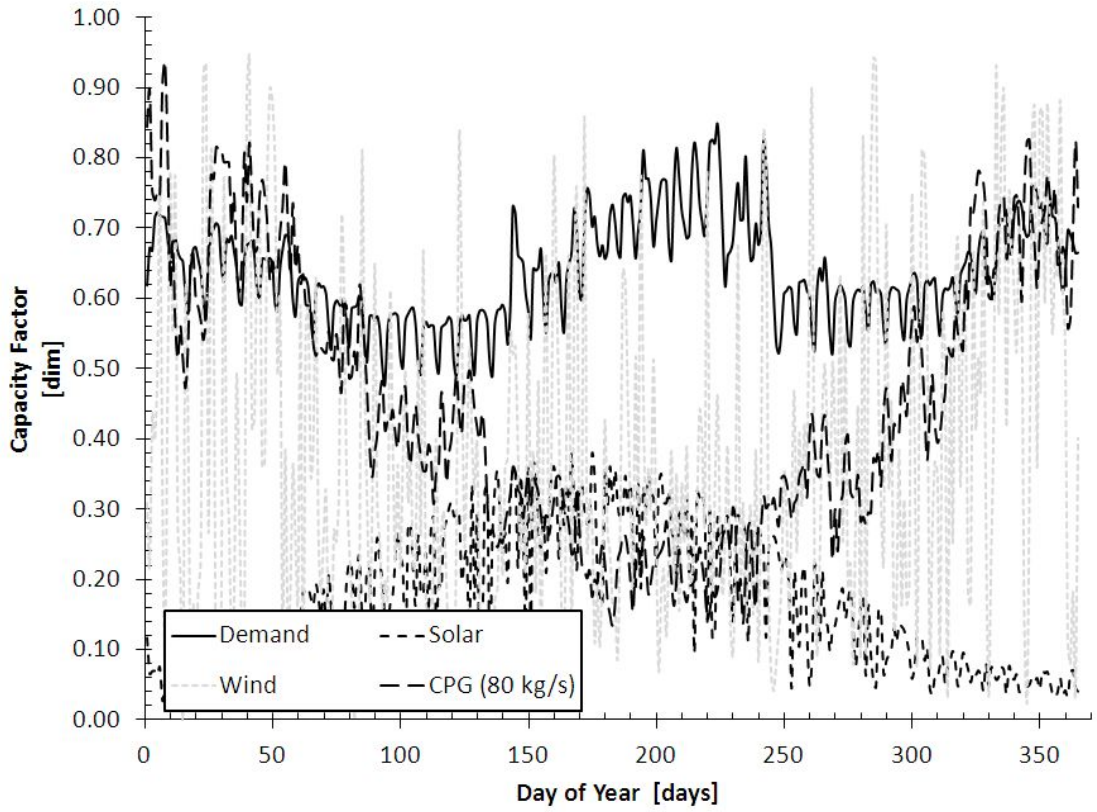


**Figure 5.4: Demand, Solar, Wind, and CPG Capacity Factor Power Curves for the Year, Averaged per Day**

When the data are averaged by week and plotted against dry bulb air temp, the trends become more clear as shown in Figure 5.5. There is a clear dependence of both demand and CPG power production on dry bulb air temperature, most visibly near week 32, which is the peak for the summer dry bulb and demand, and also the CPG production minimum for the year. The peak in solar flux occurs with a 45 day phase lag from the summer demand, and wind appears to be independent of all others.

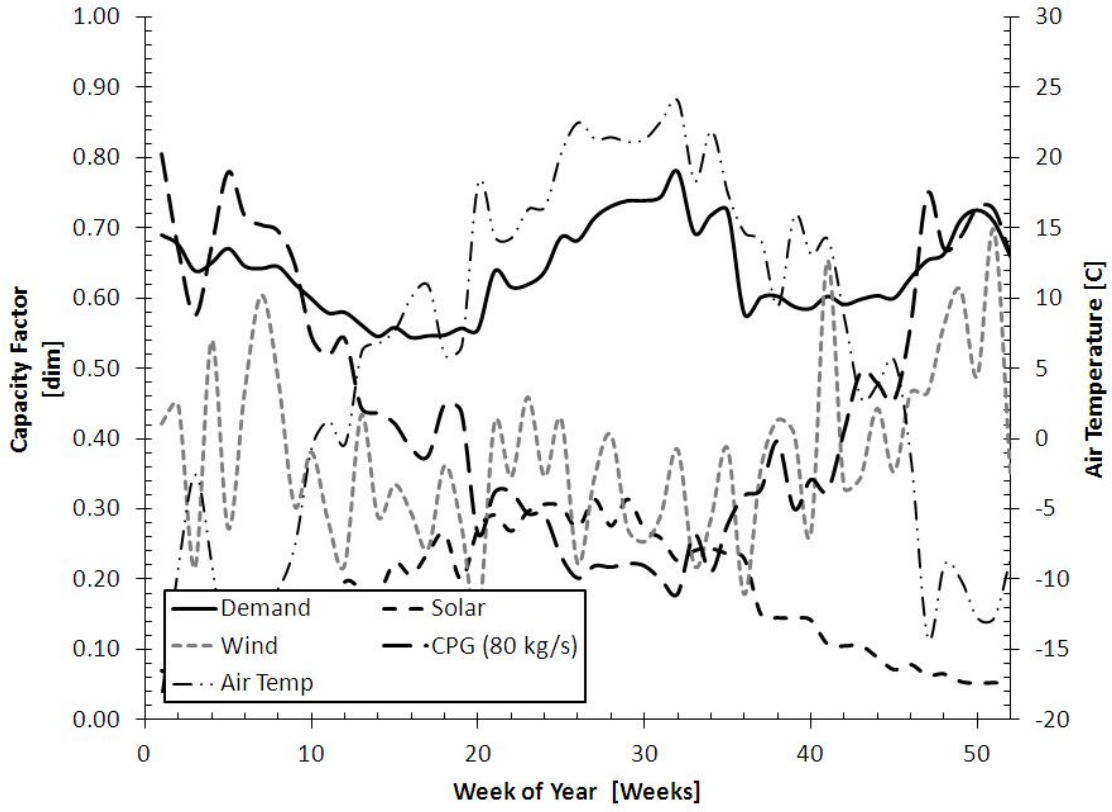


**Figure 5.5: Demand, Solar, Wind, CPG Capacity Factors, and Ambient Air Temperature, Averaged Weekly for the Year**

To quantify trends within the data, the capacity factors for each renewable technology were plotted against demand in Figure 5.6. In this arrangement, a resource that perfectly matched demand would have a slope of one, and an $R^2$ of 1. The values are then summarized in Table 5.1.

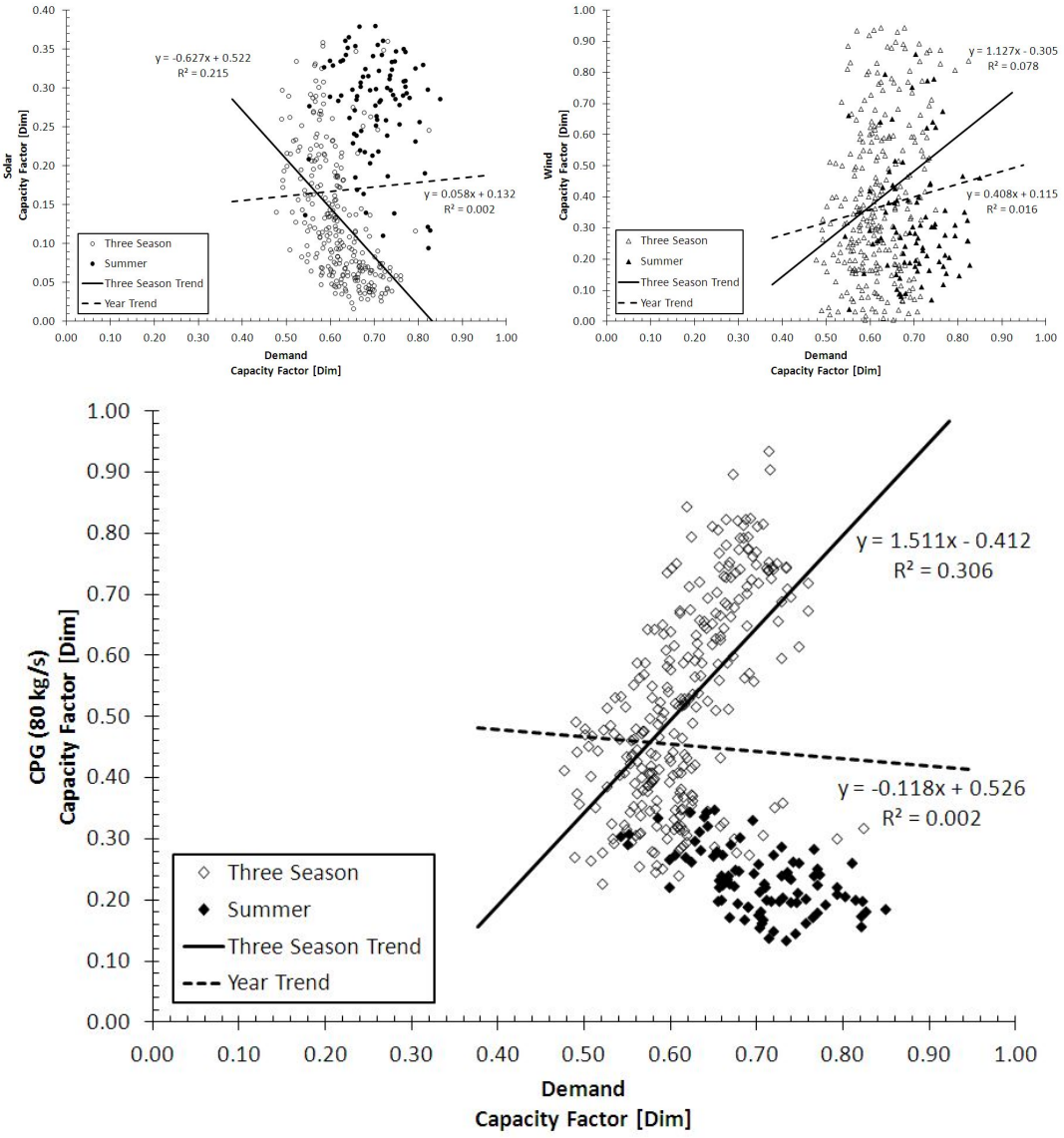


**Figure 5.6: Demand Power Correlation with CPG (Bottom), Solar (Top Left), and Wind (Top Right)**

CPG has the best correlation with demand, with two clear regions of data: a three-season and a summer region. In the three-season region, the CPG data is positively correlated with demand, while it is negatively correlated in the summer region. The CPG three-season correlation of 0.31 was the strongest for any of these technologies. The second strongest correlation was solar three-season at 0.22; however this has a negative slope, indicating an inverse correlation of production and demand, which is not beneficial. Wind data was almost evenly distributed throughout the year with little correlation with demand.

**Table 5.1: Correlation and Variation amongst CPG, Solar, and Wind**

| | Mean [dim] | Standard Dev. [dim] | $r^2$ with Demand [dim] | Slope with Demand [dim] |
|---|---|---|---|---|
| Demand – Three Season | 0.62 | 0.09 | 1.000 | 1.00 |
| Demand – All Year | 0.64 | 0.10 | 1.000 | 1.00 |
| CPG – Three Season | 0.52 | 0.18 | 0.306 | 1.51 |
| CPG – All Year | 0.45 | 0.20 | 0.002 | -0.12 |
| Solar – Three Season | 0.13 | 0.21 | 0.215 | -0.63 |
| Solar – All Year | 0.17 | 0.25 | 0.002 | 0.06 |
| Wind – Three Season | 0.39 | 0.32 | 0.078 | 1.13 |
| Wind – All Year | 0.38 | 0.32 | 0.016 | 0.41 |

The power demand curve had the least variation of any of the curves, with a standard deviation of 0.10. CPG displayed the second-least variability throughout the year with a standard deviation of 0.20, while solar and wind followed with increased variabilities of 0.25 and 0.32 respectively.

### 5.3.2 Sizing a System

After this initial characterization, each of the renewable resources was sized to meet a 10 MW peak demand with no provision for storage. The demand capacity factor was multiplied by 10 MW and was compared to the renewable selected nameplate capacity multiplied by the capacity factor. These values were compared hourly for the year, and the percentage of hours for which the demand was met through that renewable resource was calculated, shown in Figure 5.7. All three resources had a moderately flat curve at low percent demands that developed into very steep curves at higher demand values. For wind and solar this was due to zero capacity factors which often occurred. It is not possible to meet a non-zero demand during the nighttime hours with a solar panel, regardless of the panel's nameplate capacity. A similar problem occurred when the wind was not blowing. However, CPG was able to meet most electrical demand with a sufficiently upsized unit.

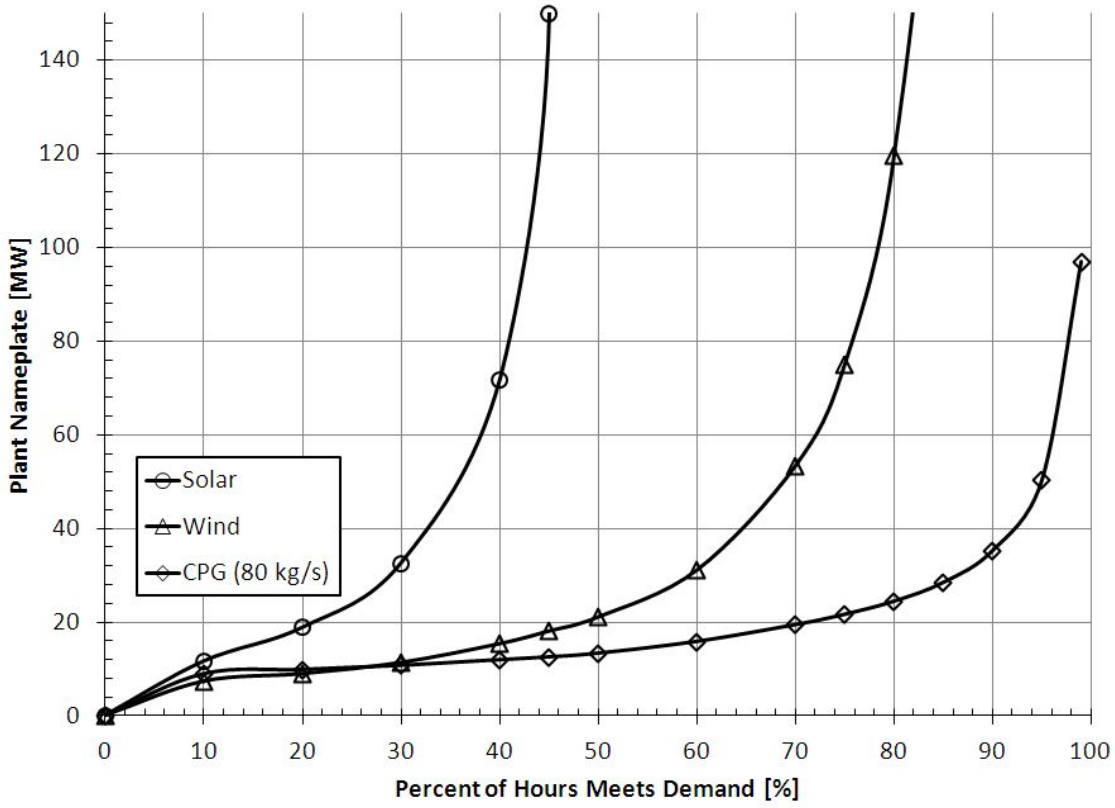


**Figure 5.7: Plant Nameplate Required to Meet Percentage of Demand**

This Percent-demand method could be used for sizing a system. For example, selecting a point near the sharp bend for each energy source would likely be an optimum, near 50 MW. This would mean the 10 MW peak system demand would be met 95%, 70%, and 35% of the time for CPG, Wind, and Solar, respectively. Alternatively, if storage were available, either through local energy storage (compressed air, batteries, etc) or grid storage (buying and selling excess energy), a unit could be sized to provide only the amount of demand energy needed on average throughout the year, as shown in Figure 5.8. In this scenario, nameplate values of 17.0 MW, 37.8 MW, and 14.2 MW are needed for the Wind, Solar, and CPG systems, respectively. Positive net power generation values indicate a deficit of energy to the grid; negative net power values indicate a surplus has been sent to the grid.

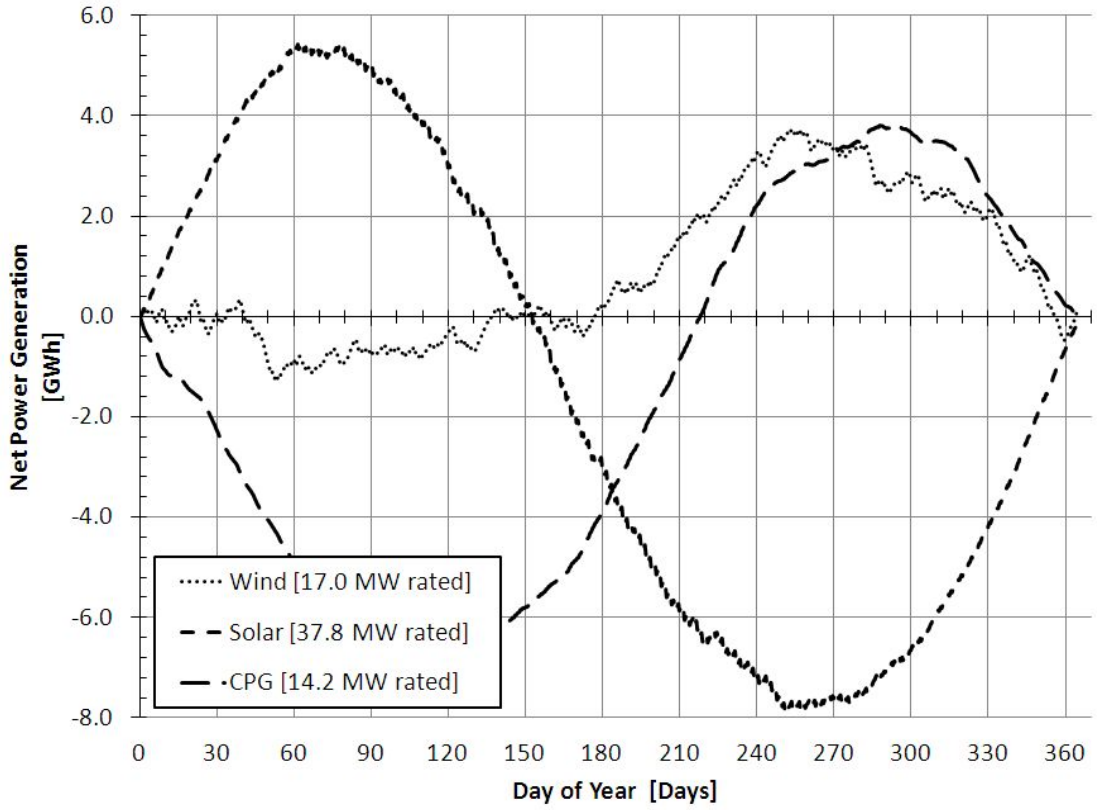


**Figure 5.8: Wind, Solar, and CPG Nameplate Sizes Needed to Provide Yearly Average Power**

### 5.3.3 Varying CPG Performance

In the analysis thus far, we have chosen a single operating condition for the CPG system: an 80 kg $s^{-1}$ mass flowrate. This value has been chosen based on typical simulation parameters that have been chosen for the system. However, the output of the CPG system is not governed by the availability of the resource, as wind and solar are—it is controlled by the heat extraction rate from the reservoir, determined by mass flowrate. Therefore, we may design a CPG system which follows the system load precisely, with some constraints. For example, if pressure losses result in the production of $CO_2$ below the ambient temperature, power generation is not possible. However, now we will show a system which will meet demand 95% of the time.

To meet the demand, the power supply curves, based on ambient temperature and mass flowrate were found and are plotted in Figure 5.9. At low mass flowrates, increasing the

flowrate increases power, as flow through the turbine increases. However at high mass flowrates, system pressure losses become important and result in a drop of pressure differential across the turbine, despite the high flowrates. These competing factors result in a maximum power output for each of these base-case CPG systems. Two mass flowrate solutions will always occur for a given desired power output, but the lower value will be chosen as it will have greater efficiency due to fewer system irreversibilities. No regard was made in this analysis for turbine roll-off or other non-peak performance issues.

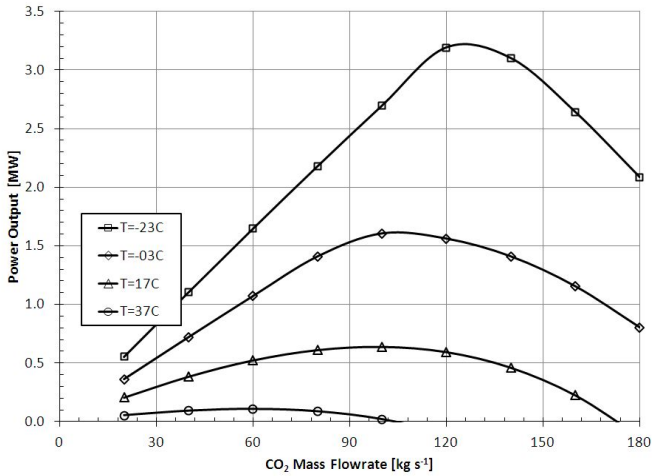


**Figure 5.9: Variation in CPG Power Output based on Mass Flowrate and Ambient Air Temperature**

It was found that approximately 20 of these CPG units were needed to meet the 50MW nameplate requirement to handle the hourly load 95% of the time. For each hour, the dry bulb temperature and demand value were used to find the required mass flowrate. These flowrates, and the corresponding actual power production are illustrated in Figure 5.10. The CPG system follows the demand well except for a period of high summer demand and dry bulb temperatures between weeks 24 and 34. In this period, it meets as little as 80% of the load, and would require other energy sources less sensitive to the ambient to provide backup.

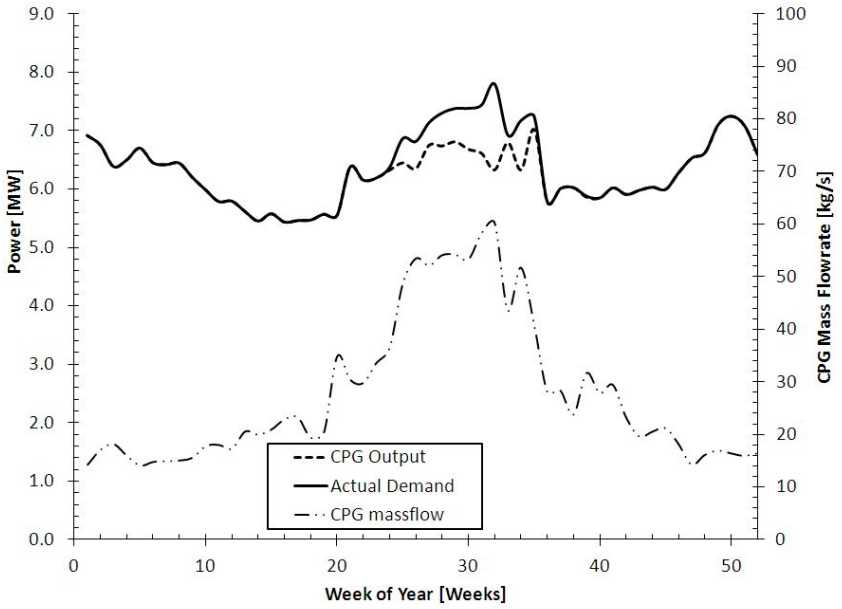


**Figure 5.10: CPG Mass Flowrate and Corresponding Power Production**

The dependence on ambient temperature also becomes very clear during the summer operating months of the CPG system. The summer demand peak is nearly equal to the winter peak, however a mass flowrate four times larger is required. This shows how a CPG power system would be very well suited to northern climates with low summer peaks.

## 5.4 Conclusions

We have shown how the CPG system is a demand-driven renewable energy source, not a resource-driven energy source, such as wind and solar. A 50 MW nameplate CPG system was needed to meet 95% of the demand hours, a value unattainable by wind and solar.

We have shown that even though it is demand-driven, if it is left alone at a constant flowrate, it still meets the three-season load more reliably than solar or wind. CPG has a positive correlation to load for the three-season region, with a $R^2$ of 31%. For the same region, solar was negatively correlated, and wind was erratic and variable.

We have shown than none of these three renewable technologies is capable of meeting the year-round load by itself without backup.

We have shown that if storage options are available, CPG is able to meet the average yearly demand with a 16% lower nameplate capacity than wind, and a 61% lower nameplate capacity than solar. This is because the CPG resource is always available and the equipment is never unutilized.

## 5.5 Acknowledgements

The authors wish to acknowledge support from the Initiative for Renewable Energy & the Environment (IREE), part of the Institute on the Environment, at the University of Minnesota.

## 5.6 Nomenclature

| | |
|---|---|
| A | Cross-Sectional Area of Pipe [$m^2$] |
| D | Diameter of Pipe [m] |
| f | Friction Factor, From Moody Chart [dim] |
| g | Gravitational Constant, 9.8 [m $s^{-2}$] |
| h | Fluid Enthalpy [J $kg^{-1}$] |
| $\dot{m}$ | Fluid Mass Flow Rate [kg $s^{-1}$] |
| P | Fluid Pressure [Pa] |
| V | Fluid Bulk Velocity [m $s^{-2}$] |
| z | Fluid Elevation [m] |
| ρ | Fluid Bulk Density [kg $m^{-3}$] |

# Bibliography


Adams, B., & Kuehn, T.H. (2012). The complementary nature of $CO_2$-plume geothermal (CPG) energy production and electrical power demand. *Proceedings of the ASME 2012 International Mechanical Engineering Congress & Exposition*, IMECE2012-88704, November 9-15, 2012, Houston, Texas, USA.

Adams, B.M., Kuehn, T.H., Bielicki, J.M., Randolph, J.B., & Saar, M.O. (2014). On the importance of the thermosiphon effect in CPG ($CO_2$ plume geothermal) power systems. *Energy*, 69, 409-418. http://dx.doi.org/10.1016/j.energy.2014.03.032

Adams, B.M., Kuehn, T.H., Bielicki, J.M., Randolph, J.B., & Saar, M.O. (2015). A comparison of electric power output of $CO_2$ Plume Geothermal (CPG) and brine geothermal systems for varying reservoir conditions. *Applied Energy*, 140, 365-377.

Adams, B.M., Kuehn, T.H., Bielicki, J.M., Garapati, N., & Saar, M.O. (In preparation). A characterization of temperature depletion in a sedimentary basin and its effect on the electric power output of $CO_2$ plume geothermal (CPG) power systems. *Geothermics*.

Adams, B.M., Kuehn, T.H., Randolph, J.B., & Saar, M.O. (2013). The reduced pumping power requirements from increasing the injection well fluid density. *GRC Transactions*, 37, 667-672.

Agarwal, V., & Anderson, B. (2010) An integrated model to compare net electricity generation for $CO_2$ and water based geothermal systems. *GRC Transactions*, 34, 277-283.

Armstead, H.C.H., Tester, J.W. (1987). *Heat mining*. Cambridge: University Press.

Atrens, A.D., Gurgenci, H., & Rudolph, V. (2009). $CO_2$ thermosiphon for competitive geothermal power generation. *Energy & Fuels*, 23, 553-557.

Atrens, A.D., Gurgenci, H., & Rudolph, V. (2010). Electricity generation using a carbon-dioxide thermosiphon. *Geothermics*, 39, 161-169.

Atrens, A, Gurgenci, H, & Rudolph, V. (2011). Economic optimization of a $CO_2$-based EGS power plant. *Energy & Fuels*, 25, 3765-3775.

Azar, C., Lindgren, K., Larson, E., & Möllersten, K. (2006). Carbon capture and storage from fossil fuels and biomass–Costs and potential role in stabilizing the atmosphere. *Climatic Change*, 74, 47-79.

Baltimore AirCoil (BAC). (2013). Baltimore AirCoil's product selection software. Available at http://www.baltimoreaircoil.com/english/product-selection-software-public.

Beckers, K.F., Lukawski, M.Z., Anderson, B.J., Moore, M.C., & Tester, J.W. (2014). Levelized costs of electricity and direct-use heat from enhanced geothermal systems. *Journal of Renewable and Sustainable Energy*, 6. http://dx.doi.org/10.1063/1.4865575.

Blackwell D.D. & Richards, M. (2004). Geothermal map of North America. *American Assoc. Petroleum Geologist (AAPG)*. 1 sheet, scale 1:6,500,000.

Blackwell, D., Richards, M., Frone, Z., Batir, J., Ruzo, A., Dingwall, R., & Williams, M. (2011). Temperature-at-depth maps for the conterminous U.S. and geothermal resource estimates. *GRC Transactions*, 35, 1545-1550.

Borgia A., Pruess K., Kneafsey T. J., Oldenburg, C. M., and Pan, L. (2012). Numerical simulation of salt precipitation in the fractures of a $CO_2$-enchanced geothermal system. *Geothermics*, 44, 13-22. http://dx.doi.org/10.1016/j.geothermics.2012.06.002.

Brown, D. (2009). Hot dry rock geothermal energy: Important lessons from fenton hill. *Proceedings of the thirty-fourth workshop on geothermal reservoir engineering*, Stanford University, Stanford, California, February 9-11, 2009.

Buscheck, T.A., Bielicki, J.M., Randolph, J.B., Chen, M., Hao, Y., Edmunds, T.A., Adams, B., & Sun, Y. (2014). Multi-fluid geothermal energy systems in stratigraphic reservoirs: Using brine, $N_2$, and $CO_2$ for dispatchable renewable power generation and bulk energy storage (No. LLNL-CONF-650283). *Proceedings of the Thirty-Ninth Workshop on Geothermal Reservoir Engineering*, Stanford University, Stanford, California, February 24-26, 2014.

Buscheck, T.A., Sun, Y., Chen, M., Hao, Y., Wolery, T.J., Bourcier, W.L., Court, B., Celia, M.A., Friedmann, S.J., & Aines, R.D. (2012). Active $CO_2$ reservoir management for carbon storage: Analysis of operational strategies to relieve pressure buildup and improve injectivity. *International Journal of Greenhouse Gas Control*, 6, 230-245.

Buscheck, T.A., Elliot, T.R., Celia, M.A., Chen, M., Sun, Y., Hao, Y., Lu, C., Wolery, T.J., & Aines, R.D. (2013). Integrated geothermal-$CO_2$ reservoir systems: reducing carbon intensity through sustainable energy production and secure $CO_2$ storage. *Energy Procedia*, *37*, 6587-6594.

Carroll, S. & Stillman, G. (2014). Assessment of key physical and chemical research findings for the use of $CO_2$ as a heat exchanging fluid for geothermal energy production. *Proceedings of the Thirty-Ninth Workshop on Geothermal Reservoir Engineering*, Stanford University, Stanford, California, February 24-26, 2014.

Chen, H., Goswami, D.Y., Rahman, M.M., & Stefanakos, E.K. (2011). Energetic and exergetic analysis of $CO_2$-and R32-based transcritical Rankine cycles for low-grade heat conversion. *Applied Energy*, 88, 2802-2808.

Class, H., Ebigbo, A., Helmig, R., Dahle, H.K., Nordbotten, J.M., Celia, M.A., et al. (2009). A benchmark study on problems related to $CO_2$ storage in geologic formations: Summary and discussion of the results. *Computational Geosciences*, 13, 409-434.

Coleman, J.L. & Cahan, S.M. (2012). Preliminary catalog of the sedimentary basins of the United States: *U.S. Geological Survey Open-File Report 2012–1111*. Available at http://pubs.usgs.gov/of/2012/1111/.

Darcy, H. (1856) *Les fountaines publiques de la Ville de Dijon [The public fountains of the city of Dijon]*. Dalmont: Paris.

Database of State Incentives for Renewables and Efficiency (DSIRE). (2015). Minnesota renewable portfolio standard. Available at: http://www.dsireusa.org/incentives/incentive.cfm?Incentive_Code=MN14R.

Department of Energy (DOE). (2012). Guide to providing input to the model, August 2012. Available at: http://www1.eere.energy.gov/geothermal/getem_manuals.html.

Department of Energy Geothermal Technologies Office (DOE). (2015). What are low-temperature and coproduced resources? Available at http://energy.gov/eere/geothermal/low-temperature-and-coproduced.

DiPippo, R. (1985). A simplified method for estimating the silica scaling potential in geothermal power plants. *Geothermal Resource Council Bulletin*: May, 1-9.

DiPippo, R. (2012). *Geothermal power plants: Principles, applications, case studies, and environmental impact*. New York: Elsevier.

Doughty, C. & Pruess, K. (2004). Modeling supercritical carbon dioxide injection in heterogeneous porous media. *Vadose Zone Journal*, 3, 837-847.

Driesner, T. (2007). The system $H_20$-NaCl. Part II: Correlations for molar volume, enthalpy, and isobaric heat capacity from 0 to 1000 °C, 1 to 5000 bar, and 0 to 1 XNaCl. *Geochimica et Cosmochimica Acta*, 71, 4902-4919.

Duchane, D., & Brown, D. (2002). Hot dry rock (HDR) geothermal energy research and development at Fenton Hill, New Mexico. *Geo-Heat Center Bulletin*, 23, 13-19.

Eccles, J.K. & Pratson, L. (2014). A "carbonshed" assessment of small-vs. large-scale CCS deployment in the continental US. *Applied Energy*, 113, 352-361.

Elliot, T.R., Buscheck, T.A., & Celia, M. (2013). Active $CO_2$ reservoir management for sustainable geothermal energy extraction and reduced leakage. *Greenhouse Gases: Science and Technology*, *3*, 50-65.

Energy Information Administration (EIA). (2007). International energy statistics. Available at: http://www.eia.gov/cfapps/ipdbproject/IEDIndex3.cfm?tid=44&pid=44&aid=2.

Energy Information Agency (EIA). (2015a). Monthly energy review (MER). Available at: http://www.eia.gov/totalenergy/data/monthly/.

Energy Information Agency (EIA). (2015b). Electric power monthly. January, 2015. Available at: http://www.eia.gov/electricity/monthly/.

Environmental Protection Agency (EPA). (2014). Clean power plan proposed rule. http://www2.epa.gov/carbon-pollution-standards/regulatory-actions.

Farshad, F. & Rieke, H. (2006). Surface-roughness design values for modern pipes. *SPE Drilling & Completion*, 212-215.

Finley, R. (2005). An assessment of geologic carbon sequestration options in the Illinois Basin—Final report. Retrieved from http://www.sequestration.org/resources/reports.html.

Frailey, S., Damico, J., & Leetaru, H.. (2011). Reservoir characterization of the Mt. Simon sandstone, Illinois Basin, USA. *Energy Procedia*, 4, 5487–5494.

Freifeld, B., Zakim, S., Pan, L., Cutright, B., Sheu, M., Doughty, C., & Held, T. (2013). Geothermal energy production coupled with CCS: a field demonstration at the SECARB Cranfield Site, Cranfield, Mississippi, USA. *Energy Procedia*, 37, 6595-6603.

Ganjehsarabi, H., Gungor, A., & Dincer, I. (2012). Exergetic performance analysis of Dora II geothermal power plant in Turkey. *Energy*, 46, 101-108.

Garapati, N., Randolph, J.B., & Saar, M.O. (2014a). Total heat energy output from, thermal energy contributions to, and reservoir development of $CO_2$ plume geothermal (CPG) Systems. *PROCEEDINGS, Thirty-Ninth Workshop on Geothermal Reservoir Engineering* Stanford University, Stanford, California, February 24-26, 2014.

Garapati, N., Randolph, J.B., Valencia, J.L., & Saar, M.O. (2014b). $CO_2$ plume geothermal (CPG) heat extraction in multi-layered geologic reservoirs. *Energy Procedia*, 63, 7631-7643.

Garapati, N., Randolph, J.B., & Saar, M.O. (2015). Brine displacement by $CO_2$, energy extraction rates, and lifespan of a $CO_2$-limited $CO_2$-Plume Geothermal (CPG) system with a horizontal production well. *Geothermics*, 55, 182–194.

Geothermal Energy Association (GEA). (2013). 2013 geothermal power: International market overview. Available: http://geo-energy.org/events/2013%20International%20Report%20Final.pdf

Geothermal Technologies Office (GTA). (2015). Enhanced Geothermal Systems: How to extract more energy and power from geothermal resources. Available at: http://www1.eere.energy.gov/geothermal/pdfs/egs.pdf

Ghasemi, H., Sheu, E., Tizzanini, A., Paci, M., & Mitsos, A. (2014). Hybird solar-geothermal power generation: Optimal retrofitting. *Applied Energy*, 131, 158-170.

Global CCS Institute. (2012). The global status of CCS: 2012. Retrieved from http://www.globalccsinstitute.com/publications/global-status-ccs-2012.

Global CCS Institute. (2013). The global status of CCS: Summary report. Available online: http://www.globalccsinstitute.com/publications/global-status-ccs-2012-summary-report.

Global CCS Institute. (2014). The global status of CCS: 2014. Available at http://www.globalccsinstitute.com/publications/global-status-ccs-2014.

Goulds. (2013). Goulds VIT vertical industrial turbine pumps. Retrieved from http://www.gouldspumps.com/Products/VIT/.

Haar, L., Gallagher, J.S., & Kell, G.S. (1984). NBS-NRC steam tables: *Thermodynamic and transport properties and computer programs for vapor and liquid states of water in SI units*. Hemisphere.

Hitzman, M.W., Clarke, D.D., Detournay, E., Dieterich, J.H., Dillon, D.K., Green, S.J., et al. (2012). *Induced seismicity potential in energy technologies*. Washington, D.C.: The National Academics Press.

Intergovernmental Panel on Climate Change (IPCC). (2005). *IPCC special report on carbon dioxide capture and storage*. Prepared by working group III of the intergovernmental panel on climate change. (Metz, B, Davidson, O, de Coninck, HC, Loos, M, Meyer, LA., Eds.). Cambridge University Press: New York.

Intergovernmental Panel on Climate Change (IPCC). (2014). Climate Change 2014: Synthesis Report. Available at: http://www.ipcc.ch/report/ar5/syr/.

Janke, B. & Kuehn, T.H. (2011). Geothermal power cycle analysis for commercial applicability using sequestered supercritical $CO_2$ as a heat transfer or working fluid. *Proceedings of the ASME 2011 5th International Conference on Energy Sustainability*, Aug 7-10, 2011.

Kong, X.Z. & Saar, M.O. (2013). Numerical study of the effects of permeability heterogeneity on density- driven convective mixing during $CO_2$ dissolution storage. *International Journal of Greenhouse Gas Control*, 19, 160-173.

Luhmann, A.J., Kong, X.Z., Tutolo, B.M., Garapati, N., Bagley, B.C., Saar, M.O., & Seyfried Jr, W.E. (2014). Experimental dissolution of dolomite by $CO_2$-charged brine at 100ºC and 150 bar: Evolution of porosity, permeability, and reactive surface area. *Chemical Geology*, 380, 145–160.

Lund, J.W. & Bloomquist, R.G. (2012). Development of geothermal policy in the United States: What works and what doesn't work. *Proceedings of the 37th Workshop on Geothermal Reservoir Engineering*, Stanford University, Stanford, California, January 30 – February 1, 2012.

Luo, F., Xu, R.N., & Jiang, P.X. (2013). Numerical investigation of the influence of vertical permeability heterogeneity in stratified formation and of injection/production well perforation placement on $CO_2$ geological storage with enhanced CH4 recovery. *Applied Energy*, 102, 1314-1323.

Luo, F., Xu, R-N., & Jiang, PX. (2014) Numerical investigation of fluid flow and heat transfer in a doublet enhanced geothermal system with $CO_2$ as the working fluid. *Energy*, 64, 307-322.

Majer, E.L., Baria, R., Stark, M., Oates, S., Bommer, J., Smith, B., & Asanuma, H. (2007). Induced seismicity associated with enhanced geothermal systems. *Geothermics*, 36, 185-222.

Maraver, D., Royo, J., Lemort, V., & Quoilin, S. (2014). Systematic optimization of subcritical and transcritical organic rankine cycles (ORCs) constrained by technical parameters in multiple applications. *Applied Energy*, 117, 11-29.

Massachusetts Institute of Technology (MIT). (2006). The future of geothermal energy: Impact of enhanced geothermal systems (EGS) on the United States in the 21st century. Available at www.eere.energy.gov/geothermal/future_geothermal.html.

Mathias, S.A., Gluyas, J.G., Oldenburg, C.M., & Tsang, C. (2010). Analytical solution for Joule-Thomson cooling during $CO_2$ geo-sequestration in depleted oil and gas reservoirs. *International Journal of Greenhouse Gas Control*, 4, 806-810.

Meng, Q. & Jiang, X. (2014). Numerical analyses of the solubility trapping of $CO_2$ storage in geological formations. *Applied Energy*, 130, 581-591.

Metz, B., Davidson, O.R., Bosch, P.R., Dave, R., & Meyer, L.A., editors. (2007). Contribution of working group III to the fourth assessment report of the Intergovernmental Panel on Climate Change. Cambridge University Press: New York.

Midcontinent Independent System Operator (MISO). (2012a). Corporate fact sheet. Available at:

https://www.midwestiso.org/Library/Repository/Communication%20Material/Corporate/ Corporate%20Fact%20Sheet.pdf.

Midcontinent Independent System Operator (MISO). (2012b). Market reports – Archived market reports. Available at: https://www.midwestiso.org/Library/MarketReports/Pages/ArchivedMarketReports.aspx.

Moody, L.F. (1944). Friction factors for pipe flow. *Transactions of the ASME*, 671-684.

Myers, D., Wilcox, S., Marion, W., George, R., & Anderberg, M. (2005). Broadband model performance for an updated national solar radiation database in the United States of America. *Proc. Solar World Congress*, International Solar Energy Society.

Nathenson, M. & Guffanti, M. (1985). Geothermal gradients in the continuous United States. *Journal of Geophyiscal Research*, 93, 6437-6450.

National Climactic Data Center (NCDC). (2012). Hourly/subHourly climactic data. Available at: http://gis.ncdc.noaa.gov/map/cdo/?thm=themeHourly.

National Climactic Data Center (NCDC). (2013). The national climactic data center monthly normals. Retrieved from http://www.ncdc.noaa.gov/cdo-web/.

National Energy Technology Laboratory (NETL). (2010). Cost and performance baseline for fossil energy plants: Volume 1 Bituminous coal and natural gas to electricity. *Department of Energy publication DOE/2010/1397.*

National Renewable Energy Laboratory (NREL). (2006). Wind integration dataset-eastern wind dataset. Available at: http://www.nrel.gov/wind/integrationdatasets/eastern/ methodology.html.

National Renewable Energy Laboratory (NREL). (2007a). National solar radiation database-typical meteorological year v3. Available at http://rredc.nrel.gov/solar/old_data/ nsrdb/1991-2005/.

National Renewable Energy Laboratory (NREL). (2007b). National solar radiation database 1991-2005 update: User manual. Technical Report NREL/TP-581-41364.

National Renewable Energy Laboratory (NREL). (2009a). Development of eastern regional wind resource and wind plant output datasets. Subcontract Report NREL/SR-550-46764.

National Renewable Energy Laboratory (NREL). (2009b). U.S. 50m wind resource map. Available at: http://www.nrel.gov/gis/wind.html.

National Renewable Energy Laboratory (NREL). (2012). Photovoltaic solar resource of the United States. Available at: http://www.nrel.gov/gis/solar.html.

National Renewable Energy Laboratory (NREL). (2014). Geothermal power generation: Current and planned nameplate capacity (MW) by state. Retrieved from http://www.nrel.gov/gis/geothermal.html

Nordbotten, J.M., Celia, M.A., & Bachu, S. (2005). Injection and storage of $CO_2$ in deep saline aquifers: Analytical solution for $CO_2$ plume evolution during injection. *Transport in Porous media*, 58, 339-360.

Oldenburg, C.M. (2007). Joule-Thomson cooling due to $CO_2$ injection into natural gas reservoirs. *Energy Conversion and Management*, 48, 1808-1815.

Oldenburg, C.M., Stevens, S.H., & Benson, S.M. (2004). Economic feasibility of carbon sequestration with enhanced gas recovery (CSEGR). *Energy*, 29, 1413-1422.

Pan, L., & Oldenburg, C. M. (2014). T2Well—An integrated wellbore–reservoir simulator. *Computers & Geosciences*, *65*, 46-55.

Pan, L., Oldenburg, C.M., Wu, Y., & Pruess, K. (2010). T2Well/ECO2N version 1.0: Multiphase and non-isothermal model for coupled wellbore-reservoir flow of carbon dioxide and variable salinity water. *LBNL-4291E*.

Pan F., McPherson B., Lichtner P., Kaszuba J., Re, C.L., Karra, S., Lu, C., and Xu, T. (2013). Numerical evaluation of energy extraction, $CO_2$-rock interactions, and carbon sequestration in enhanced geothermal system (EGS) with supercritical $CO_2$ as a working fluid. *Proceedings 38th Workshop on Geothermal Reservoir Engineering*, Stanford University, Stanford, CA.

Pan, L., Freifeld, B., Doughty, C., Zakem, S., Sheu, M., Cutright, B., & Terrall, T. (2015). Fully coupled wellbore-reservoir modeling of geothermal heat extraction using $CO_2$ as the working fluid. *Geothermics*, 53, 100-113.

Pollack, H.N., Hurter, S.J., & Johnson, J.R. (1993). Heat flow from the earth's interior: Analysis of the global data set. *Reviews of Geophysics,* 31**,** 267-280.

Princiotta, F. (2014). Global climate change: The quantifiable sustainability challenge. Available at: http://www.swri.org/4org/d18/sCO$_2$/papers2014/climateChange-EPA.pdf

Princiotta, FT. & Loughlin, DH. (2014). Global climate change: The quantifiable sustainability challenge. *Journal of the Air & Waste Management Association*, 64, 979-994. http://dx.doi.org/10.1080/10962247.2014.923351

Procesi, M., Cantucci, B., Buttinelli, M., Armezzani, G., Quattrocchi, F., & Boschi, E. (2013). Strategic use of the underground in an energy mix plan: Synergies among $CO_2$, $CH_4$ geological storage and geothermal energy. Latium region case study (Central Italy). *Applied Energy*, 110, 104-131.

Pruess, K., Moridis, G., & Oldenburg, C. (1999). TOUGH2 user's guide, version 2.0. Report LBNL-43134, Lawrence Berkeley National Laboratory: Berkeley.

Pruess, K. (2004). The TOUGH codes — A family of simulation tools for multiphase flow and transport processes in permeable media. *Vadose Zone Journal*, 3, 738–746.

Pruess, K. (2005). ECO2N: A TOUGH2 fluid property module for mixtures of water, NaCl, and $CO_2$. Rep. LBNL-57952, Lawrence Berkeley National Laboratory: Berkeley.

Pruess, K. (2006). Enhanced geothermal systems (EGS) using $CO_2$ as working fluid—A novel approach for generating renewable energy with simultaneous sequestration of carbon. *Geothermics*, 35, 351-67.

Pruess, K. & Azaroual, M. (2006). On the feasibility of using supercritical $CO_2$ as heat transmission fluid in an engineered hot dry rock geothermal system. *Proceedings of the Thirty-First Workshop on Geothermal Reservoir Engineering*, Stanford University, Stanford, California, January 30-February 1, 2006.

Pruess, K. & Bodvarsson, G.S. (1984). Thermal effects of reinjection in geothermal reservoirs with major vertical fractures. *Journal of Petroleum Technology*, 16, 1567-78.

Quattrocchi, F., Boschi, E., Spena, A., Buttinelli, M., Cantucci, B., & Procesi, M. (2013). Synergic and conflicting issues in planning underground use to produce energy in

densely populated countries, as Italy: Geological storage of $CO_2$, natural gas, geothermics and nuclear waste disposal. *Applied Energy*, 101, 393-412.

Randolph, J.B. (2011). Coupling geothermal energy capture with carbon dioxide sequestration in naturally permeable, porous geologic formations -- a novel approach for expanding geothermal energy utilization. Retrieved from the University of Minnesota Digital Conservancy, http://purl.umn.edu/116297.

Randolph J.B., Adams B.M., Kuehn T.H., & Saar M.O. (2012). Wellbore heat transfer in $CO_2$-based geothermal systems. *Geothermal Resource Council Transactions,* 36, 549-554.

Randolph, J.B. & Saar, M.O. (2010). Coupling geothermal energy capture with carbon dioxide sequestration in naturally permeable, porous geologic formations: A comparison with enhanced geothermal systems. *Geothermal Research Council Transactions*, 34, 433-437.

Randolph, J.B. & Saar, M.O. (2011a). Coupling carbon dioxide sequestration with geothermal energy capture in naturally permeable, porous geologic formations: Implications for $CO_2$ sequestration. *Energy Procedia*, 4, 2206-2213.

Randolph, J.B. & Saar, M.O. (2011b). Combining geothermal energy capture with geologic carbon dioxide sequestration. *Geophysical Research Letters*, 38, L10401. http://dx.doi.org/10.1029/2011GL047265

Randolph, J.B. & Saar, M.O. (2011c). Impact of reservoir permeability on the choice of subsurface geothermal heat exchange fluid: $CO_2$ versus water and native brine. *Geothermal Resource Council Transactions*, 35, 521-526.

Randolph, J.B., Saar, M.O., & Bielicki, J.M. (2013). Geothermal energy production at geologic $CO_2$ sequestration sites: Impact of thermal drawdown on reservoir pressure. *Energy Procedia*, 37, 6625-6635.

Runkel, A.C., Miller, J.F., McKay, R.M., Palmer, A.R., & Taylor, J.F. (2007). High-resolution sequence stratiography of lower Paleozoic sheet sandstones in central North America: The role of special conditions of cratonic interiors in development of strata architecture. *Geological Society of America Bulletin*, 119, 860-881.

Saar, M.O. (2011). Review: Geothermal heat as a tracer of large-scale groundwater flow and as a means to determine permeability fields. *Hydrogeology Journal*, 19, 31-52.

Saar, M.O., Buscheck, T.A., Jenny, P., Garapati, N., Randolph, J.B., Karvounis, D.C., Chen, M., Sun, Y., & Bielicki, J.M. (2015). Numerical study of multi-fluid and multi-level geothermal system performance. *Proceedings of the World Geothermal Congress*, Melbourne, Australia, 19-25 April 2015.

Saar, M.O., Randolph, J. B., & Kuehn, T. H. (2012-2015). Carbon dioxide-based geothermal energy generation systems and methods related thereto. U.S. Patent No. 8,316,955 (issued 2012); Canada Patent No. 2.753.393 (issued 2013); Europe Patent No. 2406562 (issued 2014); Australia Patent No. 2010223059 (issued 2015).

Saar, M.O., Randolph, J.B., & Kuehn, T.H. (pending). Carbon dioxide-based geothermal energy generation systems and methods related thereto, U.S. patent application for CPG with enhanced oil recovery (EOR), i.e., CPG-EOR (continuation-in-part of CPG parent patent; patent application number: 13/554,868)

Sanyal, S. & Butler, S. (2005). An analysis of power generation prospects from enhanced geothermal systems. *Proceedings, World Geothermal Congress 2005*. Antalya, Turkey, 24-29 April 2005.

Sauret, E. & Gu, Y. (2014). Three-dimensional off-design numerical analysis of an organic rankine cycle radial-inflow turbine. *Applied Energy*, 135, 202-211.

Shengjun, Z., Huaixin, W., & Tao, G. (2011). Performance comparison and parametric optimization of subcritical organic rankine cycle (ORC) and transcritical power cycle system for low-temperature geothermal power generation. *Applied Energy*, 88, 2740-2754.

Singh, A.K., Goerke, U.J., & Kolditz, O. (2011). Numerical simulation of non-isothermal compositional gas flow: Application to carbon dioxide injection into gas reservoirs. *Energy*, 36, 3446-3458.

Smith, M.C., Aamodt, R.L., Potter, R.M., & Brown, D.W. (1975). Man-made geothermal reservoirs. Los Alamos Scientific Laboratory. Technical Report. OSTI: 5132450, LA-UR-75-953; CONF-750525-6.

Southern Methodist University Geothermal Lab (SMU). (2012a). Heat flow maps. Available: http://smu.edu/geothermal/GeothermalMap/geothermalmap.html.

Southern Methodist University Geothermal Lab (SMU). (2012b). Thermal gradient map. Available at: http://smu.edu/geothermal/heatflow/heatflow.htm.

Span, R. & Wagner, W. (1996). A new equation of state for carbon dioxide covering the fluid region from the triple-point temperature to 1100 K at pressures up to 800 MPa. *Journal of Physical Chemical Reference Data*, 25, 1509-1596.

Spycher, N. & Pruess, K. (2011). A model for thermophysical properties of $CO_2$-brine mixtures at elevated temperatures and pressures. *Proceedings Thirty-Sixth Workshop on Geothermal Reservoir Engineering*, Stanford University, Stanford, CA, January 31 – February 2, SGP-TR-191.

Tester, J.W., Brown, D.W., & Potter, R.M. (1989). Hot dry rock geothermal energy—A new energy agenda for the 21st Century. LA-11514-MS, Los Alamos National Laboratory, Los Alamos, NM.

Toffolo, A., Lazzaretto, A., Manente, G., & Paci, M. (2014). A multi-criteria approach for the optimal selection of working fluid and design parameters in organic rankine cycle systems. *Applied Energy*, 121, 219-232.

Tutolo, B.M., Luhmann, A.J., Kong, X.Z., Saar, M.O., & Seyfried Jr, W.E. (2014). Experimental observation of permeability changes in dolomite at $CO_2$ sequestration conditions. *Environmental Science and Technology*, 48, 2445-2452.

Tutolo, B.M., Schaen, A.T., Saar, M.O., & Seyfried Jr, W.E. (in press). Implications of the redissociation phenomenon for mineral-buffered fluids and aqueous species transport at elevated temperatures and pressures. *Special Issue in Applied Geochemistry*.

United States Department of Energy (DOE). (2012). Geothermal electricity technology evaluation model (GETEM). Retrieved from http://energy.gov/eere/geothermal/geothermal-electricity-technology-evaluation-model.

U.S. President. (2013). The president's climate action plan. Available at: http://www.whitehouse.gov/sites/default/files/image/president27sclimateactionplan.pdf

Wang, J.L., Zhao, L., & Wang, X.D. (2012). An experimental study on the recuperative low temperature solar Rankine cycle using R245fa. *Applied Energy*, 94, 34-40.

Yin, H., Sabau, A.S., Conklin, J.C., McFarlane, J., & Qualls, A.L. (2013). Mixtures of $SF_6$–$CO_2$ as working fluids for geothermal power plants. *Applied Energy*, 106, 243-253.

Zhang, L., Ezekiel, J., Li, D., Pei, J., & Ren, S. (2014). Potential assessment of $CO_2$ injection for heat mining and geological storage in geothermal reservoirs of China. *Applied Energy*, 122, 237-246.

Ziagos, J., Phillips, B.R., Boyd, L., Jelacic, A., Stillman, G., and Hass, E. (2013). A technology roadmap for strategic development of enhanced geothermal systems. *Proceedings of the Thirty-eighth workshop on geothermal reservoir engineering, Stanford University, Stanford, California, February 11-13, 2013.*

# Appendix: Copyright Reprint Licenses

This appendix contains copyright reprint licenses for the three published papers in this dissertation: [Chapter 2] Adams et al. (2014), [Chapter 3] Adams et al. (2015), and [Chapter 5] Adams and Kuehn (2012).

# Reprint License for Adams et al. (2014)





**Title:** On the importance of the thermosiphon effect in CPG (CO2 plume geothermal) power systems

**Publication:** Energy

**Publisher:** Elsevier

**Date:** 1 May 2014



## Order Completed

Thank you very much for your order.

This is a License Agreement between Benjamin M Adams ("You") and Elsevier ("Elsevier"). The license consists of your order details, the terms and conditions provided by Elsevier, and the payment terms and conditions.

Get the printable license.

| | |
|---|---|
| License Number | 3596220168433 |
| License date | Mar 25, 2015 |
| Licensed content publisher | Elsevier |
| Licensed content publication | Energy |
| Licensed content title | On the importance of the thermosiphon effect in CPG (CO2 plume geothermal) power systems |
| Licensed content author | None |
| Licensed content date | 1 May 2014 |
| Licensed content volume number | 69 |
| Licensed content issue number | n/a |
| Number of pages | 10 |
| Type of Use | reuse in a thesis/dissertation |
| Portion | full article |
| Format | both print and electronic |
| Are you the author of this Elsevier article? | Yes |
| Will you be translating? | No |
| Title of your thesis/dissertation | On the Power Performance and Integration of Carbon-dioxide Plume Geothermal (CPG) Electrical Energy Production |
| Expected completion date | Mar 2015 |
| Estimated size (number of pages) | 120 |
| Elsevier VAT number | GB 494 6272 12 |
| Permissions price | 0.00 USD |
| VAT/Local Sales Tax | 0.00 USD / 0.00 GBP |
| Total | 0.00 USD |

ORDER MORE... CLOSE WINDOW

# Reprint License for Adams et al. (2015)





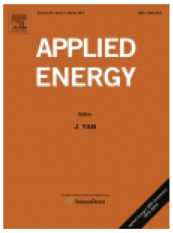


**Title:** A comparison of electric power output of CO2 Plume Geothermal (CPG) and brine geothermal systems for varying reservoir conditions

**Publication:** Applied Energy

**Publisher:** Elsevier

**Date:** 15 February 2015





## Order Completed

Thank you very much for your order.

This is a License Agreement between Benjamin M Adams ("You") and Elsevier ("Elsevier"). The license consists of your order details, the terms and conditions provided by Elsevier, and the payment terms and conditions.

Get the printable license.

| | |
|---|---|
| License Number | 3596220450747 |
| License date | Mar 25, 2015 |
| Licensed content publisher | Elsevier |
| Licensed content publication | Applied Energy |
| Licensed content title | A comparison of electric power output of CO2 Plume Geothermal (CPG) and brine geothermal systems for varying reservoir conditions |
| Licensed content author | None |
| Licensed content date | 15 February 2015 |
| Licensed content volume number | 140 |
| Licensed content issue number | n/a |
| Number of pages | 13 |
| Type of Use | reuse in a thesis/dissertation |
| Portion | full article |
| Format | both print and electronic |
| Are you the author of this Elsevier article? | Yes |
| Will you be translating? | No |
| Title of your thesis/dissertation | On the Power Performance and Integration of Carbon-dioxide Plume Geothermal (CPG) Electrical Energy Production |
| Expected completion date | Mar 2015 |
| Estimated size (number of pages) | 120 |
| Elsevier VAT number | GB 494 6272 12 |
| Permissions price | 0.00 USD |
| VAT/Local Sales Tax | 0.00 USD / 0.00 GBP |
| Total | 0.00 USD |

# Reprint License for Adams and Kuehn (2012)

Ben Adams <adam0068@umn.edu>

## Permission to reprint

**Beth Darchi** <DarchiB@asme.org> Thu, Mar 26, 2015 at 12:30 PM
To: Ben Adams <adam0068@umn.edu>

Dear Prof. Adams,

It is our pleasure to grant you permission to publish **any part or all of** the ASME paper "The Complementary Nature of CO2-Plume Geothermal (CPG) Energy Production and Electrical Power Demand," by Benjamin M. Adams and Thomas H. Kuehn, Paper No. IMECE2012-88704, as cited in your letter in the dissertation entitled On the power performance and integration of carbon-dioxide plume geothermal (CPG) electrical energy production to be published by University of Minnesota.

Permission is granted for the specific use as stated herein and does not permit further use of the materials without proper authorization. Proper attribution must be made to the author(s) of the materials. **Please note**: if any or all of the figures and/or Tables are of another source, permission should be granted from that outside source or include the reference of the original source. ASME does not grant permission for outside source material that may be referenced in the ASME works.

As is customary, we request that you ensure proper acknowledgment of the exact sources of this material, the authors, and ASME as original publisher. Acknowledgment must be retained on all pages printed and distributed.

Many thanks for your interest in ASME publications.

Sincerely


**Beth Darchi**
Publishing Administrator
ASME
2 Park Avenue, 6th Floor
New York, NY 10016-5990
Tel 1.212.591.7700
darchib@asme.org